Integration of PV systems in urban environments

A location-dependent performance study

Andres Calcabrini

Technische Universiteit Delft

TUDelft

Integration of PV systems in urban environments

A location-dependent performance study

by

Andres Calcabrini

to obtain the degree of Master of Science in Sustainable Energy Technology
at the Delft University of Technology,
to be defended publicly on Tuesday October 19, 2017 at 10:00 AM.

Student number:	4509161	
Project duration:	October 30, 2016 – October 19, 2017	
Thesis committee:	Prof. Dr. M. Zeman,	TU Delft
	Dr. O. Isabella,	TU Delft
	Dr. M. Ghaffarian Niasar,	TU Delft
	Ir. N. Kooke,	Kameleon Solar

TU Delft

Abstract

The present thesis project approaches the integration of small-scale PV systems in urban environments and the prediction of the energy yield. It aims to find a simple method energy yield prediction model that accounts for the effects of the surroundings on the generated power.

The most accurate existing frameworks that are used to calculate the energy yield of a PV system rely on the integration of the solar power received by the solar modules. These methods although being precise, become computationally demanding when the performance of a solar panel has to be studied for a large number of locations.

As part of the present study a new version of the Infotainment Spot has been designed and fabricated for bus stops in the Netherlands. Applying the existing frameworks, the performance is simulated for a large number of urban scenarios. Based on the results, a novel approach is proposed by correlating the yield of the Infotainment Spot with the characteristics of the skyline profiles.

The model proposed in this study is applicable in most urban scenarios and valid in an extensive geographic area. Furthermore, it was determined that the annual energy yield prediction model can estimate the performance of a PV system with 10% accuracy in average.

Acknowledgements

During the last year, many people have helped me, and I am truly thankful to all those that selflessly supported me and contributed to this project.

Among the people that directly contributed to this work, I am specially grateful for the invaluable help of to Dr. Olindo Isabella, my daily supervisor. He opened me the door of his office uncountable number of times, and did not only guide me and gave me excellent pieces of advice, but he also encouraged me to go a little bit deeper into every aspect of this work.

I would also like to express my gratitude to Prof. Miro Zeman, chairman of the PVMD group at TU Delft, who made this work possible by initiating the relations with Kameleon Solar.

On the side of Kameleon Solar, the company that together with the PVMD group has financed this project, I am thankful to Guust Verpaalen, Nico Kooke, Kevin Verpaalen and Peter van Geloven who have been very helpful and facilitated the design process of the Infotainment Spot.

My special gratitude also goes to:

- Dr. Rudi Santbergen, for the time he dedicated to hearing about my project and the recommendations he gave me.
- Eternal Sun, who kindly allowed me to conduct tests in their facilities, and Elias Garcia Goma who spent his free time helping me there.
- Vimal Adithyan Muthukumar, who was always predisposed and has taught how to apply his work to my project.
- Stefaan Heirman, who helped me in assembling the Infotainment Spot prototype.

Last but not least, I want to highlight the role of my family and especially my parents, who through their tireless effort have given me this opportunity, and have supported me every minute since the moment I decided to study abroad.

Andres Calcabrini
Delft, October 2017

Contents

List of symbols

AOI	Angle Of Incidence	$[deg]$
A_a	Active area of the PV module	$[m^2]$
a_M	Module elevation	$[deg]$
A_M	Module orientation	$[deg]$
a_S	Sun elevation	$[deg]$
A_S	Sun azimuth	$[deg]$
C_{bat}	Battery nominal capacity	$[Wh]$
D_h	PV module hydraulic diameter	$[m]$
DHI	Diffuse Horizontal Irradiance	$[\frac{W}{m^2}]$
DNI	Direct Normal Irradiance	$[\frac{W}{m^2}]$
E_a	Extraterrestrial radiation	$[\frac{W}{m^2}]$
E_{bat}	Energy stored in battery	$[Wh]$
E_d	Battery energy density	$[\frac{Wh}{kg}]$
E_{dump}	Energy dump in off-grid PV system	$[Wh]$
E_g	Bandgap energy	$[eV]$
E_y	Annual Energy Yield	$[\frac{kWh}{yr}]$
g	Gravitational acceleration	$[\frac{m}{s^2}]$
GHI	Global Horizontal Irradiance	$[\frac{W}{m^2}]$
G_M^{diff}	Diffuse irradiance	$[\frac{W}{m^2}]$
G_M^{dir}	Direct beam irradiance	$[\frac{W}{m^2}]$
G_M^{gnd}	Ground reflected irradiance	$[\frac{W}{m^2}]$
G_M^{tot}	Total irradiance on PV module	$[\frac{W}{m^2}]$
Gr	Grashof Number	$[-]$
I_{mpp}	Maximum power point current	$[I]$
I_{ph}	Photogenerated current	$[A]$
I_{SC}	Short-circuit current	$[A]$
L	PV module length	$[m]$
Nu	Nusselt Number	$[-]$
Pr	Prandlt Number	$[-]$
r_D	Isotropic Sky View Factor	$[-]$
Re	Reynolds Number	$[-]$
R_{int}	Battery internal resistance	$[m\Omega]$
R_s	P cell series resistance	$[\Omega]$
R_{sh}	PV cell shunt resistance	$[\Omega]$
SCF	Sun Coverage Factor	$[-]$
SoC	Battery State of Charge	$[Wh]$
SVF	Sky View Factor	$[-]$
T_M	PV Module temperature	$[^\circ C]$
V_{mpp}	Maximum power point voltage	$[V]$
V_{OC}	Open-circuit voltage	$[V]$
w	Wind speed	$[\frac{m}{s}]$
W	PV module width	$[m]$
α_{gnd}	Albedo cofficient	$[-]$
Δ	Sky brightness	$[-]$
θ_M	Module tilt	$[deg]$
$\kappa_{I_{SC}}$	Short circuit current temperature coefficient	$[\frac{mA}{^\circ C}]$
$\kappa_{V_{OC}}$	Open circuit voltage temperature coefficient	$[\frac{mV}{^\circ C}]$
$\kappa_{P_{mpp}}$	Maximum power temperature coefficient	$[\frac{mW}{^\circ C}]$
κ_η	Module efficiency temperature coefficient	$[\frac{\%}{^\circ C}]$
τ	Transmittance	$[-]$

1 Introduction

1.1. Overview of the solar energy industry

The expected worldwide energy demand in 2017 is 590 quadrillion Btu. In terms of average power, this amount is equivalent to 19.7 TW, or approximately 2.6 kW per human being on the planet. With China, Japan and Germany on the lead, the energy demand is expected to increase by 30% by 2040 [1]. This projection represents a challenge from two points of view: on one hand energy production must be increased at an unprecedentedly high rate; on the other hand, the share of low-carbon energy sources has to be drastically increased in order to meet the goals set by the Paris Agreement on climate change which entered into force on November 2016.

Nowadays, around 80% of the energy consumed is obtained from fossil fuels, and electricity represents only one-fourth of the total energy consumed. The share of electricity in the total energy generation is expected to increase in 69% by 2040, from 21.6 PWh in 2012 to 25.8 PWh in 2020 and 36.5 PWh in 2040 (IEA 2016). The fact that only 23.5% of the generated electricity in 2016 comes from renewable sources reflects the dimensions of the Energy Transition challenge [2].

Among the renewable energy sources hydro-power plants play a predominant role (17% share in total electricity generation), however, the installed capacity can only be duplicated with the available resources on Earth. Solar energy, on the other hand, has the potential of providing more than 1000 times the power demanded by the world, but at the moment it only contributes in 1% to the net electricity generation (refer to Figure 1.1). .

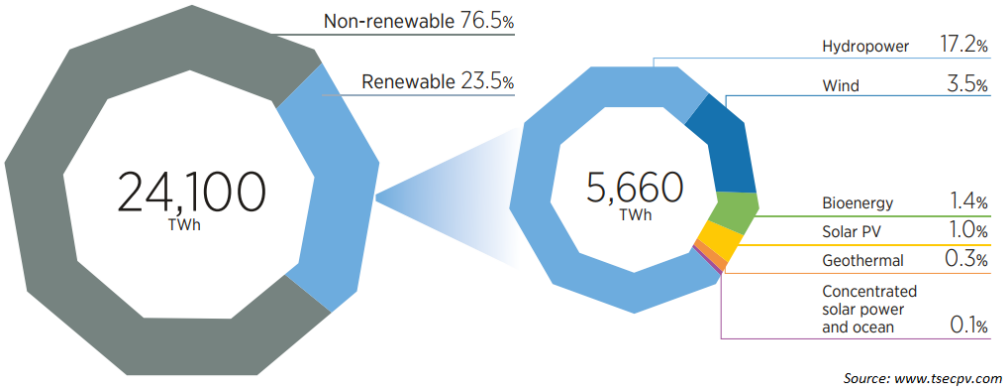

Figure 1.1: Global electricity generation by source in 2015 (Retrieved from [2])

The sun is without any doubt the energy source that offers the highest potential to face the energy transition process. Photovoltaic technology has made significant progress in the last 20 years. Pushed by the increase in efficiency and the cost reduction, the industry sector has experienced an impressing boost during the last decade. In 2017, solar panels with a life expectancy longer than 25 years and a conversion efficiency higher than 20% are readily available on the retail market for less than $1.5/W_p$ (and less than $1/W_p$ in the

wholesale market). All these are clear indicators that Solar is ready to become the leader renewable energy industry.

There are several PV technologies available in the market, but mainly three dominate at the moment: thin-film, multi-crystalline silicon (mc-Si) and mono-crystalline silicon (mono-Si). Figure 1.2 shows how the market share of each of these technologies has evolved since 1980. Thin-film technology has been relegated by crystalline silicon due to multiple reasons: the natural abundance of materials (compared to CdTe), the lower manufacturing costs (compared to CI(G)S), and the higher conversion efficiency (compared to amorphous silicon).

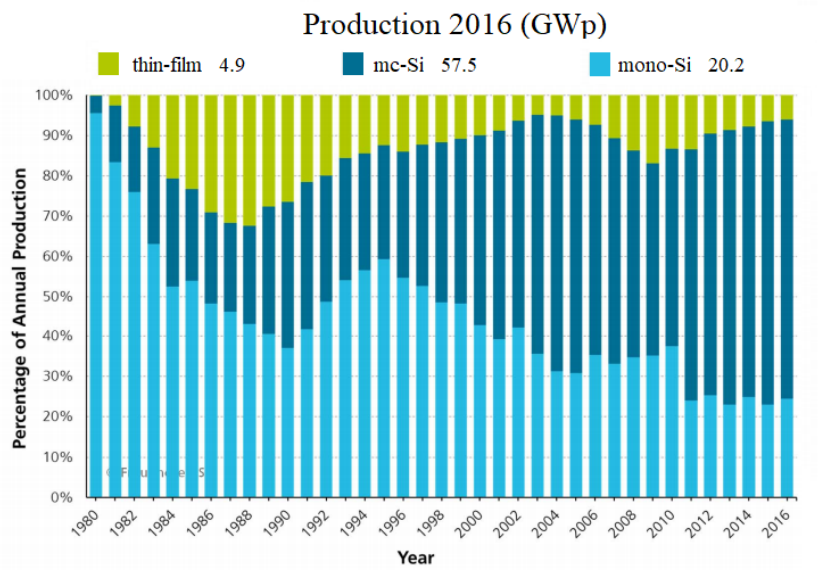

Figure 1.2: Market share of different PV technologies[21]

Among crystalline silicon technology, p-type wafer solar cells dominate the market. Nonetheless, the market share of n-type wafer solar cells has started to grow and is expected to become dominant in the future, as it allows to achieve higher conversion efficiencies (see Figure 1.3).

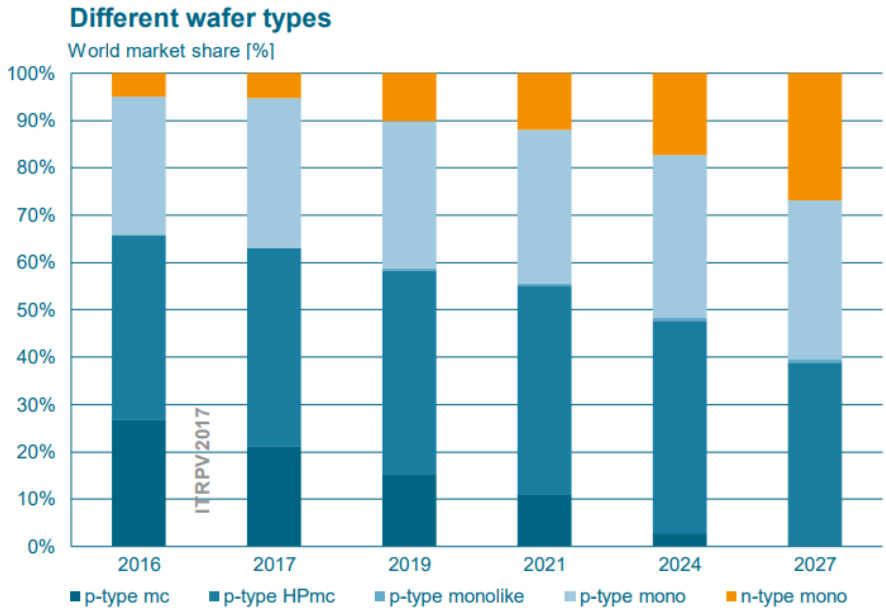

Figure 1.3: Market share of different wafer types for crystalline Si solar cells[29]

Historically p-type wafers have dominated for multiple reasons: higher tolerance to radiation damage in space applications; lower temperature requirements for phosphorous diffusion compared to boron; a more uniform resistivity of p-type ingots compared to n-type ingots[13]. However, n-type wafer solar cells offer higher efficiencies due to two main reasons. First, the absence of boron-oxygen related defects, which results in a higher minority carrier lifetime even though the mobility of holes is around three times smaller than that of electrons in c-Si. Second, the higher tolerance for metallic impurities, since the capture cross-section of transition metal impurities for holes is much less than the capture cross-section for electrons[6].

The reasons why the p-type solar cells remain dominant are related to the production scale, which makes the price of p-type ingots slightly lower, and also to the fact that the fabrication of n-type solar cells requires some additional steps.

1.2. PERC technology

The Passivated Emitter Rear Cell concept was proposed for the first time in 1984 in the University of New South Wales[3]. The first high-efficiency PERC solar cells (based on a p-type wafer) were fabricated in 1988 and achieved a conversion efficiency of 21.8% (20.9% to present standards), which represented a 2.7% increment on the highest confirmed efficiency of a Si solar cell at that time[5]. PERC will probably become the dominant cell technology by 2020 since it will enable greater efficiencies by introducing relatively small changes in current cell production lines. Researchers expect PERC technology to reach 24.4% conversion efficiency for 6 inches commercial solar cells in the close future[16].

The PERC acronym is also used to describe a family of different solar cells, including PERT (Passivated Emitter, Rear Totally-diffused), PERL (Passivated Emitter, Rear Locally-diffused) cells. However, the PERC architecture has proven to be the most viable option for the industry[5]. The structure of a conventional Si and a PERC solar cell are compared in Figure 1.4.

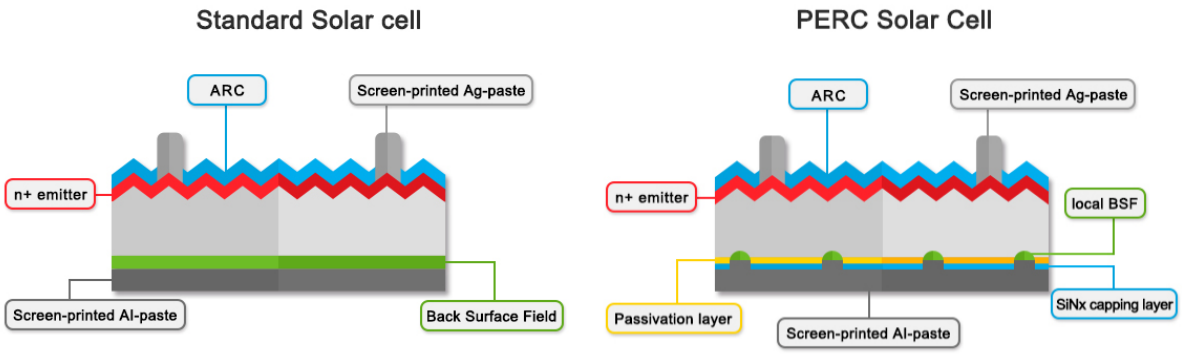

Figure 1.4: Comparison between a conventional and a PERC mono-Si solar cell

The increment in conversion efficiency of PERC solar cells in 1984 was attributed to two main facts: the use of chlorine-based processing and the contacting at the rear part of the cell[3]. PERC solar cells are fabricated by applying a dielectric passivation film on the back of the cell and subsequently creating small pockets on the film to allow the contact between the Si and the conducting layer.

The passivation layer in p-type wafers is commonly made of a thin PECVD silicon or aluminum oxide[1]. The passivation layer reduces the recombination induced by the dangling bonds at the surface of the Si. Additionally, the lower refractive index of the dielectric layer (compared to Si) significantly enhances the reflection at the back surface. The higher back reflection increases the chances of light absorption in the Si, and also improves the thermal performance of the cell by reducing the absorption of photons with energy lower than the band gap in the back Al contact.

Photons with energies close to that of the bandgap are absorbed deeper in the base of the solar cell. The characteristics mentioned above allow the charge carriers generated by these photons to be collected more efficiently. Since there is a higher proportion of infrared light during mornings and evenings, manufacturers claim that PERC cells perform better under weak light conditions.

[1] Plasma-Enhanced Chemical Vapor Deposition (PECVD) can be used for depositing both SiO_x and Al_2O_3, but the aluminum oxide can also be deposited using Atomic Layer Deposition (ALD)[9].

1.3. Motivation

This thesis project was developed with the support of Kameleon Solar. Kameleon Solar is a Dutch company dedicated to the design and manufacture of customized solar modules for a broad range of applications. This study originated from the mutual interest of the PVMD group and Kameleon Solar in developing a PV-powered solution together. In particular, Kameleon Solar expressed interest in developing a solar-powered kiosk for public places. In the end, it was decided to work on solutions for public transport networks.

As part of the design process of PV powered solutions, it is necessary to estimate how the PV system will perform in different locations. The design requirements are directly linked to the locations where a system is to be installed. Consequently, the most common design approach is to (first) choose a set of locations, and then use the irradiation characteristics of those sites to define the requirements of the system. However, in many cases there is another approach that can be more convenient. This approach consists in starting from a more general design (or an already existing one), and then finding all those locations where the solution could be applied. In this method, the second step can be used to retrofit the original design and broaden the applicability of the system.

In this second design approach, it is implicit the capacity to easily estimate the performance of a PV system in a large number of locations. As the number of location increases, the application of conventional methods for determining performance of a PV system becomes highly demanding and complicated. Therefore, in cases like these, it would be much more convenient to have a model that would allow to quickly predict the performance of a PV system at expense of some accuracy in the results. The development of such a model is the ultimate goal of this project.

1.3.1. Brief description of the Dutch public transport network

Mobility is a key aspect of modern societies. According to the World Economic Forum, The Netherlands has one of the most developed transport infrastructures in the world. Every day in The Netherlands more than 4.5 million trips are made by tram, bus, and metro[17].

The number of stops and the frequency of public transport are two important factors that influence the mean of transport that people choose to move in urban environments. In Holland, the time between consecutive trams oscillates between 8 and 15 minutes while the bus frequency is generally between 2 and 4 buses per hour[2].

The availability of precise public transport schedules and mobile applications contribute to reduce the time people spend on a stop. Additionally, many stops have electronic displays which indicate the arrival time of the next bus. Some of these displays are powered by small multi-crystalline solar panels like the one shown in Figure 1.5.

Figure 1.5: Solar-powered LCD for indicating the time to the next bus or tram

The original motivation of this project was to develop a solar-powered kiosk for public transport networks to demonstrate what can be achieved with flexible solar modules and the high conversion efficiency that

[2]These figures have been obtained from an analysis of bus and tram schedules in year 2016.

PERC solar cells offer. Based on this first idea, the research questions that constitute the core of this study were formulated.

1.4. Research Questions

The present study aims to answer three main research questions, which have been broken down to simplify and guide the answers. The research questions are presented below:

1. What is the result of implementing a tracking system on the Infotainment Spot?
   (a) How can the design of the tracking system be optimized?
   (b) What is the gain in the harvested energy by using a tracking system when compared to a fixed tilt system?
2. Can the characteristics of a skyline profile be quantified to create a simplified model for estimating the energy yield of a PV system?
   (a) What are the relevant parameters?
   (b) What is the accuracy of such estimation?
   (c) What are the limitations of the approach?
3. What are the limitations of an off-grid Infotainment Spot?
   (a) What is the best battery technology for this application?
   (b) What is the effect of winter on the required storage capacity?
   (c) Are there restrictions on the skyline profiles characteristics for the acceptable locations?

This thesis project concluded with the construction of a fully functional prototype of the designed infotainment spot.

1.5. Thesis Outline

The thesis report is organized in six chapters. The overview of each of the chapters is presented below.

Chapter 1 - Introduction In the first chapter, a brief review of the current state of the solar energy industry and the public transport networks in The Netherlands is given to motivate this study. The introductory chapter concludes with the statement of the main research questions of this project.

Chapter 2 - Design concepts In this chapter, previous related projects are recapitulated. Consecutively the central design concepts and their characteristics are discussed.

Chapter 3 - Physical models This chapter describes the optical, thermal and electrical models used to calculate the yield of a PV system.

Chapter 4 - PV designs and simulations This is the core chapter of this study. The results of the PV yield simulations are presented and discussed in this part.

Chapter 5 - Balance of System The fifth chapter is dedicated to the design of the BoS applying the results from Chapter 4. In particular, the description of the load profile and the design of the energy storage system are discussed. Finally, the prototype of the Infotainment Spot is presented.

Chapter 6 - Conclusions and outlook The last chapter summarizes the answers to the research questions and gives an outlook on this work.

2

The design concepts

This thesis project focuses on the design of two primary PV systems for bus and tram stops. Both systems are based on the Infotainment Spot concept. The first one is a fixed-tilt system, while the second one integrates a solar tracking unit.

Additionally to the design of the off-grid PV system, and in order to expand the applicability of the models introduced, the performance of a grid-tied PV bus shelter has been assessed.

2.1. Infotainment spot

The first Infotainment Spot, shown in Figure 2.1, was developed in 2014 at TU Delft. It is powered by a 90 W_p flexible thin-film PV module with 36 CIGS solar cells. The back of the structure is a concave surface on top of which the PV module is fixed. The most salient aspect of the solar panel is that it includes a bypass diode per cell, which allows different groups of cells to be more productive during different times of the day and the year [31].

The first version was meant to be placed in the vicinity of the EEMCS faculty and is equipped with a 12 V VRLA battery of 120 Ah. The modules and the battery power a tablet which allows the user to access the Internet and different applications. The kiosk is also a mobile charging station and it provides a 5 V USB charger.

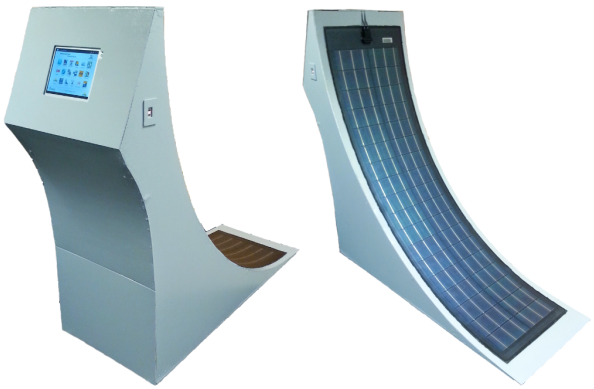

Figure 2.1: First version of the Infotainment Spot

A more recent version of the Infotainment Spot that was developed in 2017 is shown in Figure 2.2. This model was designed for Japan and is powered by two series-connected solar modules made of silicon hetero-junction solar cells which together can deliver 100 W_p[22]. In this second design, the cells were cut in half to duplicate the voltage of the module, and there is only one bypass diode per module. The storage system consists of one 12 V $LiFePO_4$ battery of 150 Ah. The kiosk is equipped with a Raspberry Pi 3, an LCD touch-screen, a USB and a wireless phone charger.

The features of both designs have been taken into account for the design of a third version of the Infotainment Spot. The goal of this project is to reduce the footprint of the structure to place in a typical bus stop,

Figure 2.2: Second version of the Infotainment Spot

and also to study the viability of an Infotainment Spot with a solar tracking system. Moreover, while the two previous kiosks have been designed for specific places, in this project the geographic location of the structure is considered as a variable and is not restricted.

2.2. PV Bus shelter

The concept of a PV bus shelter has been studied by multiple universities and companies. Generally, companies show more interest in this type of systems for two reasons: flat panels offer higher yields than curved modules, and also the available surface area on bus stop sheds is larger than on a kiosk. Some typical design concepts are shown in Figure 2.3.

The first bus shelters were built with commercial opaque modules. However, more recently, glass to glass modules have been introduced. The latter option is not only more elegant but also the separation between cells can be chosen so that some light can go through the panel.

Figure 2.3: PV bus shelter design concepts

The electrical energy generated by these designs is usually injected into the grid. The inverter is either embedded in the same bus shelter structure or located in a connection box underground or next to the bus stop.

2.3. Dutch bus shelter design

In The Netherlands different types of bus shelters can be found. This study is centered on the most common bus shelters in North and South Holland like the one shown in Figure 2.4.

The pavement width is generally at least 1.5 m wide, and the bus shelter consists of a metallic structure

with glass panes on the roof and walls. The glass panes on the roof are at least 1.4 $mx1.6$ m large, and they are tilted 5°. This angle allows the rainwater to remove the dust that is deposited on the rooftop.

Figure 2.4: Most common bus shelter design in Holland

Bus shelters are grid connected and use the grid to power LED lamps for illumination, and also electronic signs for advertising.

2.4. Design considerations

The design goals of the off-grid kiosk have been decided together with Kameleon Solar. The most relevant requirements of the new Infotainment spot are listed below:

- Off-grid: The company was interested in designing a solution that could also be applicable in countries where the electrical network is not as reliable as in The Netherlands.
- Reduced footprint: The footprint of the kiosk must be reduced to fit in the width of a typical bus stop sidewalk.
- Robust design: The kiosk must be safe and robust to resist acts of vandalism.
- Visually appealing: In order to improve the aesthetics of the design, curved panels must be used.
- Tracking system: The design of the kiosk must contemplate the implementation of a solar tracking system on the same base structure.

The study of PV bus shelters was carried out applying the same framework and models as for the Infotainment Spot. The design considerations for this system are the following:

- Grid-tied: The PV bus shelter must be grid-tied in order to maximize the utilization of the generated PV power.
- Glass-glass PV modules: The existent glass panes are to be replaced by KS Glass PV Modules.
- Based on the existent shelter structure: The metallic structure is not to be modified, which implies that the tilt angle of the PV module is fixed at 5°.

3

Physical models

The irradiance on the surface of a photovoltaic panel must be determined to estimate the produced electric power. There are several meteorological stations around the world that can provide radiation data, which can be used to build an irradiance framework to accurately predict the energy yield of a solar module. In this work two irradiance frameworks are presented.

Once the irradiance on the surface of a PV cell is known, a thermal model is needed to estimate the cell temperature. The temperature can be in turn used to calculate the conversion efficiency.

Finally, an electrical model is used to determine how many (the current) and how energetic (the voltage) are the charge carriers generated by the incident photons at the given temperature.

This chapter deals with all the models used for calculating the energy yield of the PV modules.

3.1. Irradiance framework A

The radiation incident on a tilted plane can be decomposed in three main components (refer to Figure 3.1):

1. The direct beam component (G_M^{dir}): It is the fraction of the Sun radiation that travels in a straight line from the sun to the module's surface. When the sun is blocked by buildings o cover by clouds, this component is null.

2. The diffuse light component (G_M^{diff}): It is the fraction of the radiation emitted by the Sun that is scattered by the molecules that compose the Earth's atmosphere. Diffuse radiation arriving at the surface of the module has no particular direction, and it is maximized when the module is placed horizontally.

3. The ground-reflected radiation (G_M^{gnd}): It represents the radiation that reaches the module after being reflected on the floor. Its value is related to the reflectivity (albedo) of the ground surface. This component is especially important for modules with a large tilt and also for bifacial solar panels.

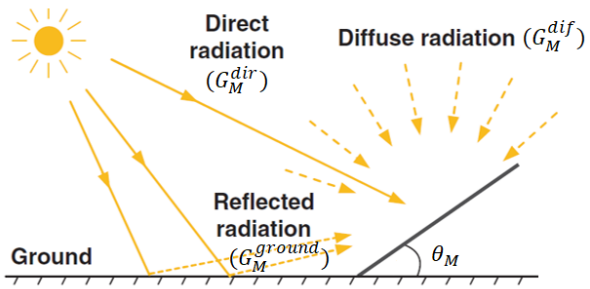

Figure 3.1: Solar radiation components (retrieved from [15])

The addition of these three components results in the total incident irradiance on a flat surface:

$$G_M^{tot} = G_M^{dir} + G_M^{diff} + G_M^{gnd} \tag{3.1}$$

The models used in this work to calculate each of these components from measured data are described in detail below.

3.1.1. Sun position and module orientation

Prior to presenting the models used to calculate the radiation components, a convention must be adopted to describe the Sun position and the panel orientation. In this study, the same convention as in [27] was used.

In Figure 3.2 the position of an object (in this case the Sun) is described with coordinates in the reference frame of an observer (in this case the PV module) located on the Earth's surface.

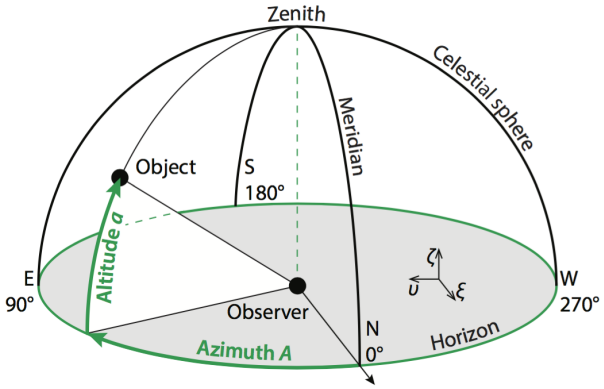

Figure 3.2: Illustration of the angles that describe the position of the sun (retrieved from [27]).

The altitude of the Sun (a_S) denotes the elevation with respect to the PV module. The azimuth of the Sun (A_S) stands for the angle between the Sun and the north direction. The convention adopted here is particularly useful for the locations in the northern hemisphere. For locations below the Equator, it would be more convenient to measure the azimuth with respect to the south direction.

For a complete description of the problem's geometry, it is also necessary to define the orientation of the PV module. The nomenclature is presented in Figure 3.3. The altitude of the module (a_M) is defined as the angle complementary to the module tilt (θ_M), which is measured from the ground level. The azimuth of the module (A_M) is the difference between the azimuth of the normal vector to the PV module and the north direction.

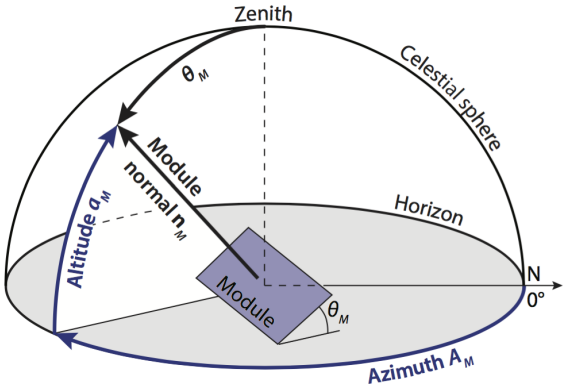

Figure 3.3: Illustration of the angles that describe the orientation of a solar module (retrieved from [27]).

3.1.2. Direct Beam model

The direct normal irradiance (DNI) is the direct light incident on a surface that is placed perpendicular to the Sun. The portion of this irradiance the surface of the module is the direct beam component, and it can

be obtained by multiplying the direct normal irradiance by the cosine of the angle of incidence (AOI) of the solar light on the module:

$$G_M^{dir} = DNI \cdot \cos(AOI) \tag{3.2}$$

The angle of incidence is defined by Equation 3.3:

$$\cos(AOI) = \sin(\theta_M) \cdot \cos(a_S) \cdot \cos(A_M - A_S) + \cos(\theta_M) \sin(a_S) \tag{3.3}$$

Only positive results from Equation 3.3 must be considered. Negative values are only obtained when the sun is behind the module, i.e., when the difference inside the cosine term in Equation 3.3 is larger than 90°.

3.1.3. Diffuse radiation model

The diffuse horizontal irradiance (DHI) is the solar radiation that is scattered by the atmosphere and reaches a horizontal plane on the Earth's surface. By measuring the DHI, it is possible to estimate the diffuse irradiance on a tilted flat surface.

There are several models that have been developed to estimate the diffuse component of the solar radiation incident on a specific surface. Among them the most common ones are:

- Liu and Jordan isotropic diffuse model: This model is the simplest one, and it assumes that the diffuse radiation is constant at every point on the celestial sphere [11].
- Hay and Davies diffuse sky model: It divides the diffuse radiation in the isotropic and the circumsolar components [8].
- Reindl diffuse sky model: this model accounts for the isotropic, the circumsolar component, and also the horizon brightening effect [23].
- Perez diffuse sky model: this model also takes into account the three diffuse components and uses empirical correction factors for more accurate results. This model is described in detail below as it was chosen to carry out the simulations[20].

The model developed by Perez for calculating the amount of diffuse radiation incident on a flat surface tilted an angle θ_M, accounts for three components of the diffuse irradiance: the isotropic component, the circumsolar component, and the horizon brightening.

The circumsolar component is concentrated around the solar disk, and it is the consequence of the forward scattering of the solar beams. The horizon brightening component is due to the radiation concentrated close to the horizon line, this component is positive for clear skies but negative under cloudy conditions. The isotropic component is uniformly distributed on the celestial sphere.

According to the Perez model, the total diffuse irradiance can be calculated as:

$$G_M^{diff} = DHI \cdot \left[(1 - F_1) r_D + F_1 \frac{a}{b} + F_2 \sin(\theta_M) \right] \tag{3.4}$$

In Equation 3.4 r_D is the isotropic diffuse view factor. This factor represents the portion of the sky visible under a free horizon and it depends on the module tilt angle:

$$r_D = \frac{1 + cos(\theta_M)}{2} \tag{3.5}$$

The coefficients a and b are given by the following expressions:

$$a = max\{0, \cos(AOI)\} \tag{3.6}$$

$$b = max\{\cos(85°), \sin(a_S)\} \tag{3.7}$$

The empirical coefficients F_1 and F_2 in Equation 3.4 describe the circumsolar component and the horizon brightening respectively. These coefficients are defined in Equations 3.8 and 3.9 where a_S must be expressed in radians:

$$F_1 = \max\left\{0, \left(f_{11} + f_{12}\Delta + (\frac{\pi}{2} - a_S) f_{13}\right)\right\} \tag{3.8}$$

$$F_2 = f_{21} + f_{22}\Delta + (\frac{\pi}{2} - a_S) f_{23} \tag{3.9}$$

The sky brightness (Δ) present in the previous equations is defined as:

$$\Delta = \frac{DHI \cdot \csc(a_S)}{E_a} \tag{3.10}$$

In order to determine the constants f_{ij} the sky clearness (ϵ) must be defined:

$$\epsilon = \frac{\frac{DHI+DNI}{DHI} + \kappa \cdot (\frac{\pi}{2} - a_S)^3}{1 + \kappa \cdot (\frac{\pi}{2} - a_S)^3} \tag{3.11}$$

where κ is a constant equal to 1.041 for a_s in radians.

In Equation 3.11, E_a is the extraterrestrial radiation, which stands for the solar irradiance at the top of the atmosphere. This value is almost constant but it slightly varies throughout the year reaching a minimum in winter due to the elliptical shape of the Earth's orbit around the Sun:

$$E_a = E_{sc} \cdot \left(1.00011 + 3.422 \cdot 10^{-2} \cos(b) + 1.28 \cdot 10^{-3} \sin(b) + 7.19 \cdot 10^{-4} \cos(2b) + 7.7 \cdot 10^{-5} \sin(2b)\right) \tag{3.12}$$

where $E_{sc} = 1367 \frac{W}{m^2}$ is the solar constant and $b = 2\pi \frac{day\ \ of\ \ year}{365}$.
Finally, the values of the constants f_{ij} are given for different sky clearness ranges in Table 3.1.

Table 3.1: Perez model coefficients

ϵ range	f_{11}	f_{12}	f_{13}	f_{21}	f_{22}	f_{23}
[1;1065)	-0.008	0.588	-0.062	-0.06	0.072	-0.022
(1065;1230]	0.13	0.683	-0.151	-0.019	0.066	-0.029
(1230;1500]	0.33	0.487	-0.221	0.055	-0.064	-0.026
(1500;1950]	0.568	0.187	-0.295	0.109	-0.152	-0.014
(1950;2800]	0.873	-0.392	-0.362	0.226	-0.462	0.001
(2800;4500]	1.132	-1.237	-0.412	0.288	-0.823	0.056
(4500;6200]	1.06	-1.6	-0.359	0.264	-1.127	0.131
> 6200	0.678	-0.327	-0.25	0.156	-1.377	0.251

3.1.4. Ground reflected radiation model

The radiation that is reflected on the ground and reaches the PV module surface is related to the isotropic diffuse view factor and can be approximated with the following equation:

$$G_M^{gnd} = G_h \cdot \alpha_{gnd} \cdot (1 - r_D) \tag{3.13}$$

where G_h is the global horizontal irradiance (GHI) and α_{gnd} stands for the albedo coefficient of the ground surface.

3.1.5. The effect of the skyline profile on the radiation components

All the equations presented above are valid for a free horizon. When an object is placed between the PV module and the Sun, the skyline profile is modified and so are the different components of the solar radiation[24]. The following rules for modifying the different radiation components must be applied:

- The direct beam component and the circumsolar component are null when the module shaded by the skyline profile.
- The horizon brightening component remains unchanged independently of the skyline profile.

- The diffuse isotropic and the reflected irradiance are altered since the sky view factor is different from r_D when the skyline is above the horizon line. The new proportion of the sky that is still visible despite the skyline profile is referred to as the Sky View Factor (SVF), and it can be calculated by numerical integration (see Section 3.1.6).
- The global horizontal radiation (G_h) in Equation 3.13 must be modified according to the following cases:
  - If the Sun is above the skyline and $cos(AOI) > 0$:

$$G_h^{hor} = \frac{DNI + DHI \cdot \left[(1 - F_1) \cdot SVF + F_1 \cdot a/b \right]}{1 - \alpha_{gnd} \cdot r_D^{hor}} \tag{3.14}$$

  - If the Sun is below the skyline:

$$G_h^{hor} = \frac{DHI \cdot \left[(1 - F_1) \cdot SVF \right]}{1 - \alpha_{gnd} \cdot r_D^{hor}} \tag{3.15}$$

Final expression for the incident irradiance

Taking into account the components described above, the total irradiance arriving at the PV module surface can be expressed as:

$$G_M^{tot} = \underbrace{DNI \cdot cos(AOI)}_{G_M^{dir}} + \underbrace{DHI \cdot (1 - F_1) \cdot SVF}_{G_M^{diff-iso}} + \underbrace{DHI \cdot F_1 \cdot a/b}_{G_M^{diff-cir}} + \underbrace{DHI \cdot F_2 \cdot sin(\theta_M)}_{G_M^{diff-hb}} + \underbrace{G_M^{hor} \cdot \alpha_{gnd} \cdot (1 - SVF)}_{G_M^{gnd}} \tag{3.16}$$

3.1.6. Sky View Factor

For this study, the location of the solar modules is in principle undefined. Thus, it is necessary to come up with a simple but effective way for calculating the sky view factor for a wide range of different skyline profiles. For this purpose, the mesh grid proposed by Steyn was used[28]. This grid consists of 244 circular sectors with different weights that total 10.000. By projecting[1] the skyline profile on this grid and diving the sum of the free sectors by the total amount of points, the sky view factor can be determined. In Figure 3.4 an example of the weighted grid from Steyn's work is presented.

The grid has been further subdivided into 2592 sectors (36 rings and 72 slices) to increase the accuracy of the calculation. The modified SVF grid is shown in Figure 3.5. The distribution of weights for each new ring is given by Equation 3.17:

$$\Phi_i = \frac{\pi}{n} \sin\left(\frac{\pi \cdot \left(i - \frac{1}{2}\right)}{2 \cdot n}\right) \cos\left(\frac{\pi \cdot \left(i - \frac{1}{2}\right)}{2 \cdot n}\right) \tag{3.17}$$

where i is the ring number, and n is the total number of rings. It is interesting to notice that the weight of the rings is symmetrical due to the equiangular projection of the sky dome. The weight of each ring can be divided by the number of angular sectors that conform the annulus to obtain the weight of each slice.

When a PV module is tilted, part of sky view factor is lost because of the projection of the plane of incidence on the sky view factor grid. In Appendix B the derivation of the projection of the plane of incidence on the SVF grid is described in detail. While the orthographic projection of the tilted plane of incidence on the SVF grid results in half an ellipse, the equiangular projection results in half an ellipsoid as shown in Figure 3.5. The SVF calculated using the grid for a plane tilted 35° totals 0.91, while for a tilt angle of 75° the SVF equals 0.63.

The SVF values calculated using the SVF grid should yield the same results as the isotropic diffuse view factor given by Equation 3.5. In Figure 3.6 the comparison between both methods for calculating the SVF is depicted: the differences due to the discretization of the grid have a negligible effect on the SVF results (deviations are smaller than 0.01%), and therefore it was not necessary to subdivide the grid any further.

[1] Steyn method uses an equiangular projection.

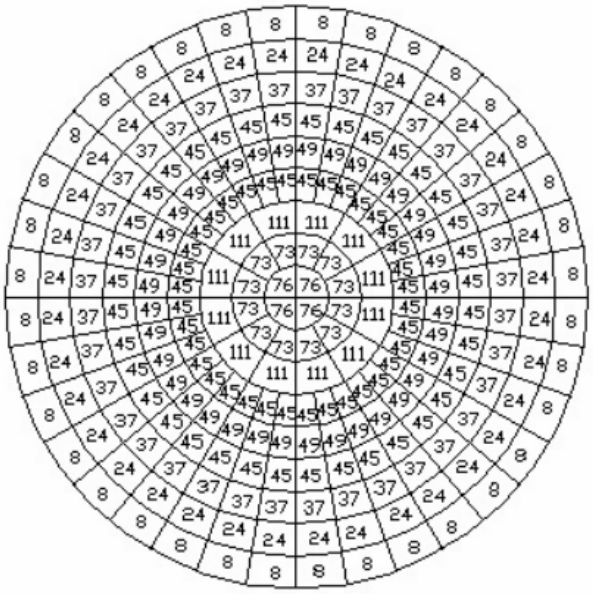

Figure 3.4: SVF grid for MapInfo analysis, developed by Souza, Rodrigues & Mendes[10]

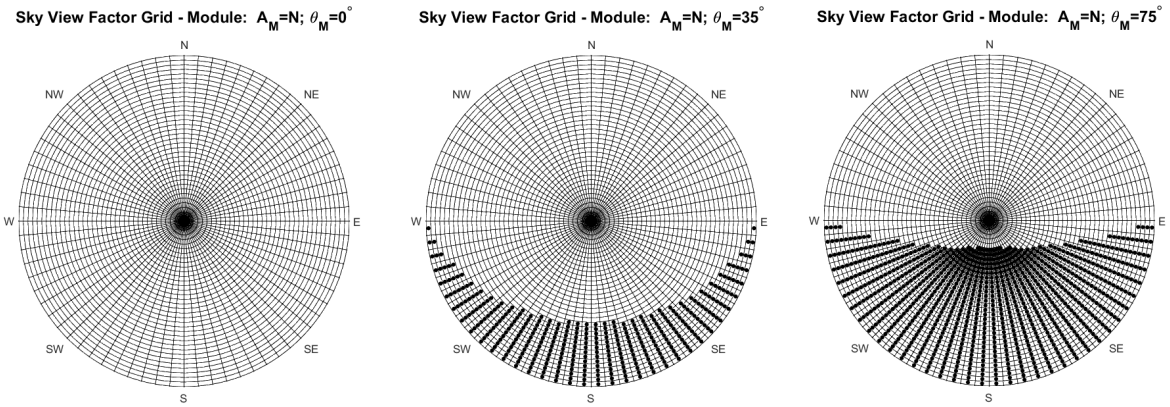

Figure 3.5: Left: Modified SVF grid. Center: Effect of a tilt of 35° on the SVF grid. Right: Effect of a tilt of 75° on the SVF grid. The black dots represent the sectors of the sky blocked by the tilted plane.

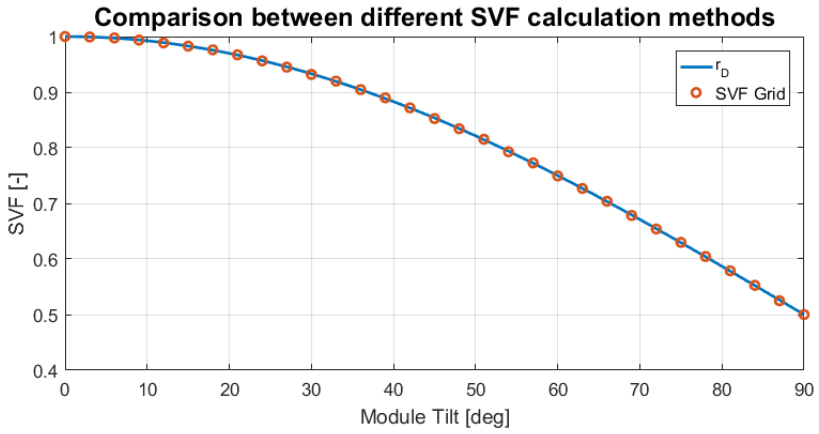

Figure 3.6: Comparison between the methods for calculating SVF using Equation 3.5 (in blue) and the SVF grid in Figure 3.4 (red)

The main advantage the SVF grid offers when compared to Equation 3.5, is that it allows quantifying the loss in the SVF due to the skyline profile. This can be achieved by overlapping the projection of the skyline profile on the projection of the tilted plane of incidence. In Figure 3.7 the TU Mekelpark bus stop skyline profile projected onto the SVF grid is shown for the case when the panel is placed flat on the ground ($\theta_M = 0°$).

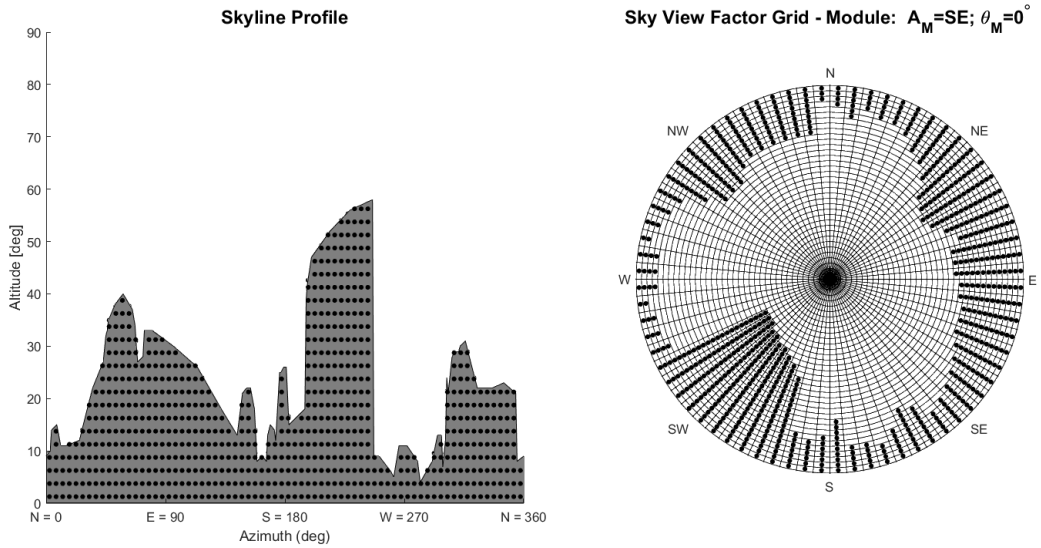

Figure 3.7: Skyline profile at TU Mekelpark bus stop for a module placed flat on the ground. The black dots represent the shaded blocked sectors of the sky.

In Figure 3.8 the skyline profile and the grid at the same location are shown for the a panel facing southeast and tilted 75°. It can be seen that on the left plot, some black dots are above the skyline. These dots represent the additional part of the sky that is covered by the module's tilt. The calculations indicate that the SVF drops from 0.79 for a flat module at TU Mekelpark to 0.51 for the case when the panel is tilted.

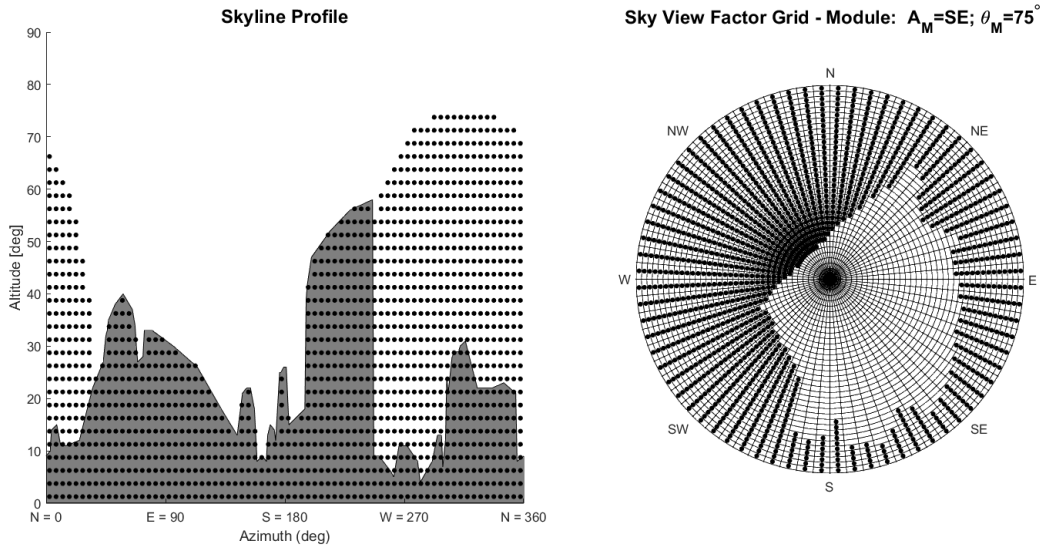

Figure 3.8: Skyline profile at TU Mekelpark bus stop for a module facing Southeast and tilted 75°

Finally, in Figure 3.9, the portions of the sky view factor lost due to the tilt angle and the skyline profile are compared for a module placed in TU Mekelpark facing southwest and north. When the module is facing southwest, the drop in the SVF is more significant because the tall EWI building is precisely in front of the module. On the other hand, when the PV panel is facing north, the tall building is behind the solar panel and its position overlaps with the projection of the plane of incidence.

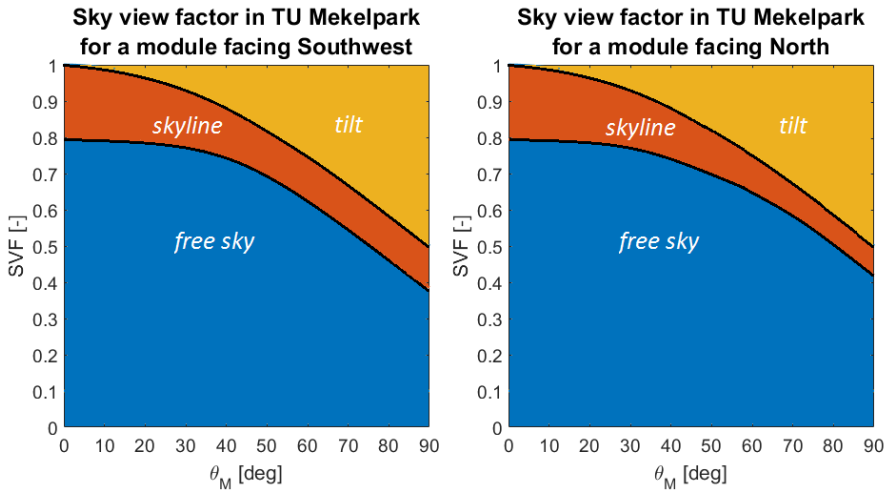

Figure 3.9: SVF loss as a function of the tilt angle

3.2. Irradiance framework B

A framework based on sky and sensitivity maps developed by Santbergen was applied to validate framework A[25]. This alternative method is based on the Perez sky luminance model, and takes into account the 3D geometry of the PV module and the surroundings, as well as the optical properties of the surfaces involved.

The sensitivity maps created using LightTools, and the sky maps created using meteorological data, are combined to determine the incident radiation on a given surface.

A sensitivity map represents the susceptibility of a specific surface to radiative power coming from a specific direction. A sky map is a 3D representation of the luminance distribution on the sky at a particular moment.

In Figure 3.10 a sensitivity map and an integral sky map are shown. The sensitivity map shows values higher than 1, which means that when the Sun is in those positions, not only the direct light from the Sun is absorbed, but also the light that is reflected by other objects reaches the surface. An integral sky map is the sum of sky maps for the same location, the addition of multiple sky maps results in the analemmas visible in Figure 3.10.

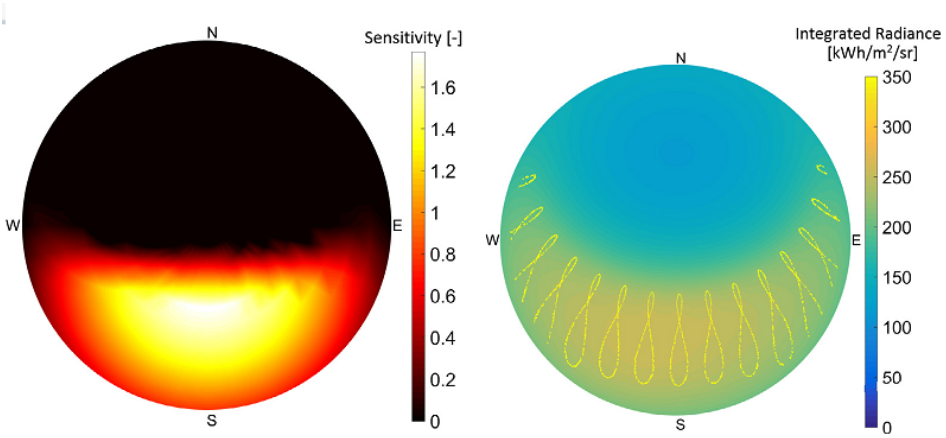

Figure 3.10: Examples of a sensitivity map (left) and a integral sky map for Eindhoven (right) (Retrieved from [25])

Once the sensitivity map of a surface is calculated, and the sky map at a given instant is generated, the irradiance on a surface can be determined by calculating the following integral over the skydome:

$$G_M^{tot} = \int \textbf{Sky map} \cdot \textbf{Sensitivity map} \cdot d\Omega \tag{3.18}$$

In Equation 3.18, $d\Omega$ is a differential area of the sky dome.

This framework, in opposition to framework A, allows to accurately calculate the irradiance on a concave PV module and on a PV modules that are surrounded by highly reflective surfaces. Although this is a more accurate method, it is computationally expensive, and therefore it cannot be applied to simulate all the cases required for this study.

3.3. Thermal model

The temperature of a material describes the kinetic energy of its composing atoms. When the temperature of a semiconductor raises, the atoms start vibrating faster, and the inter-atomic distance increases causing a the band-gap energy to drop. The decrease of the band-gap energy causes an elevated absorption of photons, and therefore an increment in the short circuit current of the cell.

However, an increase in temperature has also other effects on a semiconductor device. In a mono-Si solar cell, the phenomenon through which the generated charge carriers move across the bulk is diffusion. In the case of a p-type c-Si solar cell, the minority carriers generated on the p-type base (electrons) diffuse until they reach the depletion region and are dragged by the electric field to the quasi-neutral region on the n-type layer. The diffusion length, i.e., the average distance a minority carrier can travel before being annihilated, depends on the charge carrier mobility and the minority carrier lifetime. With increasing temperature, the concentration of phonons in the crystalline lattice increases causing scattering of the charge carriers and hence reducing their mobility.

Additionally, the minority carrier lifetime depends on multiple recombination processes. For Si is an indirect bandgap material, the predominant recombination method is Auger recombination, which is also affected by temperature. The decrease in the diffusion length causes a drop in charge collection, an effect that opposes to that one mention in the first paragraph. For this reason, the short-circuit current increases with temperature but only slightly.

On the other hand, the open circuit voltage of a solar cell is negatively affected by an increase in temperature. The open circuit voltage depends on the saturation current density, which increases at higher temperatures as a consequence of the elevated intrinsic carrier concentration.

All these phenomena bring out the importance of knowing the temperature of a solar cell to estimate the yield of the PV module. In the simulations presented in this thesis, a fluid-dynamic model[27] has been used to derive the cell temperature and it is explained subsequently.

The fluid-dynamic model, takes into account the radiation coming from the Sun, the convective heat exchange between the module and the air, and the heat radiated by the module (refer to Figure 3.11). This model neglects the conductive heat transfer between the module and the mounting structure.

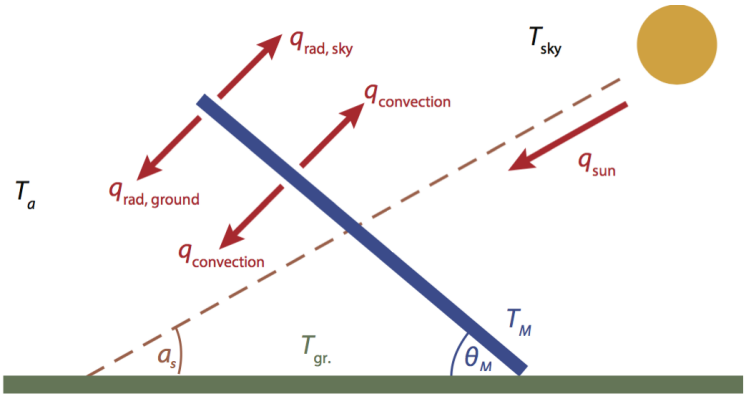

Figure 3.11: Thermal model and heat fluxes (retrieved from [27])

Starting from the heat balance, the temperature of the module can be obtained using a recursive algorithm.

First, the heat transfer coefficient on the top side of the PV module (h_c^{top}) must be determined. The forced and free convection contribute to this coefficient:

$$h_c^{top} = \left(h_{forced}^{top\ 3} + h_{free}^{top\ 3}\right)^{\frac{1}{3}} \tag{3.19}$$

The forced convection heat transfer coefficient on the top side of the module (h_{forced}) depends on the wind speed (w), the Prandtl number (Pr), the density (ρ_{air}) and heat capacity (c_{air}) of the air, as well as on the type of flow around the PV module, which can be laminar or turbulent depending on the Reynolds coefficient (Re):

$$h_{forced}^{top} = \begin{cases} \frac{0.028Re^{-0.2}}{Pr^{0.4}} \cdot \rho_{air} \cdot c_{air} \cdot w, & if \quad Re \geq 1.25 \cdot 10^5 \\ \frac{0.86Re^{-0.5}}{Pr^{0.67}} \cdot \rho_{air} \cdot c_{air} \cdot w, & if \quad Re < 1.25 \cdot 10^5 \end{cases} \tag{3.20}$$

The Reynolds number depends on the hydraulic diameter of the solar module (D_h), which in turn depends on the length (L) and width (W) of the module:

$$D_h = \frac{2 \cdot W \cdot L}{W + L} \tag{3.21}$$

The free convection heat transfer coefficient on the top side of the module (h_{free}^{top}) is a function of the hydraulic diameter, the Nusselt number and the heat conductivity of the air (κ_{air}):

$$h_{free}^{top} = \frac{Nu \cdot \kappa_{air}}{D_h} \tag{3.22}$$

The Nusselt number can be calculated as:

$$Nu = 0.21 \cdot (Gr \cdot Pr)^{0.32} \tag{3.23}$$

The Grashof number (Gr) depends on the module's hydraulic diameter, the module (T_M) and air temperature (T_{air}), the gravitational acceleration (g), the volumetric expansion coefficient (β_{air}), the kinematic viscosity of the air (ν_{air}), and the module tilt angle (θ_M):

$$Gr = \frac{g \cdot \beta_{air} \cdot (T_M - T_a) \cdot D_h^3}{\nu_{air}^2} \cdot sin(\theta_M) \tag{3.24}$$

Once h_c^{top} is determined, the heat transfer coefficient on the back side of the module can be calculated using:

$$h_c^{back} = R \cdot h_c^{top} \tag{3.25}$$

where R is defined by the following equation:

$$R = \frac{\alpha_{gnd} \cdot G_M^{tot} - h_c^{top}(T_{INOCT} - T_a) - \epsilon_{top}\sigma\left(T_{INOCT}^4 - T_{sky}^4\right)}{h_c^{top}(T_{INOCT} - T_a) + \epsilon_{back}\sigma\left(T_{INOCT}^4 - T_{sky}^4\right)} \tag{3.26}$$

In Equation 3.26, ϵ is the module emissivity, σ the Stefan-Boltzmann constant, T_{INOCT} is $18°C$ higher than the nominal operating cell temperature (NOCT), and T_{sky} depends on the cloud coverage factor (N):

$$T_{sky} = \begin{cases} T_a, & if \quad N > 6okta \\ 0.0552 \cdot T_a^1.5, & if \quad N \leq 6okta \end{cases} \tag{3.27}$$

The overall convective heat transfer coefficient (h_c) is the sum of the top and back heat transfer coefficients:

$$h_c = h_c^{top} + h_c^{back} \tag{3.28}$$

Other two heat transfer coefficients are considered in this model for describing the heat exchange by radiation between the module and the ground (h_r^{gr}), and the module and the sky (h_r^{sky}):

$$h_r^{gr} = \epsilon_{back}\sigma\left(T_M^2 + T_{gr}^2\right)\left(T_M + T_{gr}\right) \tag{3.29}$$

$$h_r^{sky} = \epsilon_{top}\sigma\left(T_M^2 + T_{gr}^2\right)\left(T_M + gr\right) \tag{3.30}$$

Subsequently, the temperature of the module can be calculated using Equation 3.31. The resulting value must be used to recalculate the heat transfer coefficients iteratively until T_M converges.

$$T_M = \frac{\alpha_{gnd} G_M^{tot} + h_c T_a + h_r^{sky} T_{sky} + h_r^{gr} T_{gr}}{h_c + h_r^{sky} + h_r^{gnd}} \tag{3.31}$$

In the fluid-dynamic model under consideration [27], the air density, the viscosity, and the Prandtl number are assumed to be constant, however, these are also function of the air temperature[2]. For the simulations carried out in this work, the dependence of each of these parameters has been approximated with a polynomial function.

The nominal operating cell temperature (NOCT) of the PV modules was determined experimentally. However, as explained in Appendix A, the nominal operating module temperature (NMOT) is a better indicator of the thermal performance of a solar panel. In consequence, the NOCT in Equation 3.26 has been replaced for the measured NMOT value.

In Figure 3.12 the results of the module temperature simulations are shown. The simulations at a constant tilt angle show that when the irradiance level is low, the module temperature is below the ambient temperature and higher wind speeds increase the module temperature. On the other hand, at high irradiance levels, the wind contributes to reducing the module temperature. Moreover, from the simulations at different tilt angles, it can be observed that the lower the tilt, the higher the temperature of the module, and also that for high wind speeds the temperature of the module becomes independent of the tilt angle.

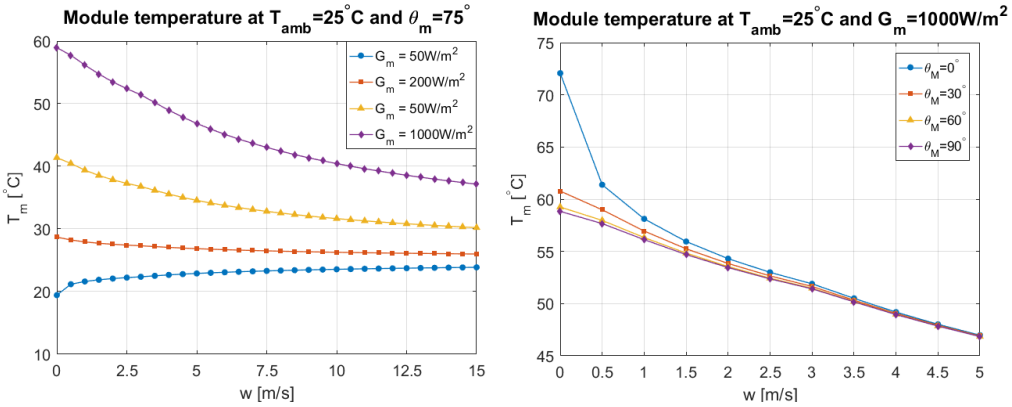

Figure 3.12: Left: Variation of the temperature with the irradiance and wind speed. Right: Variation of the temperature with the module tilt and wind speed

As a final note to the thermal model, it must be highlighted that this model was originally developed for PV panels mounted on a rack. In such conditions the contact area between the module an the rack is low, and therefore the heat transfer by conduction can be neglected. If the module is directly mounted on a metallic surface, the surface acts as a heat sink, reducing the temperature of the module. This would improve the performance of the module, and by using this thermal model, the simulated PV performance would be slightly worse than the actual one.

3.4. Electrical model

The temperature of a PV module and the irradiance reaching its surface are needed to calculate the electrical power produced by the solar cells.

The five parameter model presented in Figure 3.13 was used[19] to calculate the voltage and current generated by a solar cell, and to determine how they depend on the irradiance and the cell temperature. The model consists of one current source that represents the photo-generated current (I_{ph}), one diode whose ideality factor (A) represents the multiple recombination processes, a shunt, and series resistances.

[2]The heat capacity and the thermal conductivity are also functions of the temperature, but in the case of air, these are less sensitive to temperature changes than other parameters.

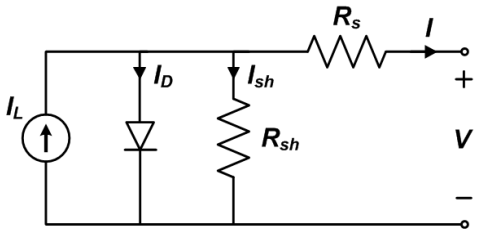

Figure 3.13: 5-point equivalent circuit of a solar cell

In this model, the series and shunt resistances are assumed to be independent of the light intensity. The shunt resistance represents a parallel conductive path across the cell junction as a consequence of imperfections close to the junction and on the device surface as well as leakage current across the edge of the cell. The series resistance mainly represents the ohmic resistance in the semiconductor materials and the contact resistance of the front and back surfaces.

The photo-generated current is considered to be equal to the cell short-circuit current at standard test conditions (STC) and proportional to the total irradiance reaching the surface of the solar cell:

$$I_{ph} = \frac{G_m}{G_m^{STC}}\left(I_{SC}^{STC} + \kappa_{I_{SC}} \cdot (T - T^{STC})\right) \tag{3.32}$$

In Equation 3.32 $\kappa_{I_{SC}}$ stands for the short circuit thermal coefficient of the solar cell, E_g the bandgap energy of silicon, and I_S the dark saturation current of the diode. The latter two parameters depend on the temperature of the cell as indicated by the following equations:

$$I_S = I_S^{STC} \cdot \left(\frac{T}{T^{STC}}\right)^3 \cdot e^{\frac{q \cdot E_g}{k_B \cdot A} \cdot \left(\frac{1}{T^{STC}} - \frac{1}{T}\right)} \tag{3.33}$$

$$E_g = E_{g0} - \frac{\alpha_{gap} \cdot T^2}{T - \beta_{gap}} \tag{3.34}$$

For silicon $E_{g0} = 1.169eV$, $\alpha_{gap} = 4{,}9 \cdot 10^{-4} \frac{eV}{K}$ and $\beta_{gap} = 655K$. The saturation current at standard test conditions (I_S^{STC}) can be calculated using the following formula:

$$I_S^{STC} = I_{SC}^{STC} \cdot \left(e^{\frac{q \cdot V_{OC}^{STC}}{k_B \cdot T \cdot A}} - 1\right)^{-1} \tag{3.35}$$

Finally, using the circuit diagram and the equations presented above, the I-V curve of a solar cell can be determined by recursively solving Equation 3.36:

$$I = I_{ph} - I_s\left(e^{\frac{q \cdot (V + I) \cdot R_s}{k_B \cdot T \cdot A}} - 1\right) - \frac{V + I \cdot R_s}{R_{sh}} \tag{3.36}$$

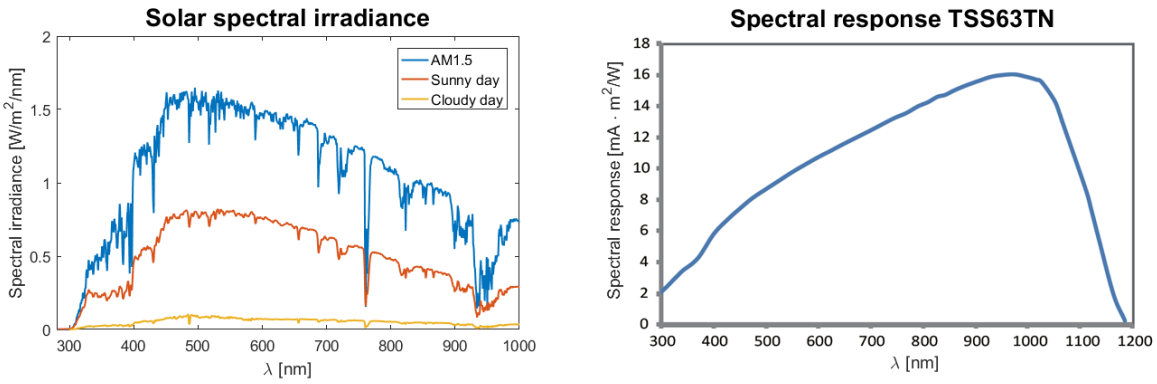

Figure 3.14: Left: Solar spectral irradiance (GHI). Right: Spectral response of a p-type mono-Si solar cell

The 5-point model disregards the spectral characteristics of the incident light and the spectral response of the solar cell. Figure 3.14 shows how the solar spectrum during a typical sunny and cloudy day differs from the spectrum consider in STC[3], and the spectral response of a typical mono-Si solar cell. It is evident that the solar spectrum is not simply scaled up or down with the total irradiance, and that the contribution of the different wavelength bands changes from a sunny to a cloudy day. Clearly, to develop a more precise electrical model of a solar cell the wavelength dependence should be taken into account. However, the five parameter model is considered an accurate approximation for the purposes of this study.

3.4.1. Parameters estimation

The five parameters that characterize the solar cells used by Kameleon Solar have been estimated from the curves provided by the cell's manufacturer. Furthermore, the values of all the parameters have been contrasted with the values reported in the literature for p-type mono-Si commercial solar cells. The parameters that best fit the data given by the manufacturer are:

- $I_{SC}^{STC} = 9.512\ A$ & $V_{OC}^{STC} = 0.663\ V$
- $I_{S}^{STC} = 8.73$ nA & $A = 1.24$
- $R_{sh} = 50\ \Omega$ & $R_s = 1.1\ m\Omega$

Figure 3.15 shows the I-V and P-V curves of the simulated solar cell under standard test conditions. The maximum power point current equals 8.989 A (0.14% lower than the reported value on the datasheet), and the maximum power point voltage is 0.560 V (0.18% higher than the reported value on the datasheet).

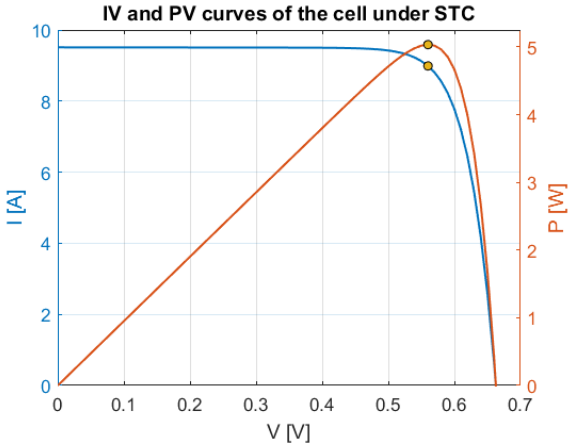

Figure 3.15: Solar cell performance under STC

The I-V and P-V curves under 1000 W/m^2 and different cell temperatures are shown in Figure 3.16. As it was expected, the open circuit voltage and the maximum power of the cell drop with increasing temperatures, whereas the short circuit current slightly increases at higher temperatures.

From the simulations at between $0°C$ and $50°C$, the temperature coefficients of the solar cell were obtained. The calculated temperature coefficients and the reported values by the manufacturer are compared in Table 3.2. As it can be seen, the current and the power temperature coefficients are within the limits given by the manufacturer, only the open circuit voltage is 7% lower than the reported values.

3.4.2. From the cells to the module

When cells are connected in series (or parallel) and laminated to build a module, the resulting maximum power of the PV module is lower than the sum of the power of the cells. This loss in efficiency is usually referred to as cell-to-module losses (CTM) and is generally above 10% relative [7].

CTM losses in a c-Si module are mainly caused by:

[3] Figure 3.14 shows the spectral irradiance between $280nm$ and $1000nm$. Nevertheless, the Sun radiates a considerable amount of power with wavelengths up to $2500nm$: 80.5% of the radiant power is between $280nm$ and $1100nm$ while 18.8% of the power is found between $1100nm$ and $2500nm$.

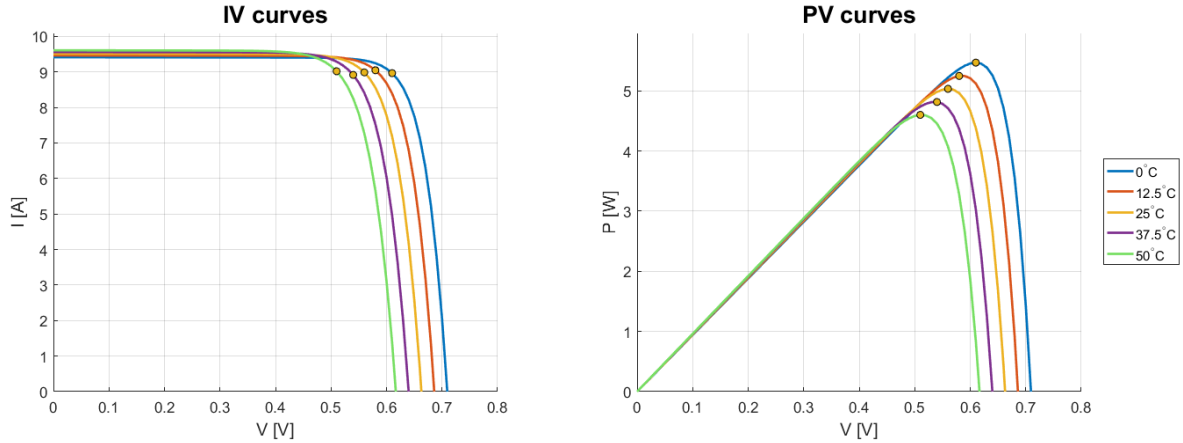

Figure 3.16: Solar cell performance under different temperatures

Table 3.2: Simulated and reported temperature coefficients

Thermal coefficient	Result	Datasheet
$\kappa_{I_{SC}}$ $[mA/°C]$	3.88	3.89 ± 0.59
$\kappa_{V_{OC}}$ $[mV/°C]$	-1.84	-1.980 ± 0.039
$\kappa_{P_{mpp}}$ $[mW/°C]$	-17.36	-17.754 ± 0.72

- Optical power losses: as a consequence of light reflection in the front transparent sheet and the encapsulant.
- Cells mismatch: due to slightly different properties of the cells or different illumination conditions.
- Ribbon resistance: the resistances of the metallic ribbon and the interconnections contribute to the series resistance of the module.
- Junction box losses: due to the connections in the junction box and the bypass diode.

The 10-cell KS-Flex PV module was tested using an AAA flash solar simulator[4] and the measurements were compared with a Simulink simulation where a by-pass diode was connected across 10 PV cells in series. The results of the comparison are shown in Figure 3.17. The slope of the I-V curve close to the open circuit voltage is a direct indicator of the series resistance of the module, and it equals 10.5 Ω, a value that is substantially larger than the sum of the series resistances of the cells. Furthermore, the maximum power of the actual module is 6.9 W lower than in the simulations, which means that CTM losses are 13.6% relative.

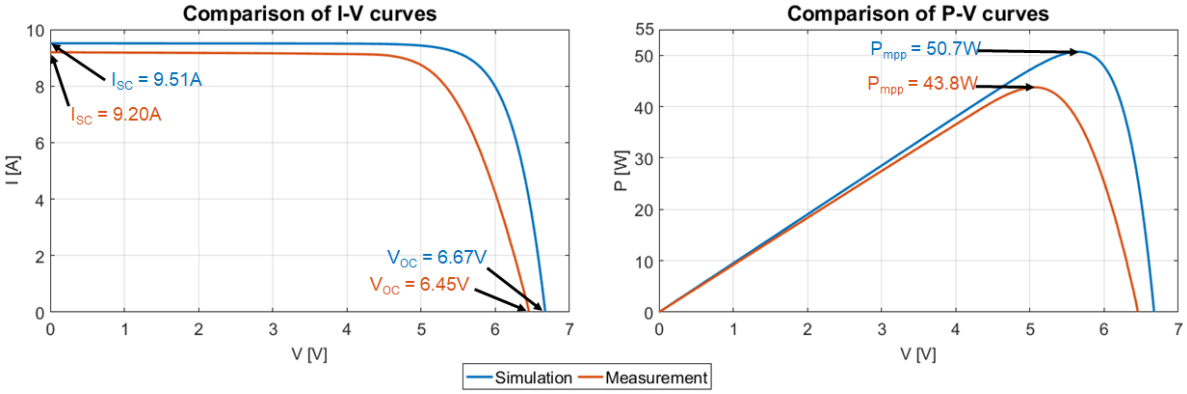

Figure 3.17: Comparison between simulated and measure I-V and P-V curves for the 10-cell KSFlex PV module under STC.

[4] Spi-Sun Simulator 3500SLP

To conclude, a simplified electrical model[12] was used to determine the required storage capacity in Chapter 5. The disadvantage of this model is that it can be used to calculate the power generated, but to know the voltage and current of the panel a fill factor value must be assumed. According to this model, the efficiency of a PV module can be calculated using Equation /

$$\eta(T_M, G_M) = \eta(25^\circ C, G_M) \cdot \Big(1 + \kappa_\eta (T_M - 25^\circ C)\Big) \tag{3.37}$$

where κ_η is the efficiency temperature coefficient and can be derived from the maximum power temperature coefficient of the module ($\kappa_{P_{mpp}}$).

4

PV designs and simulations

4.1. The design of the kiosks

The design of kiosk is based on three central premises. First, the footprint of the structure has to be minimized, and the depth of the structure must be shorter than 1 m since the pavement in most bus stops is 1.5 m wide. In the second place, the most expensive and lifetime-limited component of the system is the battery, and consequently, storage capacity must be minimized. Finally, two Infotainment Spots, with and without a tracking system, are to be designed using the same base structure.

The additional energy yield analysis of the PV bus shelter is presented in Appendix H.

4.1.1. Basic choices

The first step in the design process of any PV system is to estimate the required peak power. In this regards, the following assumptions were made:

- The kiosk will power a tablet which consumes approximately 10 W during operation and 2 W while in stand-by mode. The tablet will be used 90 minutes per day, which results in a total annual consumption of around 22 kWh.
- The kiosk will include a mobile phone charger. The charger will be used around 45 minutes per day. The power consumed by the charger is 5 W, and hence the annual consumption is 1.4 kWh.
- The kiosk will be illuminated with a 0.5 W LED for 10 hours a day. This implies a annual consumption of 1.8 kWh.
- The energy conversion efficiency (considering the battery and the charge controller) is assumed to be 85%. Therefore, the total energy required during the year equals 30 kWh.
- In the Netherlands, for a module tilted 36° there are between 2.7 and 3.1 equivalent sun hours (ESH) per day [27]. It has been assumed that for a module tilted 75° the equivalent sun hours drop to 2. Considering a conversion efficiency of 20% the minimum active area required is 0.2 m^2, which is equivalent to nine 6-inches solar cells.
- With only 9 cells, the system would require an extremely large battery capacity to store the energy during the summer for the winter. Since in the Netherlands the irradiance during summer is around 7 times larger than in winter, it is at least necessary to duplicate the required area to obtain a reasonable storage capacity in terms of cost and volume.

From this reasoning, it was concluded that at least 18 solar cells (6-inches and 20% efficient) were required for the design.

4.1.2. The new Infotainment Spot

Different shapes and tracking systems have been explored. Some of the designs considered are shown in Figure 4.1.

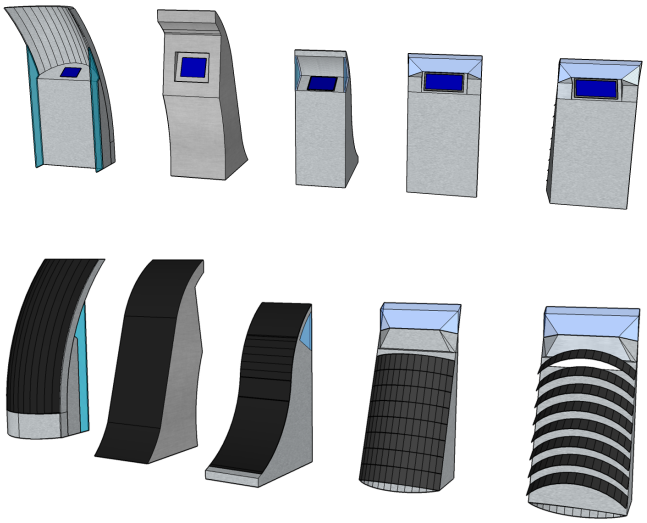

Figure 4.1: Different designs explored

Finally, in agreement with Kameleon Solar, it was decided to implement the kiosk presented in Figure 4.2. This structure has a footprint of 0.4 m wide by 0.6 m deep. The height of the structure is 2 m, and the available space for storage is approximately 120 dm^3.

The structure is made of 2mm thick stainless steel sheets, weights 60 kg, and can stand wind gusts up to 100 km/h in any direction. The positioning of the screen was decided according to a previous study based on the height of an average Dutch person[31]. The screen was placed at 1.3 m above the ground and the inclination is 65°.

The static version consists of 2 PV modules: one curved module of 10 cells and a flat module of 14 cells, which add up to 121 W_p. The flat module is tilted 75°, and the smaller module was curved to a bending radius of 1 m, which is the maximum curvature that Kameleon Solar recommends for their KS Flex PV modules. The kiosk has a pocket on the side to charge a mobile phone, and a LED lamp above the screen for illumination during the night.

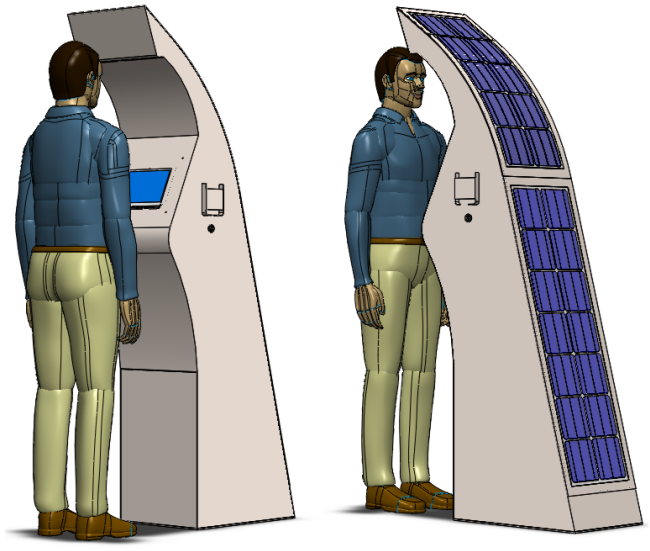

Figure 4.2: Final design of the kiosk with a 1.85m tall human body for reference

The design with a tracking system (shown in Figure 4.3) consists 3 PV modules: the same curved module as for the static design (10 cells), and two smaller modules of 6 series-connected cells placed on two flaps that

can be tilted to follow the Sun. The peak power of this design is 111 W_p.

The tracking system was designed taking care of never exposing the inside of the structure: when the flaps separate from the structure, the shape of the back part of the flaps covers any possible access to the actuators and other components inside the structure.

The available space for storage with the tracking system is restrited to 40 dm^3, due to the volume occupied by the flaps inside the structure. To compensate for this restriction, the volume for storage inside the kiosk can be increased by projecting the base below the ground level: by expanding the base only 20 cm below the ground level, the storage capacity can be increased to 85 dm^3 (see Figure 4.4).

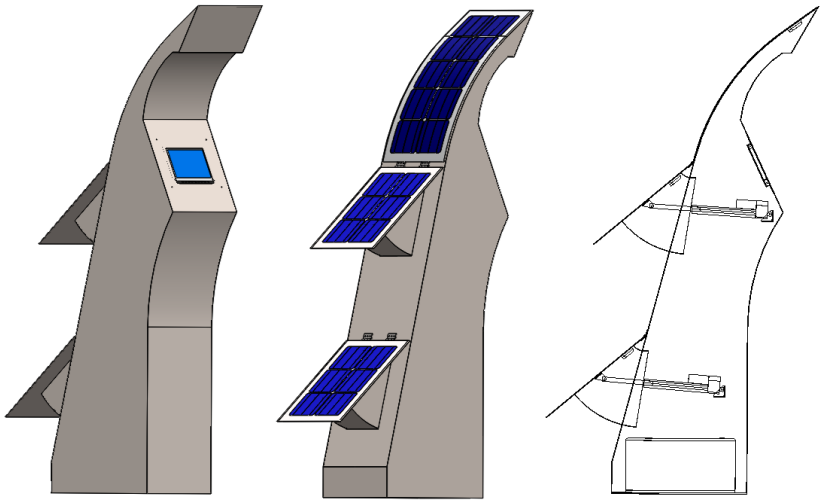

Figure 4.3: Final design of the kiosk with a tracking system

4.1.3. The tracking system

In the Netherlands, the maximum altitude the Sun reaches on the 21st of June is almost 65°, and the highest altitude reached on the 21st of December is around 15°. The lower altitude value was used to determine the tilt of the back of the kiosk (75°). The highest altitude value indicates that the optimal tilt of a PV module during summer is close to 25°.

If the panels are to be tilted at 25°, the flaps have to rotate 50°. However, the angular span of the tracking system is limited by the dimensions of the structure and also for aesthetic reasons. Additionally, a wider angular span implies a larger separation between the flaps to avoid mutual shading. After multiple redesign steps, in which the energy yield was taken into account, the chosen angular span was 40°. With this angular span the module can be tilted down to 35°. In Figure 4.4 the final design of the tracking system is presented. It is shown that when the flaps are completely opened the footprint increases by 50%.

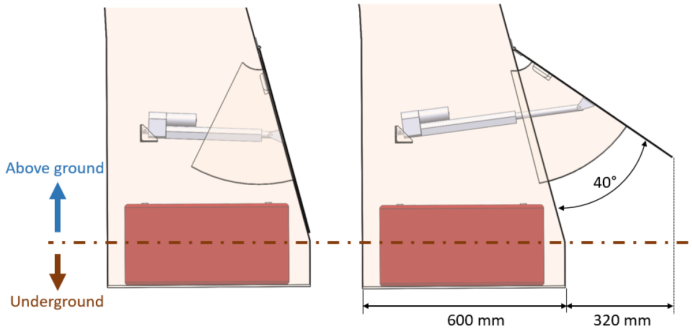

Figure 4.4: Detail of the tracking system. On the left the system is shown as it looks in winter, while on the right the position of the flaps in summer is depicted.

Since the KS Flex PV modules only have one bypass diode and the PV panels are connected in series, it

is essential to avoid mutual shading between the flaps to maximize the energy yield. For this reason, the minimum separation between flaps was calculated using the formulas presented in Appendix C.

Assuming the Sun can reach a maximum altitude of 65° and taking into account the dimensions of the panels, the minimum separation between flaps is 24 cm.

A third aspect that was investigated about the tracking system, is the advantage of implementing a discrete tracking system compared to a continuous tracking system. A continuous tracking system, one that adjusts the tilt at every moment during the day, is the best option to maximize the produced PV power. Nevertheless, this implies multiple disadvantages, among them, a large energy consumption by the linear actuators and the unnecessary wear of the movable parts. Alternatively, a tracking system that only changes the tilt once every month could reduce the consumption and the deterioration, with a minimum loss of the harvested energy.

The optimum tilt angle for every month in the Netherlands was calculated to calculate both options. In Figure 4.5 the monthly irradiation on a module for a module facing South in Delft at different tilt angles is shown. In order to make the kiosk location-independent, the average angles using five different locations in Holland and Utrecht were calculated. The optimization was repeated for eight different module orientations. In particular, for the South direction, the resulting angles are presented in Table 4.1. These values were constrained according to the angular restrictions imposed by the structure.

From Table 4.1 it is noteworthy that from November until January the best tilt angle is almost equal to the structure tilt. This match is essential for minimizing the required storage capacity.

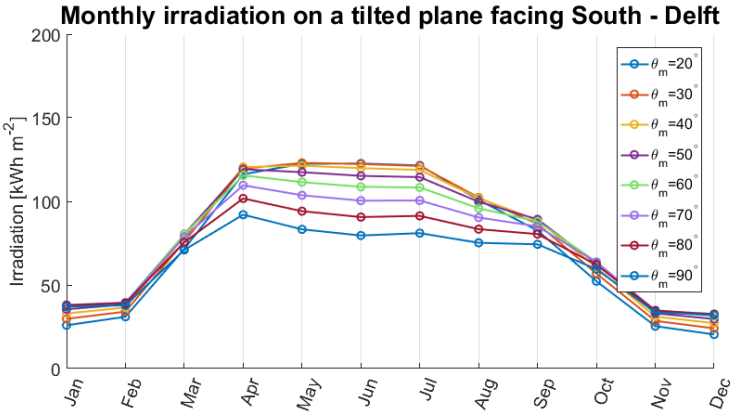

Figure 4.5: Optimum module tilt in Delft for every month during the year calculated using Meteonorm hourly data

Table 4.1: Averaged optimum tilt angles for a module in Holland/Utrecht facing South

Month	J	F	M	A	M	J	J	A	S	O	N	D
θ_{M-opt}	75°	68°	54°	39°	28°	24°	24°	33°	47°	63°	73°	78°

Aiming to compare the continuous and the discrete tracking methods, it was assumed that it is possible to implement a tracking algorithm always capable of finding the tilt that maximizes the generated power. For the simulations of the continuous tracking system, the tilt was modified every hour since that is the maximum frequency of the available meteorological data.

The results of the comparison indicate that considering the power generated by two flaps the extra energy generated by the continuous tracking system is 110 Wh in 1 year. In relative terms this equals to a 0.1% increment in the energy yield. If the linear actuator is moved five times per day in average, and it consumes 0.02 Wh every time it moves[1], the extra energy consumed by both flaps with a continuous tracking system is approximately 70 Wh.

Leaving aside the complexity of implementing the tracking algorithm, it is considered that the energy gain is not high enough to opt for a continuous tracking system. Therefore the discrete tracking version prevailed.

[1] A typical linear actuator for this application would consume 2 A at 12 V, and it is assumed that it is active for 3 seconds to orient the panel.

Complementary to the analysis in the Netherlands, the simulations were repeated for Madrid where the proportion of direct beam radiation is higher than in the Netherlands. The optimum monthly angles for Madrid were calculated to determine the differences between a continuous and a discrete tracking system (refer to Figure 4.6). The net gain in using a continuous tracking system was 300 Wh. Even in this location, the benefit is too low to support the selection of a continuous tracking system.

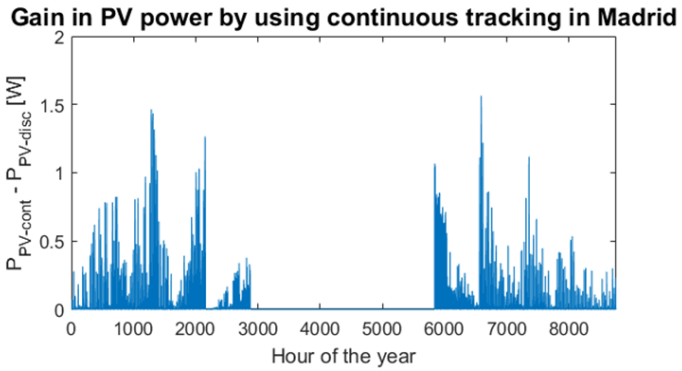

Figure 4.6: Difference between the PV generated power using a continuous and a discrete tracking system in Madrid for the PV modules facing south

4.2. Simulation results

The models presented in Chapter 3 were applied to calculate the energy yield of the kiosk. These models were developed for flat surfaces, and cannot be directly applied to calculate the yield of a curved PV module. For this reason, the curved module was subdivided into five flat segments, each of them coincident with a different row of cells on the curved panel[31].

For each of the simulations, the temperature and the irradiance on each segment of the structure were calculated using meteorological data obtained from Meteonorm. All the parameters used for the simulations are presented in Appendix D.

Figures 4.7 and 4.8 show the irradiance on each segment of the structure facing South during the 13th of July of 2015 between 9:00 and 18:00. In Figure 4.9, the GHI, DHI and DNI measurements for ever hour are given for reference. These results correspond to a free horizon, i.e., the sky view factor is only affected by the module's tilt angle.

From Figures 4.7 and 4.8, it is evident that the top cells of the curved module always receive a higher irradiance than the lower cells because the top cells are better aligned with the altitude of the Sun in summer. However, it is important to realize that since the curved module does not have a bypass diode per cell, the power output power of the module is limited by the lowest irradiance value. This means that when the Sun is low, the top cells determine the module output current, and the lower cells become restrictive for higher Sun altitudes.

As expected, the tracking flaps receive a higher irradiance than the flat module on the static kiosk. Specifically, at midday, the irradiance on the flaps of the kiosk is around 30% higher.

It is also interesting to notice from Figure 4.8 that at 13:00 the top segment of the curved panel receives a higher irradiance than the flaps that track the Sun. This is because the flaps have reached their minimum tilt (35°), while the altitude of the Sun is 59.7°. The tilt of the top segment of the curved module is 31.5° which results in a smaller angle of incidence when compared to the flaps.

Figures 4.10, 4.11 and 4.12 show the calculated and measured temperatures for the same day. Clearly the temperature of the segments increases with the irradiance level.

4.2.1. Performance of the kiosks with and without a solar tracker

The results of the simulations allowed to compare the performance of the kiosk with and without a tracking system regarding the annual energy yield. As mentioned before, the kiosk without a tracking system has 24 cells of 5.03 W_p each, while the system with the tracking system has 22 cells because the flaps must be separated. In this comparison, a kiosk without a tracking system and 22 cells, has been used as a reference to

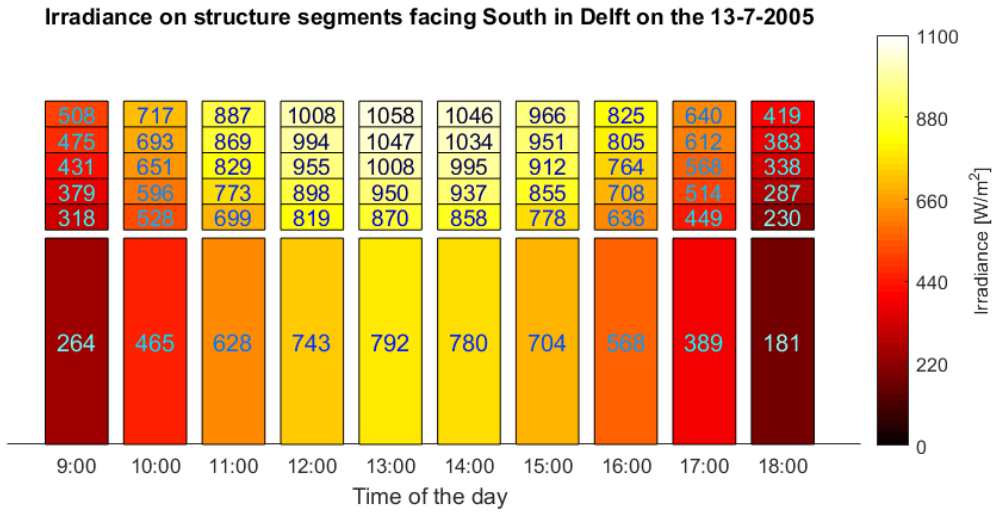

Figure 4.7: Irradiance on each segment of the kiosk without tracking and facing South on the 13th of July of 2005 in Delft

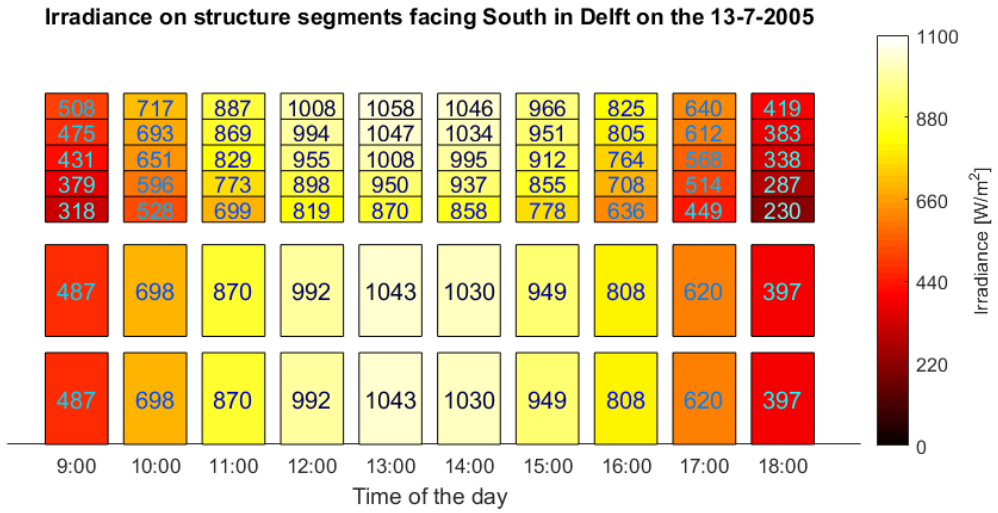

Figure 4.8: Irradiance on each segment of the kiosk with tracking and facing South on the 13th of July of 2005 in Delft

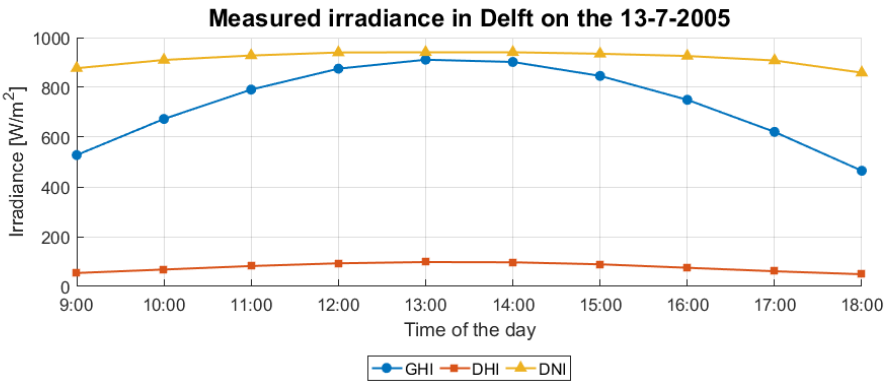

Figure 4.9: Irradiance measurements during the 13th of July of 2005 in Delft

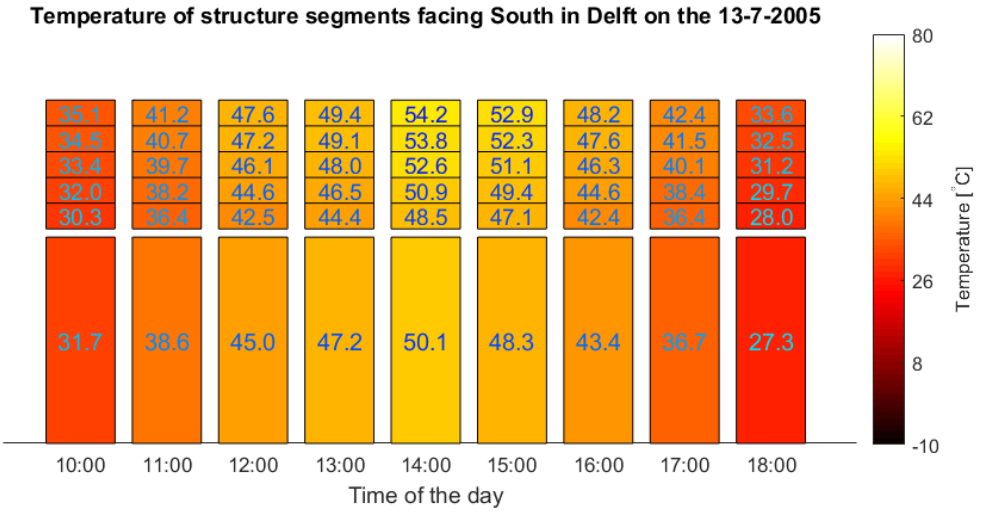

Figure 4.10: Temperature on each segment of the kiosk without tracking and facing South on the 13th of July of 2005 in Delft

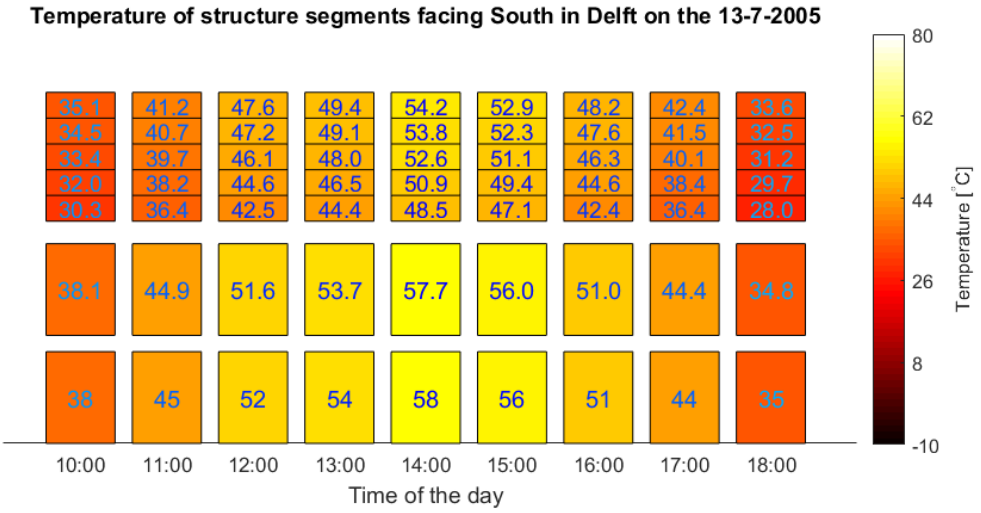

Figure 4.11: Irradiance on each segment of the kiosk with tracking and facing South on the 13th of July of 2005 in Delft

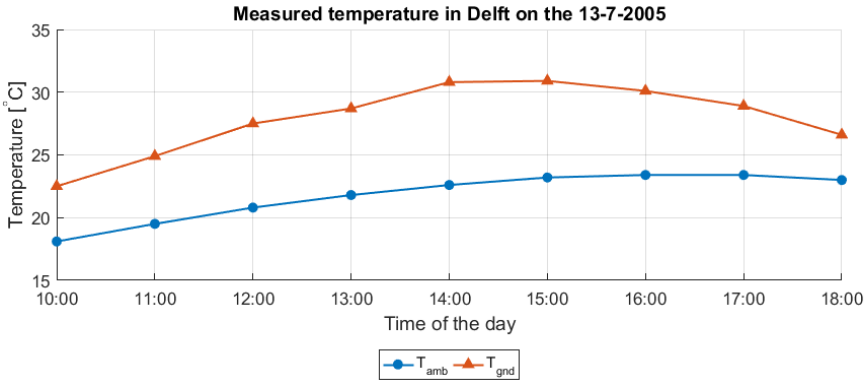

Figure 4.12: Temperature measurements during the 13th of July of 2005 in Delft

show the gain in using a tracking system.

Figure 4.13 shows a comparison of the energy yield of the 3 systems for two different cases: a completely free horizon (fhA0), and a constant skyline profile with an altitude of 65° (fhA6)[2].

In the case of a free horizon, it is clear that the use a tracking system yields better results when compared to the reference, especially when the modules are facing South, in which case 6% more energy can be harvested per year. However, when the modules are facing North the difference in yield is negligible. When other orientations are taken into account, in average, the tracking system generates 4% more energy. On the other hand, when the system with a tracker unit is compared to the kiosk with 24 cells, the static system always performs better. In average the passive kiosk generates 3% more energy than the active system, and in some cases, it can produce more than 7% extra energy.

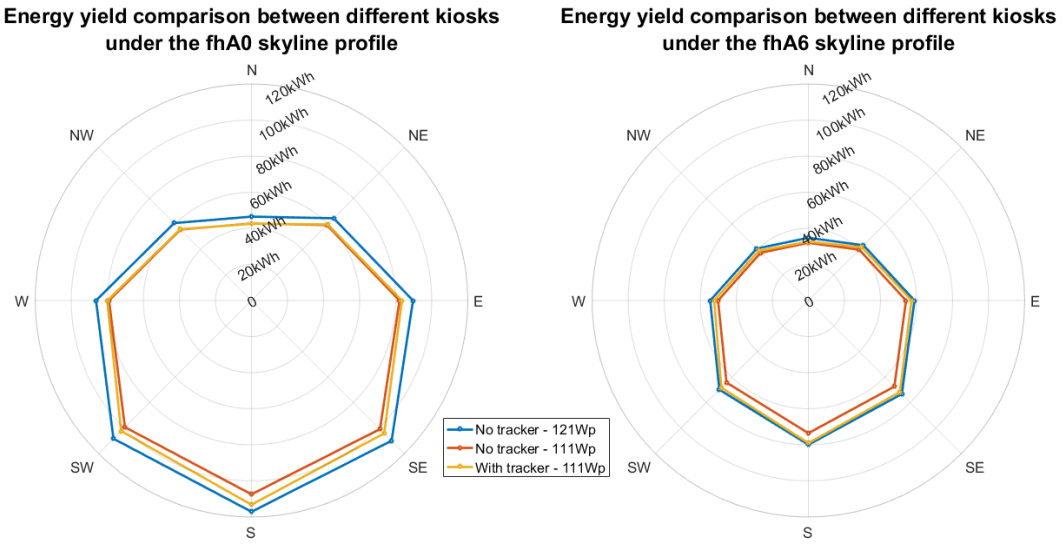

Figure 4.13: Comparison between the energy yield of the 3 versions of the kiosk for a free horizon and 8 different orientations. The red line shows the performance of the reference 22-cell fixed-tilt kiosk.

Under the fhA6 skyline profile, the energy yield of the three kiosks drops significantly, especially for the south direction, where the energy yield drops from around 110 kWh/year (with a free horizon) to less than 80 kWh. Even under this less favorable skyline profile, the static kiosk with a higher peak power always outperforms the kiosk with a tracking system.

These simulation results suggest that in the Netherlands it is more convenient to use a passive kiosk with a higher peak power rather than a kiosk with a tracking system (and a lower peak power). Based on these results it was decided that the prototype of the Infotainment Spot had to be static.

4.3. The effect of the skyline profile on the energy yield

As it is shown in Figure 4.13, the skyline profile has a significant influence on the energy yield of a PV system. The goal of this section is to find a simplified model capable of predicting how the energy yield is affected by the skyline profile characteristics in a specific location.

4.3.1. The Sun coverage factor

In this study, two parameters are used to characterize a skyline profile: the already introduced sky view factor (SVF), and the Sun Coverage Factor (SCF).

The sun coverage factor is a new parameter that has been introduced as part of this thesis project, and it is defined as:

$$SCF = \frac{Number\ of\ hours\ the\ Sun\ is\ blocked\ per\ year}{Number\ of\ Sun\ hours\ per\ year} \tag{4.1}$$

[2] Refer to Appendix E for a complete description of the synthetic skyline profiles.

For a location with a free horizon, SCF is null. For a location where the skyline profile or the tilt of the module block the Sun at every moment during the year, the SCF value is 1. It is worth mentioning that according to the definition in Equation 4.1, for an observer in the northern hemisphere, the SCF is more sensitive to obstacles placed on the south than to obstacles on the north. The sun coverage factor can be then used to complement the information given by the sky view factor.

The sky view factor contains information about the surroundings, the tilt, and orientation of the PV module. However, it gives no information about solar resources available in a geographic location: the same skyline profile could exist in two different locations, e.g., in Dubai and Amsterdam, and the SVF value would be the same. But it is evident that the energy yield of the panel should be larger in Dubai since the annual irradiation is much higher than in Amsterdam. It follows that the SVF by itself is insufficient to create a model to predict the effects on the energy yield.

In this regard, the sun coverage factor takes into account two additional effects. First, the azimuthal distribution of the skyline profile along the horizon line: the value of the sun coverage factor changes if a building placed on the North of the PV module or if the same building is placed to the South. Second, the solar resources available in a specific location in the globe: for the same skyline profile, the SCF is lower for locations at lower latitudes because the Sun reaches higher altitudes and there are also more sunlight hours per day.

4.3.2. Synthetic skyline profiles

In order to find out how these two factors relate to the annual energy yield, a series of synthetic skyline profiles have been created (refer to Appendix E). The synthetic skyline profile constitute an input data set for running the simulations. For the results presented below 80 different synthetic profiles have been used. Each of these profiles consists of a symmetrical set of rectangular shapes (that block the Sun) with different widths (azimuths) and heights (altitudes) as shown in Figure 4.14.

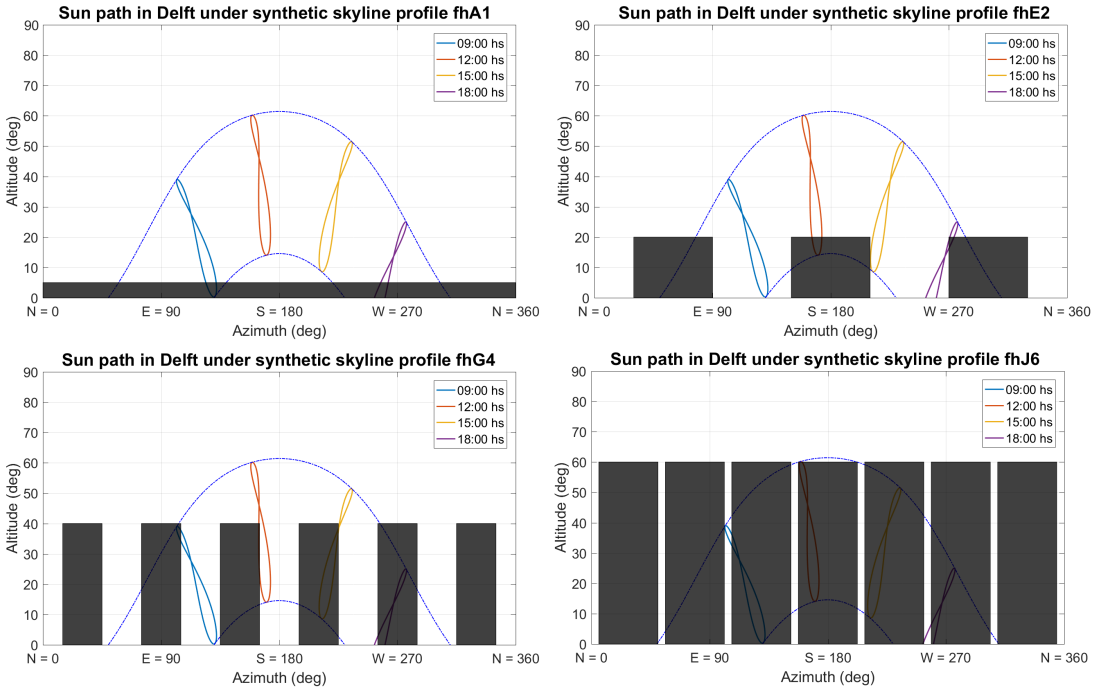

Figure 4.14: Examples of synthetic skyline profiles overlapped on top of the sun path in Delft

The idea behind the synthetic skyline profiles was to create a set of data that would allow studying the influence of the urban environments on the yield of a PV system. As it will be demonstrated in the following sections, this idea has proven to be very useful to find a relation between the SCF, the SVF, and the energy yield.

4.3.3. The energy yield estimation model

The irradiance on the kiosk was calculated for eight different orientations (N, NE, E, SE, S, SW, W, NW) using hourly meteorological data and applying the irradiance framework A presented in the previous chapter. The dependence of energy yield (resulting from the different sunlight components) on the SVF and SCF was analyzed using these simulations, and it was calculated as:

$$E_y = \int_{year} \left(\sum_i G_M^i(t) \cdot A_M \cdot \eta(t) \right) \cdot dt \tag{4.2}$$

where G_M^i stands for each of the five components of the light considered in framework A, and A_M is the active area of the PV module. Since the efficiency of the module (η) depends on the temperature and the total incident irradiance, Equation 4.2 can be rearranged in the following way:

$$E_y = \sum_i \left(\int_{year} G_M^i(t) \cdot A_M \cdot \eta(t) \cdot dt \right) \tag{4.3}$$

Equation 4.3 shows that it is possible to calculate the energy yield by adding the contributions of each of the sunlight components to the total energy yield. By decomposing the energy yield in this way, it was determined that there is a clear correlation between the SVF value and three different sunlight components: the diffuse isotropic component, the horizon brightening, and the albedo component. Nevertheless, the correlation between the sky view factor the direct beam and the circumsolar components is poor. These latter two components have shown a much stronger correlation with the SCF.

The contributions to the total energy yield can then be separated in two partial energy yields: the yield resulting from the direct beam radiation and the diffuse circumsolar component (E_y^1); and the yield resulting from the sum of the diffuse isotropic irradiance, the horizon brightening effect and the albedo component (E_y^2):

$$E_y = E_y^1 + E_y^2 \tag{4.4}$$

Figure 4.15 depicts the correlation between the partial energy yields and the SCF and the SVF for a specific location and module orientation. It is clear from the plots that E_y^1 shows a much stronger correlation with the SCF, while E_y^2 correlates better with the SVF.

It has been concluded that the correlation between the variables can be approximated by a quadratic function. A higher order approximation was discarded because the variance of the regression coefficients was too high. Furthermore, the more the module is oriented towards the south, the more linear the correlation between the variables.

In Figure 4.16 the error (ΔE_y) corresponding to the correlations shown in Figure 4.15 are presented. The error is defined so that $E_y \pm \Delta E_y$ contains at least 50% of the predictions of future observations of the independent variable. The lower deviations show that indeed the SCF correlates better with E_y^1 and the SVF with E_y^2.

Based on Equation 4.3, the proposed model for estimating the effect of the skyline profiles on the energy yield can be expressed as the sum of the quadratic regressions presented before:

$$\hat{E_y} = (a_2 \cdot SCF^2 + a_1 \cdot SCF + a_0) + (b_2 \cdot SVF^2 + b_1 \cdot SVF + b_0), \quad a_j,\ b_j \in \mathbb{R} \tag{4.5}$$

The constants a_j and b_j have been calculated for 8 module orientations, using meteorological data for 5 locations in the Dutch provinces of Holland and Utrecht[3] for 3 different years (2005, 2010 and 2015). All these locations present similar irradiance patterns, and therefore the model is applicable for a large geographic area and a long period. The average values of the constants for predicting the energy yield of the kiosk with and without a tracking system are given in Appendix F.

The calculated constants allowed to create the maps presented in Figure 4.17. These are a graphical representation of the prediction model for different orientations of the flat PV module on the kiosk. It can be noticed that according to the orientation the minimum SCF value changes. The maximum SVF for a module tilted 75° is 0.63, and the lowest SCF value that can be achieved occurs when the structure is facing south and it is 0.15.

[3] The cities used for the simulations include Delft, The Hague, Amsterdam, Rotterdam and Utrecht

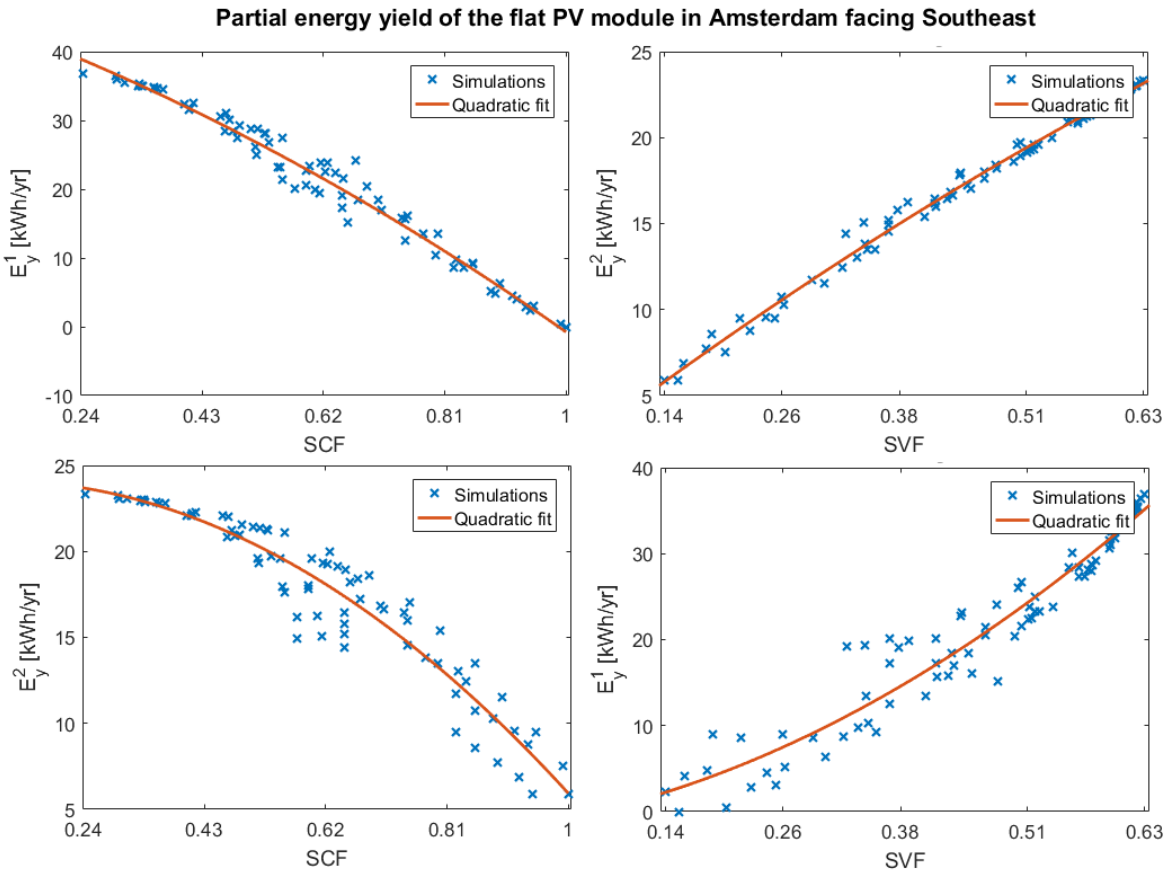

Figure 4.15: Correlation between the partial energy yields and the SVF and the SCF. The top plots show good correlations between E_y^1 and the SCF, and E_y^2 and the SVF. The bottom plots show the poor correlation if the variables are swapped.

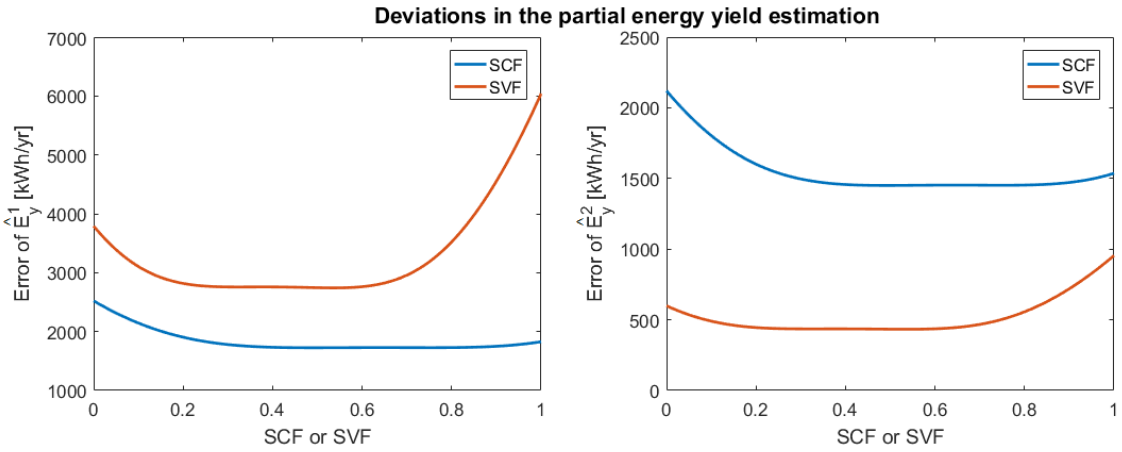

Figure 4.16: Deviations for each of the 4 correlations in Figure 4.15

A relevant property of the coefficients in Equation 4.5 is that they can be scaled with the peak power of a PV module. For example, the coefficients calculated for a PV panel of 100 W_p tilted 30° can be used to estimate the yield of a PV module of 200 W_p with the same tilt. The reason behind this property is that the area of the module in Equation 4.3 is a constant and it can be taken as common factor of the integral and the summation.

Furthermore, the model described by Equation 4.5 can also be applied to estimate the irradiation on a surface given the SVF and SCF values. Naturally, the constants a_j and b_j would be different because the

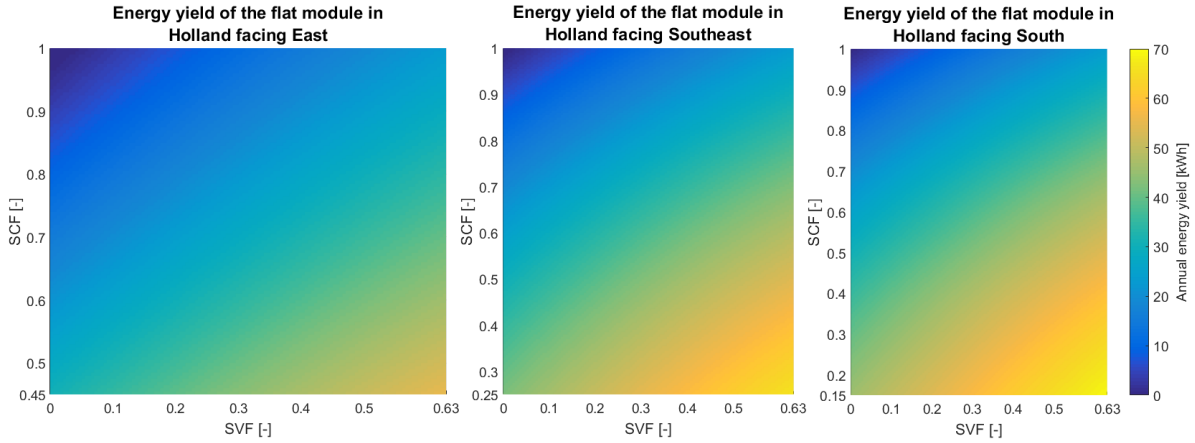

Figure 4.17: Energy yield of a flat PV module of 70.4 W_p tilted 75°

active area and the efficiency of the module are left aside.

4.4. Validation studies

To conclude this chapter, two main validation studies have been conducted to assess the reach and accuracy of the introduced models. The first study aims to validate the irradiance framework A by comparing the results with those obtained using the irradiance framework B. The object of the second validation is to quantify the deviations in the energy yield estimation proposed in subsection 4.3 using real skyline profiles.

4.4.1. Real skyline profiles

Multiple bus stops in Delft have been investigated to validate the prediction model based on the synthetic skyline profiles. The location of the 12 analyzed stops is shown on the map in Figure 4.18. In each of these places, the Horicatcher tool was used to capture the skyline profiles.

Figure 4.18: Location of the 12 analyzed bus stops

The Horicatcher tool consists of a calibrated camera and a reflective dome that allows capturing the shape of the skyline in a specific location. The pictures captured with the Horicatcher can be loaded in Meteonorm, where geometric parameters of the camera and the dome are used to process the image and project the skyline profile into an altitude-vs-azimuth map. The envelopes of the skyline profiles are obtained and processed

to generate the required data structure for the simulations. Figure 4.19 shows a picture of the Horicatcher dome taken at TU Mekelpark bus stop and the projection of the same skyline profile on the SVF grid introduced in Section 3.1.

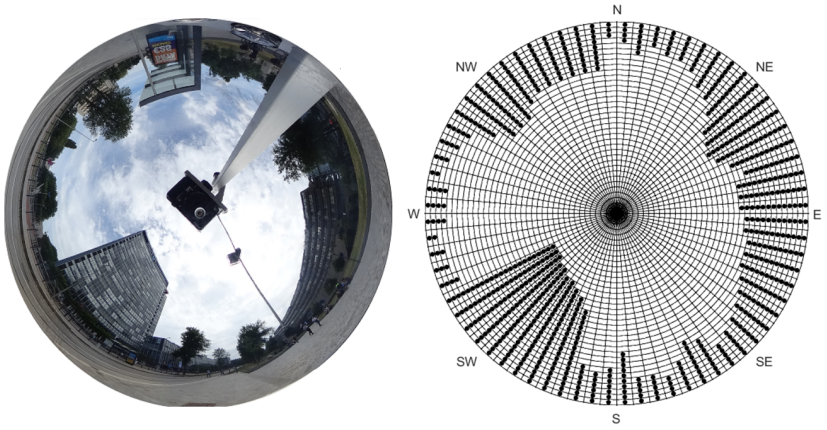

Figure 4.19: Skyline profile at TU Mekelpark bus stop (on 3/8/2017). Left: Image captured with the Horicatcher. Right: Projection of the skyline profile on the SVF grid

In Figure 4.20 the corresponding sun coverage factor values for each of the selected bus stops for a module placed flat on the ground are given. The values range from $SCF = 0.37$ (at Prinsenhof) to $SCF = 0.85$ (at TU sport en cultuur)[4].

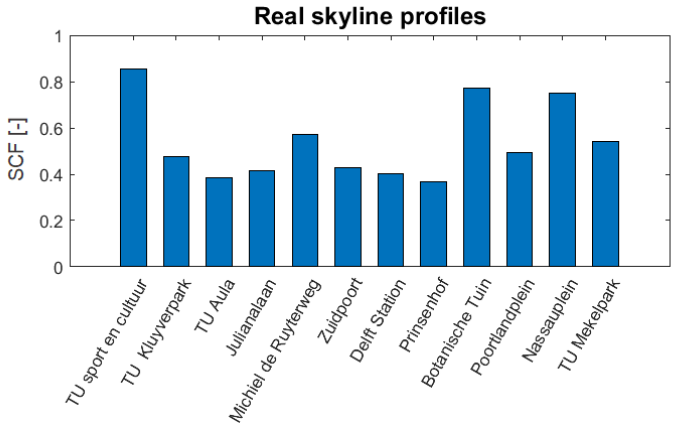

Figure 4.20: Sun coverage values for PV module placed horizontally in each of the 12 bus stops analyzed

4.4.2. Alternative methods for estimating SVF and SCF

The prediction model that describes the effects of the skyline profile on the energy yield can be useful only if there is also simple method to determine the SVF and the SCF. There are different methods to capture the skyline profile in a certain geographic position. The Horicatcher tool is one alternative. Nonetheless, this tool becomes impractical when a large number of locations must be studied, especially because it requires the user to go to the place of interest.

When moving to a particular location becomes inconvenient or even impossible, there are tools that allow using LiDAR data to create 3D maps. That is the case of the LAStools software suite, a collection of highly efficient tools that manipulate LiDAR data, which can be further processed to create maps like the one shown in Figure 4.21. For any point on this map, it is possible to reconstruct the skyline profile using the size and position of the polygons that constitute the surface of the 3D model.

For any region in the Netherlands, a point cloud generated with LiDAR data is available at the Actueel Hoogte Bestand Nederland website. This information makes it possible to recreate the skyline profile at any

[4]For the pictures of the Horicatcher tool in each bus stop refer to Appendix E

location in the country with high accuracy[5].

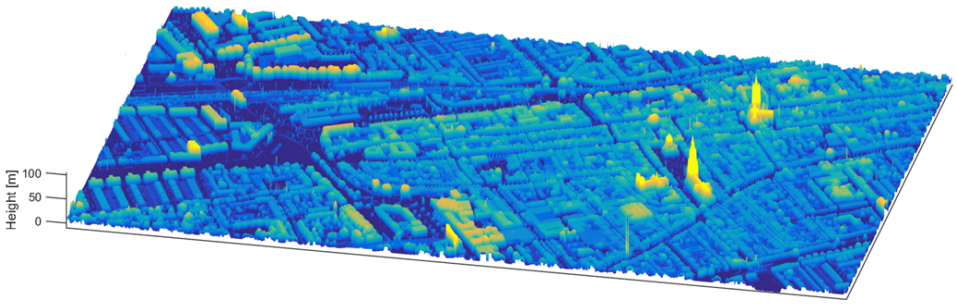

Figure 4.21: Elevation map of the city of Delft created using LAStools

LAStools is useful for evaluating the skyline profile in a large number of locations. However, when only a few number of locations are to be investigated remotely, LAStools is less convenient due to the time it takes to download and process the LiDAR data. As part of this project, a simplified tool named SkylineBlocks has been developed to reconstruct the skyline of a location remotely rapidly. SkylineBlocks allows to reconstruct the skyline profile by guiding the user through a simple sequence of steps:

1. Load a picture of the region of interest with the North direction pointing upwards.
2. Indicate the position and the height of the observer.
3. Indicate the dimension of the scale on the map.
4. Define the number of objects to be identified on the map.
5. Draw the polygons that define the shape of each building and input the height of each building.

The number of buildings needed to precisely define the shape of the skyline is usually lower than 10. Hence, most skyline profiles can be reconstructed very rapidly and accurately using SkylineBlocks. The heights of the buildings can be obtained from the online maps available on *www.ahn.nl* or from other sources (e.g. from Google Earth which extends the use of SkylineBlocks to places where LiDAR data is not available yet). Moreover, in contrast to LAStools, with this tool new obstacles that are not yet represented on the map can be included in the 3D model.

In Figure 4.22 the reconstruction of TU Delft campus using the simplified tool is shown. On the image on the left, the map and the polygons created by the user are presented. The observer position chosen by the user is indicated by a red dot. The image on the right shows the reconstructed 3D model. In this case, multiple buildings have been drawn for demonstration purposes, but only a few of them contribute to the skyline profile.

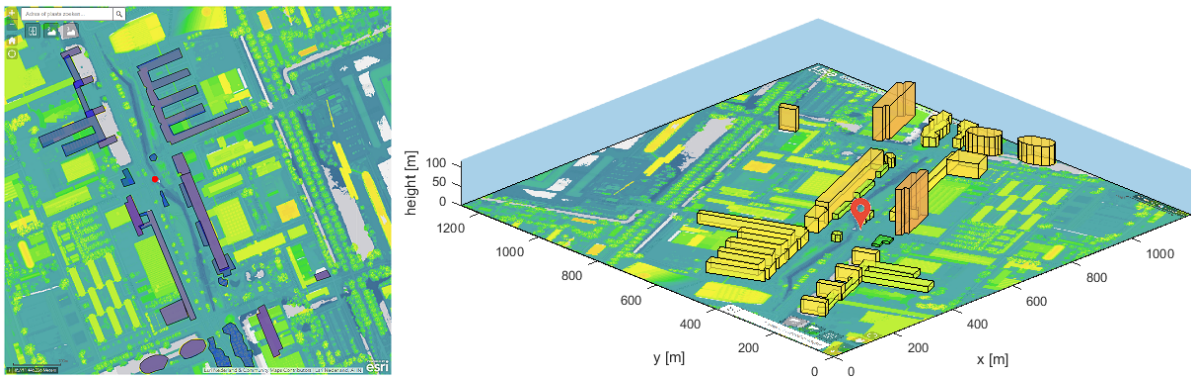

Figure 4.22: Simplified 3D model of TU Delft campus created using SkylineBlocks. The kiosk position is indicated with a red marker on the map.

[5]The accuracy of the point cloud is $\pm 1\ m$

Finally, in Figure 4.23 the resulting skyline profile is compared to the skyline profile obtained with the Horicatcher tool at the same location. The sun coverage factor values for the Horicatcher skyline and the approximated skyline are 0.54 and 0.49 respectively. The performance of the kiosk with both skylines has also been simulated, and results differ in less than 3% for all eight orientations of the structure.

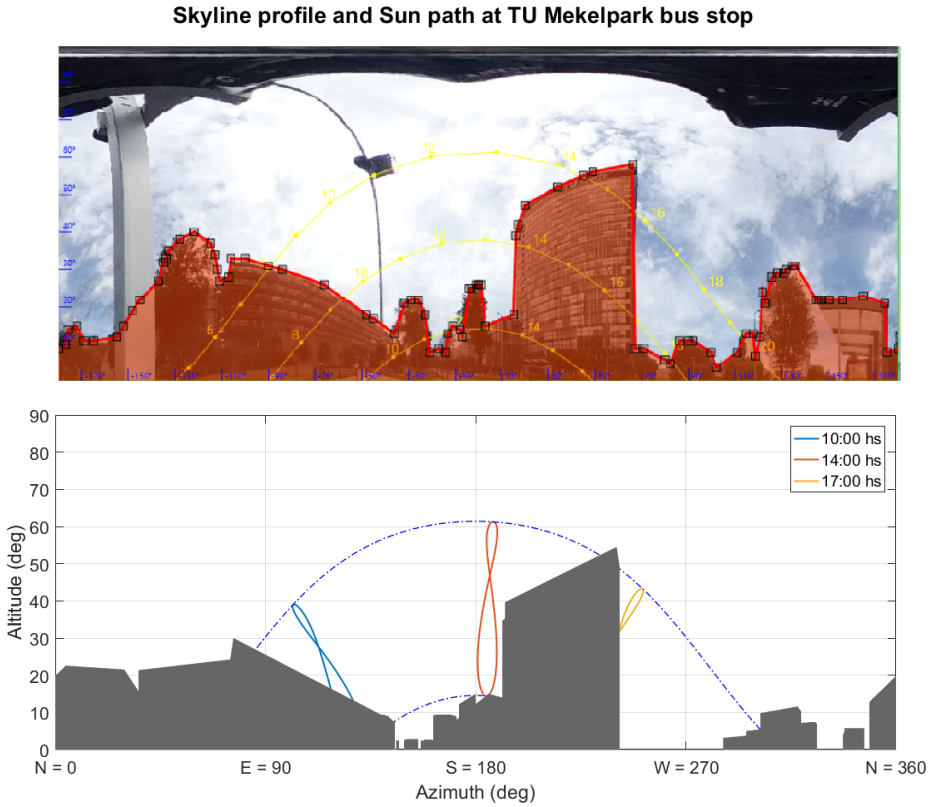

Figure 4.23: Comparison between the skyline profile captured with the Horicatcher tool (top) and the one obtained with the developed script (bottom)

The main disadvantage of SkylineBlocks is that buildings are approximated with prismatic bodies and the tool is not very suitable for buildings with tilted roofs. Moreover, the user might disregard objects on the map that are important for the skyline profile, obtaining results that are not representative of the location of interest.

In this project, the SkylineBlocks tool was used to study the shape of the skyline profiles in different cities in the Netherlands.

4.4.3. Application of the irradiance framework B

In order apply the irradiance framework B a 3D model of the kiosk is needed. In this case, a STEP model of the kiosk was created using Solidworks and was later imported in Lightools, where each surface was assigned optical properties. Additionally to the kiosk, different blocks were modeled to recreate the skyline profile. The optical properties were assigned as indicated below:

- Solar cells: 100% absorptivity.
- Floor: Lambertian scatterer: 15% reflectivity (albedo coefficient).
- Kiosk metallic structure: Lambertian scatterer: 80% reflectivity.
- Buildings: Lambertian scatterer: 10% to 60% reflectivity.

Figure 4.24 shows the kiosk model created for LightTools and the reconstruction of the synthetic skyline profile fhH4. The skyline profile fhH4 consists of 4 blocks with an altitude of 40° and a width of 60° centered at four different azimuth values: 67.5°, 142.5°, 217.5° and 292.5°. The selection of this skyline profile was

arbitrary, and although the results are not presented in this report, simulations carried out with other skyline profiles led to the same conclusions.

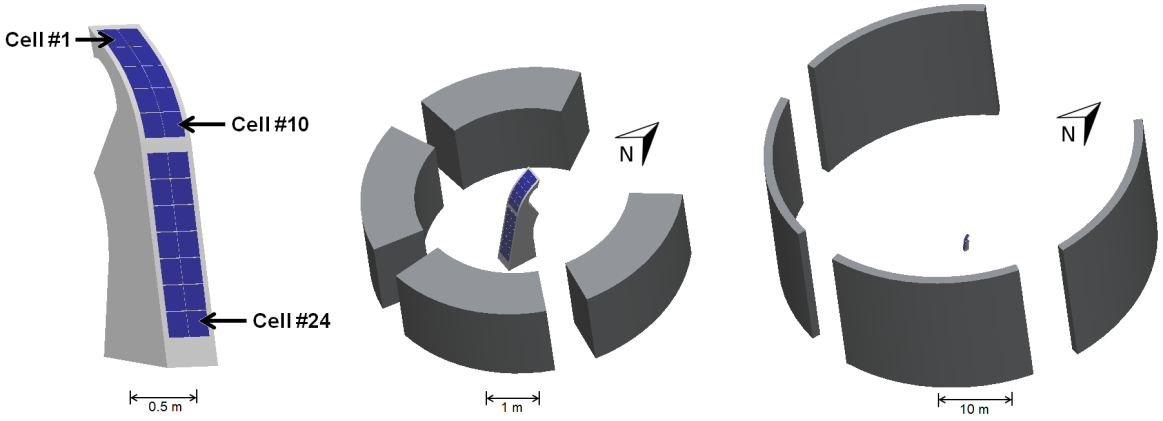

Figure 4.24: LightTools model. Left: Detail of the kiosk model. Center: Skyline profile fhH4 at 2 meters. Right: Skyline profile fhH4 at 20 meters.

For creating the sky map a light source[6] was moved around the celestial sphere in steps of 5 degrees. In total, the sensitivity of every solar cell on the kiosk was calculated for 1296 different positions of the light source. The sensitivity map was later interpolated to obtain a resolution of 0.5°.

In Figure 4.25 the sensitivity maps of the top and bottom cells of the kiosk are shown. The diffuse borders of the obstacles on the sky maps are a consequence of the interpolation. Ideally, the edges of the obstacles should be sharp, and the sensitivity should be null at those points below the skyline.

In fact, it has been verified that the sensitivity map for the skyline profile fhH4 can be accurately reconstructed by starting from the free horizon sensitivity map and later making zero the sensitivity for all points lying below the skyline. Figure 4.26 shows the absolute value of the difference between the simulated and the reconstructed sensitivity maps for cell 24. The differences are found along the edges of the obstacles due to the coarse discretization of the skydome in the simulations. The negligible (almost null) difference between both maps in the inner part of the obstacles that shape the skyline profile confirms the expectations. As the differences are exclusively concentrated along the borders, it follows that the maps generated starting from the free horizon sensitivity map are more accurate than the results from the skyline profile simulation.

A sky map for every hour during an entire year has been created using meteorological data for the city of Delft. The luminance of the sky was calculated with a resolution of 0.5° to match the sensitivity maps previously described. In Figure 4.27 the sky map at a specific instant during the year is shown.

By multiplying the sky and sensitivity maps, the irradiance on cells was calculated for each hour during an entire year and the results were compared with the results of the irradiance framework A.

4.4.4. Effect of the reflectivity and distance between objects

Since the synthetic skyline profiles only indicate the altitude and azimuth of the skyline, the distance of each of the obstacle blocks to the kiosk remains undefined. The spacing between the kiosk and the objects that constitute the skyline profile can have an important impact on the yield: if the surfaces of the obstacles are highly reflective and are too close to the kiosk, the reflection of light on the surfaces could in principle enhance the sensitivity of some cells.

Figure 4.28 shows the results of multiple simulations that were carried out by changing the reflectivity value of the obstacles and the distance between these and the kiosk for the skyline profile fhH4. From these simulations, it was inferred that:

- When the obstacles are too close to the structure, their dimension is comparable to that of the kiosk, and the skyline profiles for different cells on the kiosk differ significantly. For example, for obstacles at 1m of the structure the obstacle's height it 84 cm and all the cells that are above this height are not shaded at all[7]. For this reason, only the irradiance on cell #24 has been considered in the comparison.

[6] The properties of the light source were defined according to the guidelines established in [18].
[7] Refer to Appendix G for a complete geometrical description of the problem.

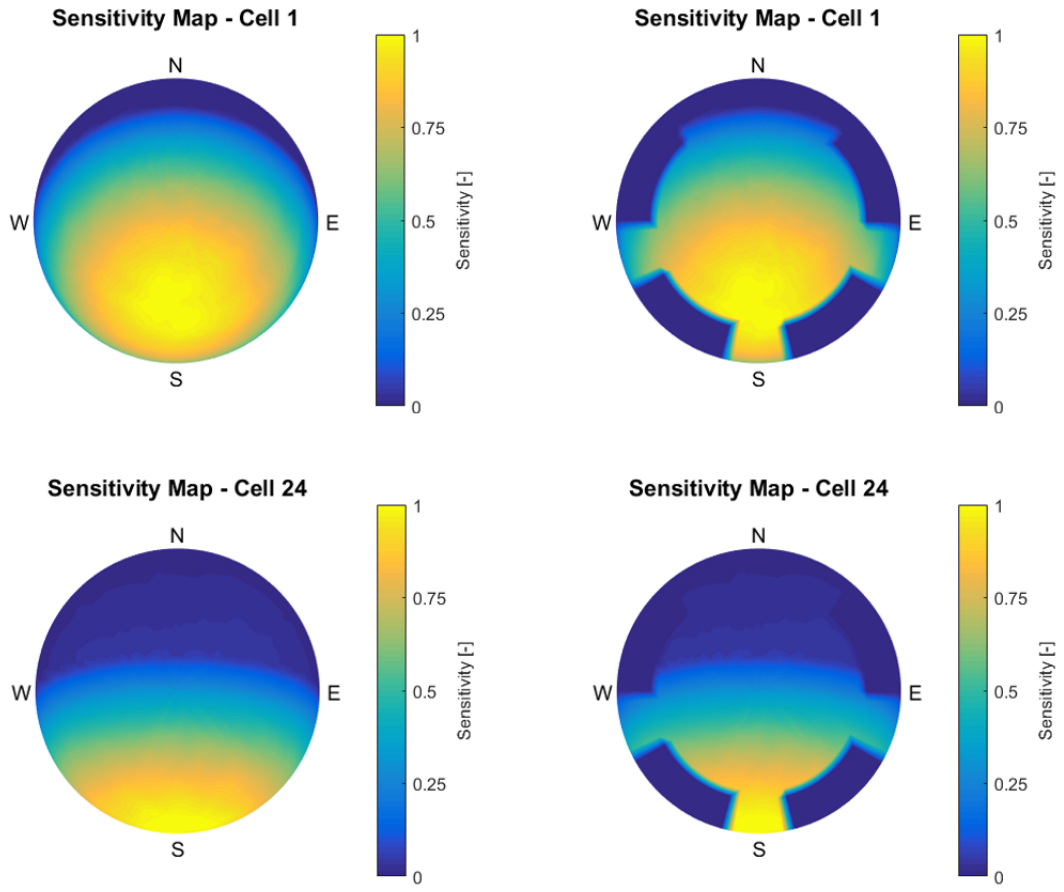

Figure 4.25: Sensitivity maps for different cells. Left: Under a free horizon. Right: Under skyline profile fhH4.

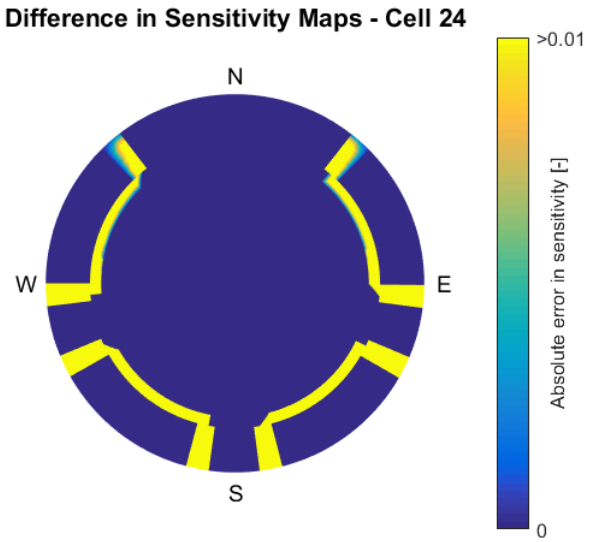

Figure 4.26: Difference between the sensitivity map for skyline fhH4 obtained from LT simulations(with the obstacles at 10 m from the kiosk) and the one generated by modifying the free horizon sensitivity map.

- Highly reflective obstacles enhance the sensitivity of the cell when they are closer than 3 m from the structure.

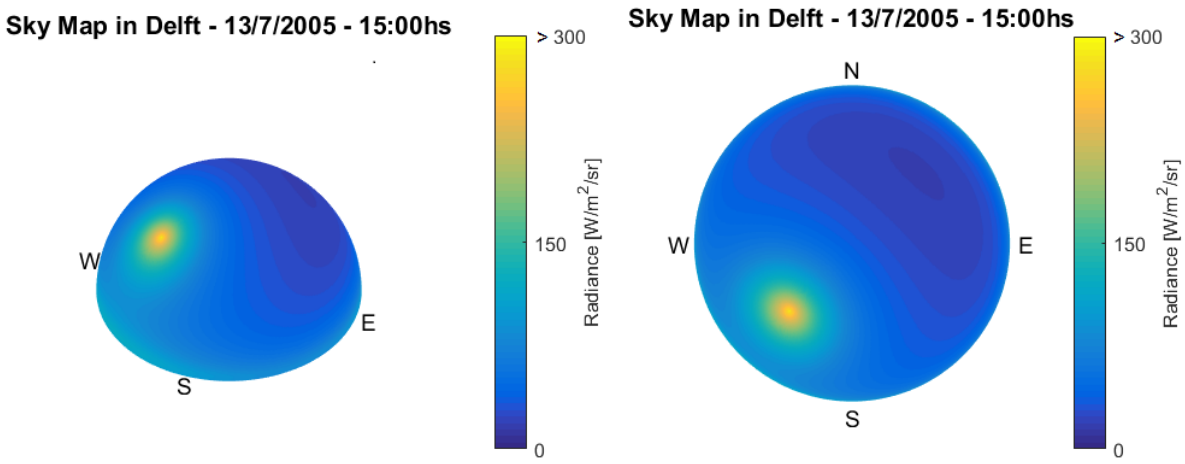

Figure 4.27: Sky map in Delft on July the 13th of 2005

- For objects further than 3 m away from the structure the irradiation changes in less than 3%.
- For objects further than 5 m away from the structure the effect of the reflectivity index of the obstacles on the annual irradiation is lower than 1%.

Most of the objects around a kiosk in real locations are enough separated from the structure to assume that their distance to the kiosk and their optical characteristics have a negligible impact on the sensitivity of the solar cells.

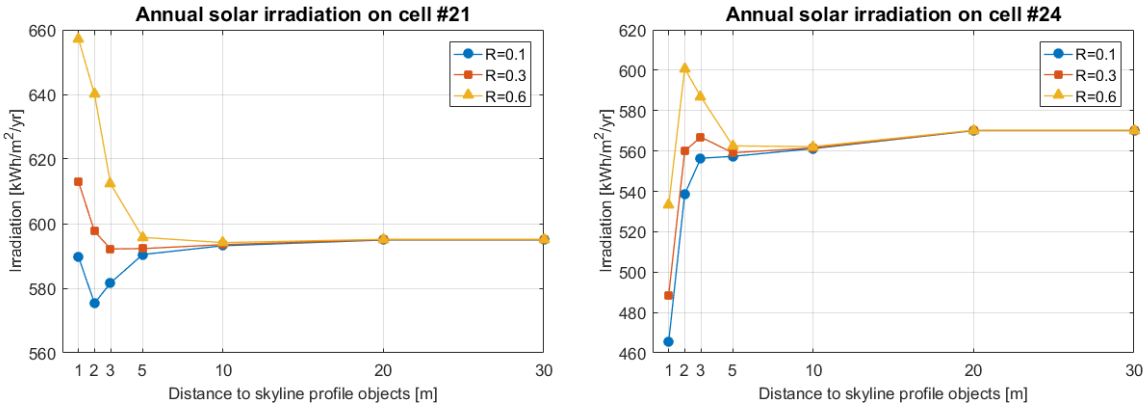

Figure 4.28: Dependence of the solar irradiation on the distance to the skyline profile objects and their reflectivity index

4.4.5. Validation of the skyline profile effects

Following the reflectivity study, the radiation on the kiosk without a tracking system was compared using both irradiance models.

In the comparison established here, the performance of the kiosk is assessed by calculating the radiant energy incident on the surface of the modules. The conversion efficiency from light to electricity is not taken into account to study the performance of the irradiance frameworks independently from the thermal and electrical models.

Furthermore, as the goal of this section is to compare the methods for calculating the irradiance and not the actual yield of the kiosk, the cumulative radiant energy on the module was calculated as the sum of the irradiance values on each of the cells. Even so, it must be reminded that since the modules do not have individual bypass diodes across each cell, and the cells are connected in series, the actual PV power generated by the modules is limited by the cell receiving the lowest irradiance.

To determine the deviations between frameworks A and B, sixteen cases have been analyzed[8]. The cases

[8]For each of these simulations meteorological data for Delft for the year 2010 was used.

involved two different skyline profiles and eight different module orientations.

The radiant energy received by each module[9] of the kiosk during an entire year when the horizon is free is shown in Figure 4.29. Likewise, Figure 4.30 shows the results of the simulations when considering the synthetic skyline profile fhH4.

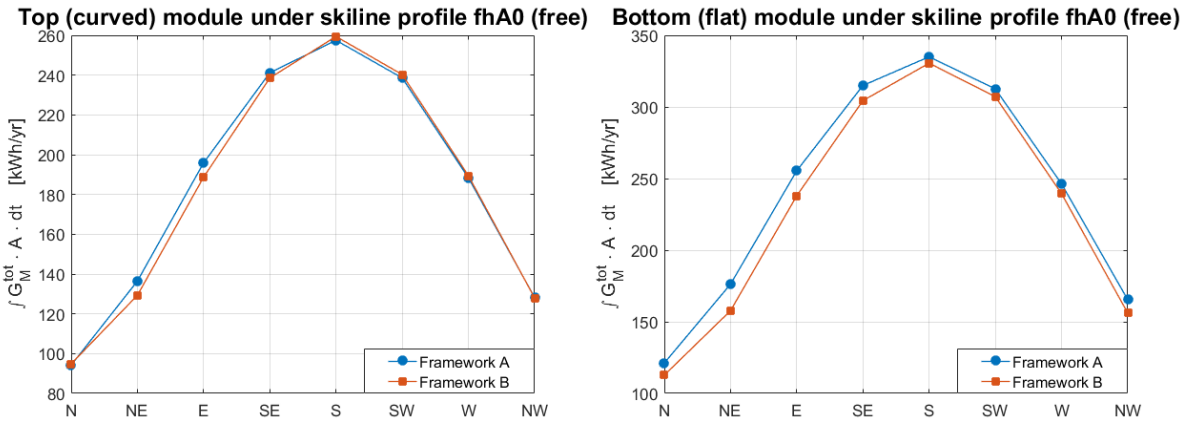

Figure 4.29: Simulated radiant energy received by the modules with a free horizon during an entire year.

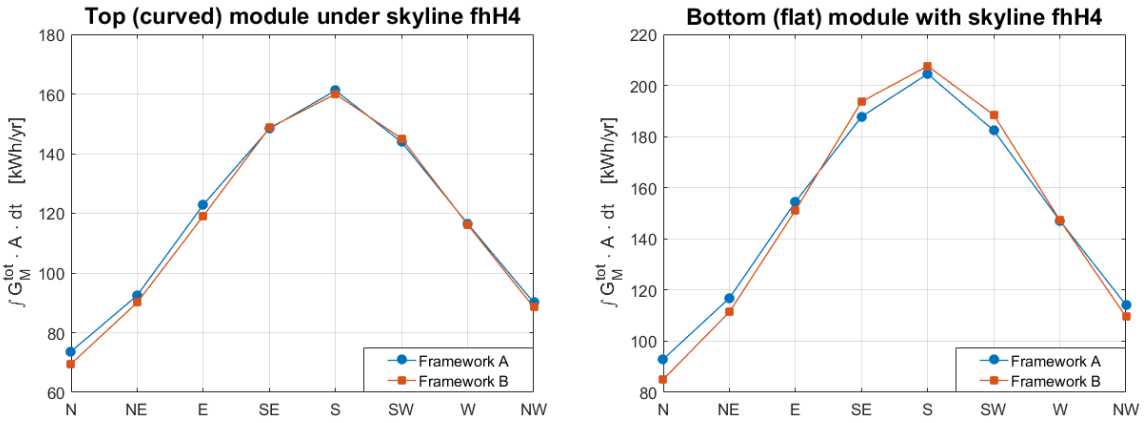

Figure 4.30: Simulated radiant energy received by the modules with the fhH4 skyline profile during an entire year.

From the free horizon simulations, it is possible to see that framework A slightly overestimates the energy received by the flat PV module. The maximum relative deviation (10%) occurs when the flat module when is pointing to the northeast. On the other hand, relative deviations in the case of the curved module under a free horizon are always lower than 6%.

Regarding the simulations with the skyline profile fhH4, in some cases framework A yields lower results than framework B. The maximum relative deviation was obtained in the case of the flat module when pointing to the north (7.7%).

Since the results in Figure 4.29 and 4.30 always show smaller deviations for the curved module, it could be concluded that framework A is more accurate for PV modules that are more separated from the ground level. In fact, the simulation results from Figure 4.31 show that, when applying framework B, the lower cells of the flat module (those closer to the floor) are the ones that receive the highest irradiance as a consequence of light reflected on the ground. Meanwhile, the top cells of the flat module receive an irradiance about 5% lower.

From Figure 4.31 it can also be noticed that the average irradiance on the flat module calculated using framework B is always lower than the one obtained using framework A.

The differences mentioned above are predictable because framework A does not take into account the distance from the ground to the PV module. The presented results indicate that framework A could be further

[9]The area considered for calculating the total energy received is the active area of the module.

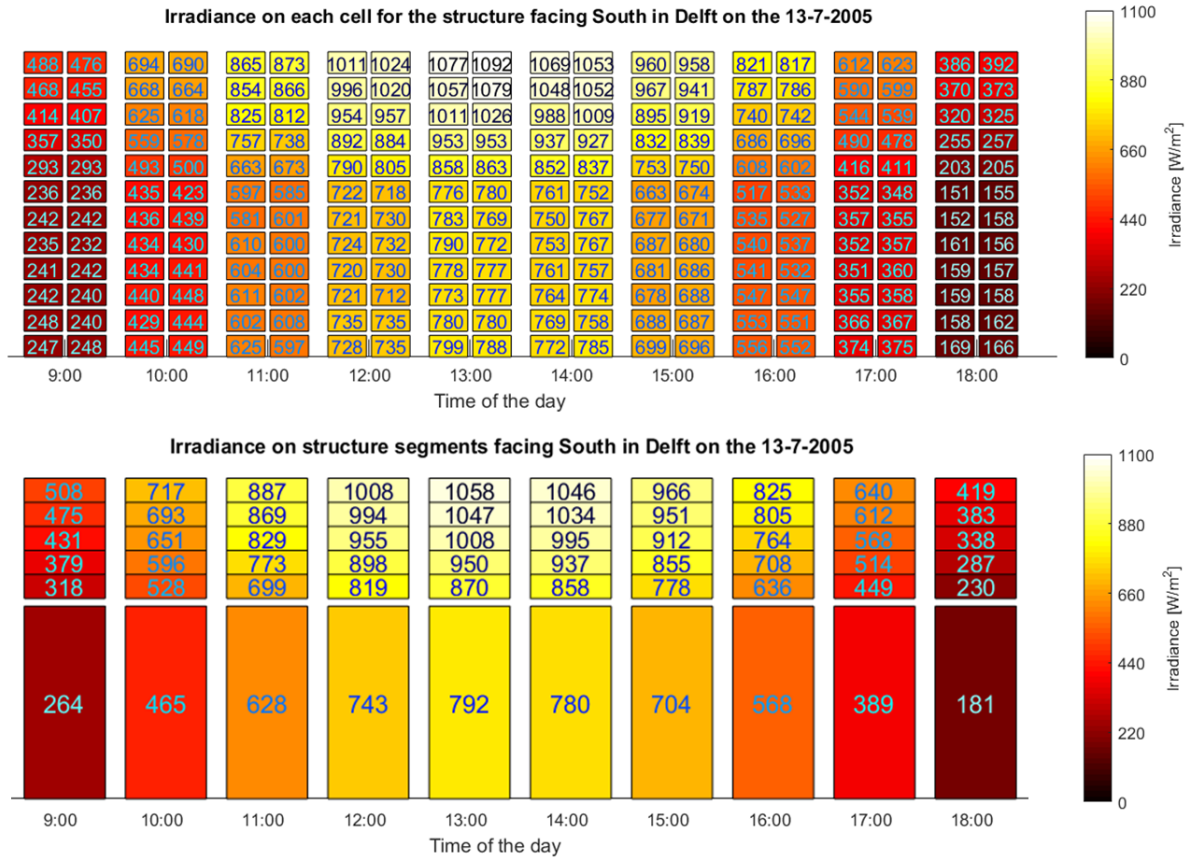

Figure 4.31: Comparison between the power incident on the kiosk calculated using both irradiance frameworks for a free horizon on the 13th of July

improved by modifying the calculation of the albedo component ($G_M^{dif-gnd}$). Nonetheless, the accuracy of this framework is considered to be good enough to the end of this study.

4.4.6. Validation of the energy yield prediction model using real skyline profiles

The final validation step consisted in comparing the energy yield of real skyline profiles resulting from the application of framework A with the results of the prediction model based on synthetic skyline profiles.

The performance of the kiosk was evaluated for the 12 bus stops presented before. In each of the locations, the structure was rotated eight times. For each of these 96 cases, the SCF and the SVF have been calculated, and Equation 4.5 was used to estimate the energy yield. The deviations between the estimation and the result of the simulation were determined according to the following formula:

$$\Delta_r = \frac{E_y - \hat{E}_y}{E_y} \tag{4.6}$$

According to Equation 4.6, positive deviations mean that the estimation is lower than the simulated yield.

The deviations in the prediction of the energy yield for the kiosk with and without tracker in Delft are shown in Figures 4.33 and 4.32 respectively. The deviations have been calculated from 2006 to 2016. The corresponding annual irradiation is provided on the left for reference.

Between the years 2007 and 2013 almost all the deviations are within an interval of ±10%. However, for the year 2006 and between 20014 and 2016, the entire deviations shift to the right, which implies an underestimation of the energy yield.

In order to understand the magnitude of the deviations and the right-shift for certain years, it must be recalled that the estimation coefficients for the kiosk were calculated using meteorological data for three different years and five different locations. Consequently, the coefficients reflect the average energy yield in Holland and Utrecht. On the other hand, the annual irradiation plots show variations of up to 15% (e.g. when

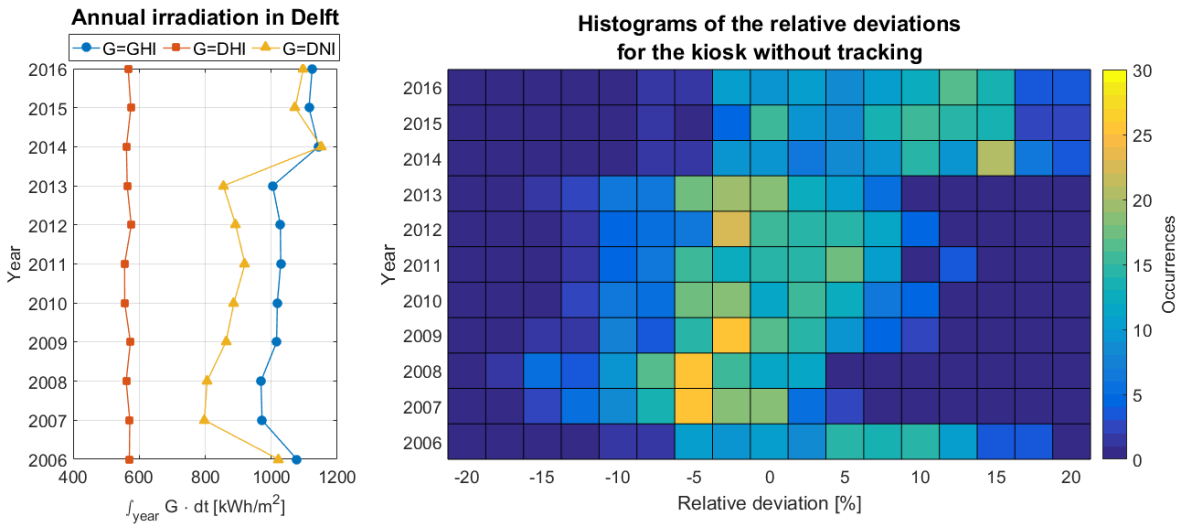

Figure 4.32: Annual irradiation and deviations in the energy yield estimation for a kiosk without tracker in 12 bus stops in Delft

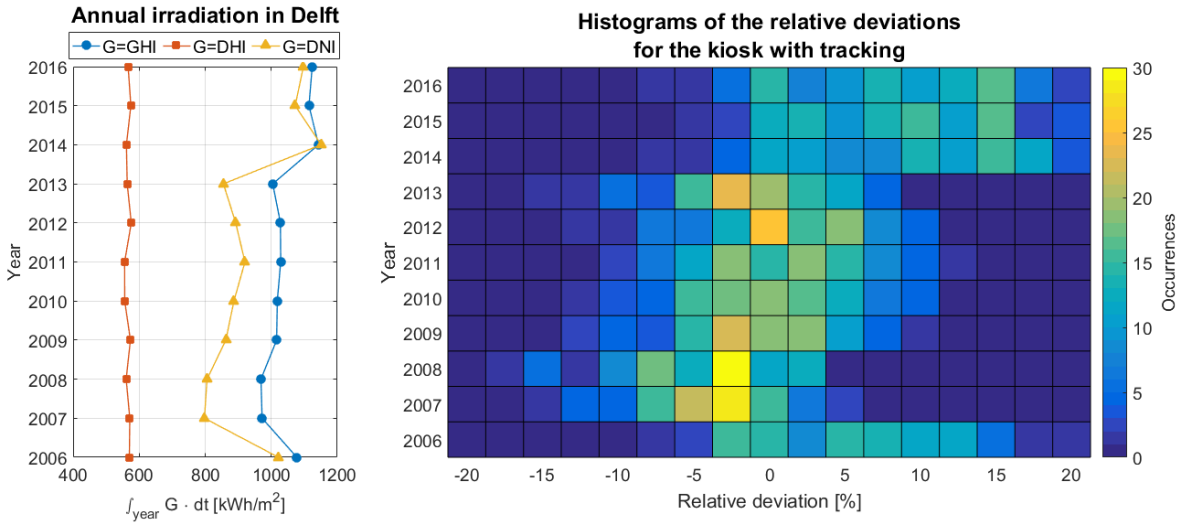

Figure 4.33: Annual irradiation and deviations in the energy yield estimation for a kiosk with tracker in 12 bus stops in Delft.

comparing 2013 and 2014). The higher irradiation leads to higher simulated energy yields. From the plots, it is evident that the years when the irradiation is above average correspond to those years when deviations are shifted to the right.

4.5. Summary

In this chapter, the new designs of the Infotainment Spot have been introduced. The performance of the kiosks has been compared with each other, and it has been concluded, that it is more convenient to implement a static kiosk. Furthermore, a new parameter called the Sun Coverage Factor has been introduced, and a model based on synthetic skyline profiles has been proposed to predict the energy yield of a PV system.

Chapter 4 has served to address the first two research questions. The answers are summarized below.

What is the effect of implementing a tracking system on the Infotainment Spot?

(a) *How can a tracking system be optimized?*
A horizontal axis tracking system has been designed. This tracking system allows tracking the sun along the year. The tilt angles that maximize the energy yield for all possible orientations have been calculated. Furthermore, in subsection 4.1.3, it was shown that a discrete tracking system is a much better alterna-

tive than a continuous tracking system since the loss in harvested energy is negligible while the gain in simplicity and reliability is very significant.

(b) *What is the gain in the harvested energy by using a tracking system when compared to a fixed tilt system?*
When two kiosks with the same peak power (110.7 W_p) are compared, the system with a tracker can generate 4% more energy in average. However, if all available space on the back of the kiosk is exploited, two more cells can be fitted if a static module is used, and the fix tilt kiosk with a higher peak power (120.7 W_p) performs 3% better in average than the kiosk with a tracking system.

Can the characteristics of a skyline profile be quantified to create a simplified model for estimating the energy yield of a PV system?

(a) *What are the relevant parameters?*
The two relevant parameters for characterizing a skyline profile are the sky view factor (SVF) and the sun coverage factor (SCF).

The sky view factor makes it possible to calculate the energy yield resulting from the diffuse isotropic, the horizon brightening and the ground reflected radiation components.

The sun coverage factor has been introduced as part of this study, and it was defined as the ratio between the number of hours the sun is covered by the skyline profile and the total number of hours the sun is above the horizon. This factor allows estimating the energy yield resulting from the direct beam and the diffuse circumsolar radiation components.

(b) *What is the reach and the limitations of the model?*
The coefficients of the model have been calculated for five different cities using meteorological data from years 2005, 2010 and 2015. Hence, the model applies to any location in Utrecht, North and South Holland.

The model can be scaled to predict the energy yield of a system with a larger peak power and the same tilt angle.

The proposed model has two main limitations. First, the objects that constitute the skyline profile must be at least 3 m away from the PV system to ensure that the reflected light on these surfaces is negligible. Second, the accuracy of the model improves the more distant the solar modules are from the ground. When the module is too close to the ground, the ground-reflected light causes the total irradiance to vary about 5% along the module.

(c) *What is the accuracy of the estimation?*
The accuracy of the model is about $\pm$10% for those years with average irradiation levels. However, when the annual irradiation is increased in 15% the deviations in the prediction can raise up to 20%.

5

Balance of system

In this chapter, the selected components for building the prototype of the Infotainment Spot and design of the BoS are introduced.

First, the load profiles are defined by measuring the power consumption of the loads. In the second place, the minimum storage capacity is calculated. Finally, the fabricated prototype and the assembly including all the components are presented.

5.1. Load characterization

This section describes the system's loads and the power electronic components of the Infotainment Spot.

5.1.1. Tablet

There are two main alternatives for the human interface device (HID) for the kiosk. One option is a tablet; another alternative is a touch screen connected to a computer. Although from the user perspective there is no major difference in the functionality, each option has advantages and disadvantages for the design.

Regarding the tablet, the main advantage is the low energy consumption: a tablet consumes one half of the power of a touchscreen of the same size for outdoors applications. Also if a tablet is chosen, no integration between the computer and the screen is required. Moreover, commercially available tablets can offer IP67 protection from all sides, while touch screens provide this protection level only on the front side.

The main disadvantages of a tablet are the elevated cost and the limited number alternatives in the market. For example, the largest screen size for an off-the-shelf rugged tablet is 10.1 inches. Moreover, if a performance monitoring system is to be implemented, it is much easier to integrate different types of sensors and actuators with a single board computer.

For this project, the main constraint is the power consumption, hence the tablet Toughpad FZ-A2 from Panasonic has been chosen. This tablet is equipped with a 16 Wh Li-ion battery which constitutes an extra energy buffer that can allow the system to operate for around two additional days.

The Toughpad FZ-A2 runs Android 6.0, allows the creation of a WiFi hotspot, and offers a maximum screen brightness of 800 cd/m^2, which ensures that the display is readable even during the brightest hours of the day.

The power consumption of the tablet was measured under different operating conditions is summarized in Table 5.1.

Table 5.1: Panasonic FZ-A2 average power consumption

Brigthness [%]	Apps	Wi-Fi	4G	Power [W]
0	CLOSED	OFF	OFF	0.5
0	OPENED	ON	ON	1.3
50	CLOSED	ON	ON	4.3
100	CLOSED	ON	ON	5.6
100	OPENED	ON	ON	6.5 to 10.6

5.1.2. Illumination

The kiosk is illuminated with the dimmable LED lamp. The LED maximum power is 1 W and it can be dimmed using the circuit presented in Figure 5.1 on the left. This small converter allows to power the LED with an AC or DC voltage source, and a buck converter (implemented in the IC PT4115) by means of a feedback loop allows to control the power of the LED. The value of the resistor R_s determines the maximum mean current through the LED, and PWM signal or a DC voltage level on the DIM port are used to regulate the LED power.

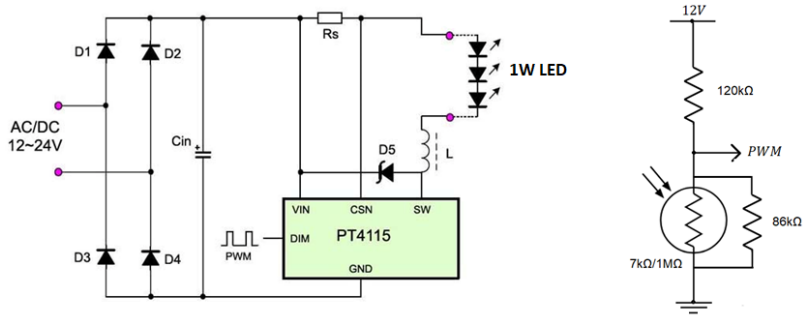

Figure 5.1: LED dimmer circuit

A voltage divider with a light-dependent resistor (LDR) has been connected to the PWM terminal to adapt the LED power to the ambient light intensity. During sunrise and sunset, the luminance is between 1 to 10 lux. The resistance of the LDR depends logarithmically on the light intensity: at 1 lux the resistance is around 40 $k\Omega$ and at 10 lux it drops to 7 $k\Omega$. The voltage threshold of the PT4115 to turn on the LED is 0.7 V.

As indicated on the right diagram in Figure 5.1, a resistor of 120 $k\Omega$ was connected in series to the LDR to create the voltage divider, and a second resistor was connected in parallel to the LDR to prevent exceeding the maximum allowable voltage by the IC (5 V in the PWM port) . With this configuration the LED turns on when the resistance of the LDR raises above 8.1 $k\Omega$, that is when the luminance is lower than 8 lux.

5.1.3. Phone charger

The kiosk can also be used as a charging station for mobile phones. A waterproof USB charger has been connected to the kiosk to offer this functionality. The charger has two different outputs: one that can deliver up to 1 A, and a second one capable of delivering up to 2.1 A. The efficiency of this USB charger has been measured, and it varies between 90% and 95%.

5.1.4. Load profiles

The time each is active was determined following the criteria presented below:

- The LED lamp consumes 0.5 W, and the number of daily hours it is switched on depends on the season. During the summer it was assumed that the LED is on between 10 PM and 6 AM. During winter the LED is on between 6 PM and 8 AM. Finally, during the equinoxes the LED turns on at 8 PM and turns off at 7 AM.
- The tablet is used in average 15 times a day, each time during 5 minutes. While the screen is turned off the power consumption is 1.3 W, and while it is being used the average power consumption is 9 W.
- The phone charger is used 45 minutes a day at maximum power (5 W)

Adding up all the contributions a the load profile can be calculated. An example of a load profile for summer and winter are shown in Figure 5.2. The daily energy demand is approximately 50 Wh (it depends on the season) and annual energy consumption of the kiosk is 18.2 kWh.

5.2. Energy storage

Once the load profile and the PV generated power are known, the storage capacity can be calculated. For the energy storage system, two main types of batteries have been considered: VRLA and Li-ion. The main characteristics of each technology are described below.

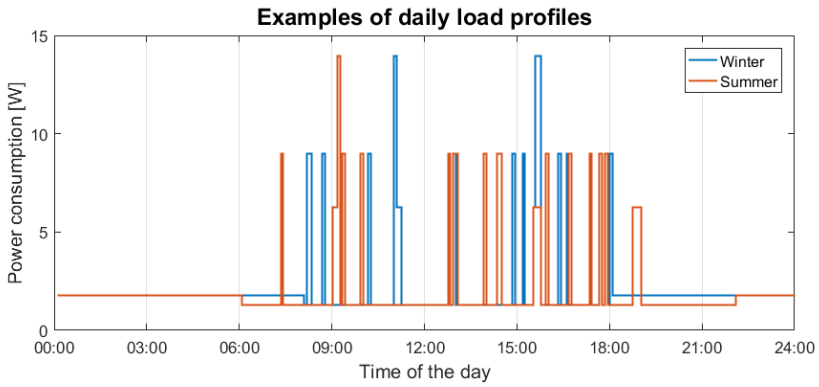

Figure 5.2: Load profile examples

5.2.1. VRLA batteries

Valve regulated lead-acid (VRLA) batteries are sealed Pb-acid batteries. In Pb-acid batteries, the electrodes are separated by aqueous sulphuric acid (electrolyte) which enables the transport of ions between the cathode and the anode. The basic charging and discharging reactions are depicted in Figure 5.3: during the charging process lead is oxidized at the anode and reduced at the cathode; during the discharging process the reactions are reverted. The standard potential of the cell is $2.04V$

However, there are side reactions that have important consequences on the performance of Pb-acid batteries. One of the main issues is the gas generation from the water in the electrolyte. Especially when the battery is overcharged, water is oxidized at the anode producing O_2 and protons that travel through the electrolyte to the cathode where they are reduced and form H_2 [14]. The gassing process is the reason why flooded lead-acid batteries require the regular addition of water.

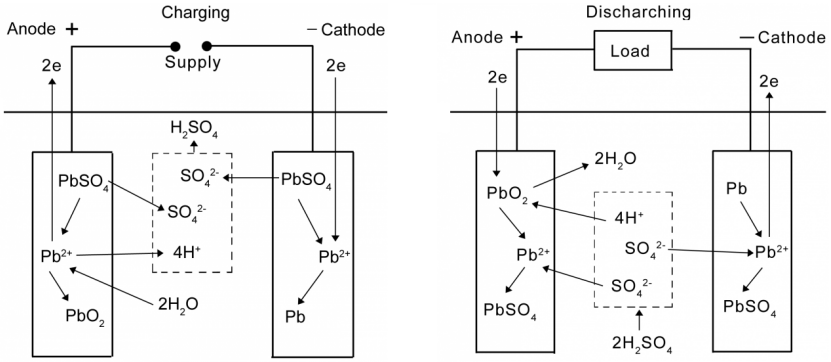

Figure 5.3: Pb-acid battery main reactions

In VRLA batteries the O_2 produced on the positive electrode is transported to the negative electrode where it is reduced, and therefore the effects of gassing and water loss are significantly mitigated[1]. Nevertheless, if the production rate of O_2 is larger than its reduction rate, the pressure inside the battery starts to rise (since it is sealed) and a pressure-release valve is required to allow the evacuation of the gases.

Gas pores are built within the electrolyte to allow the transport of the generated oxygen to the cathode. These pores are created using inert substances that immobilize the electrolyte, generally glass fibers or SiO_2. Batteries that use glass fibers are known as AGM (Absorbent Glass Mat), and those that use silicon dioxide are referred to as Gel batteries.

Gel batteries have a larger inter-electrode distance compared to AGM batteries, which implies a larger amount of electrolyte, a larger heat capacity and hence fewer issues with deep discharge[4]. These characteristics result in a longer cycle lifetime of gel technology compared to AGM batteries. This is the main reason why gel batteries are preferred for PV systems applications.

However, due to the thicker electrolyte and the reduced mobility of the ions in the electrolyte, the internal

[1] In VRLA batteries water loss is reduced by at least 98%.

resistance of the gel battery is larger, and AGM batteries are consequently more appropriate for high power applications. On the other hand, gel batteries are more difficult to manufacture than AGM batteries and have a higher cost per unit of energy stored.

5.2.2. Li-ion batteries

There are several types of Li-ion batteries. Consumer electronics generally use $LiCoO_2$ batteries, however, the lithium iron phosphate (LFP) battery is the most used one in PV systems. Although $LiFePO_4$ batteries have a lower cell voltage and energy density (compared to $LiCoO_2$), due to the stronger bond of the oxygen in the phosphate, this type of Li-ion battery is safer and performs better at high temperatures[30].

The structure and main reactions in an LFP battery are shown in Figure 5.4: the cathode material is the phosphate and the anode material is usually graphite (host material) where the Li ions intercalate forming Li_xC. Anionic complexes of Li are used as electrolytes, for example, $LiPF_6$ and $LiBF_4$. The standard potential of a lithium iron phosphate cell is $3.2V$.

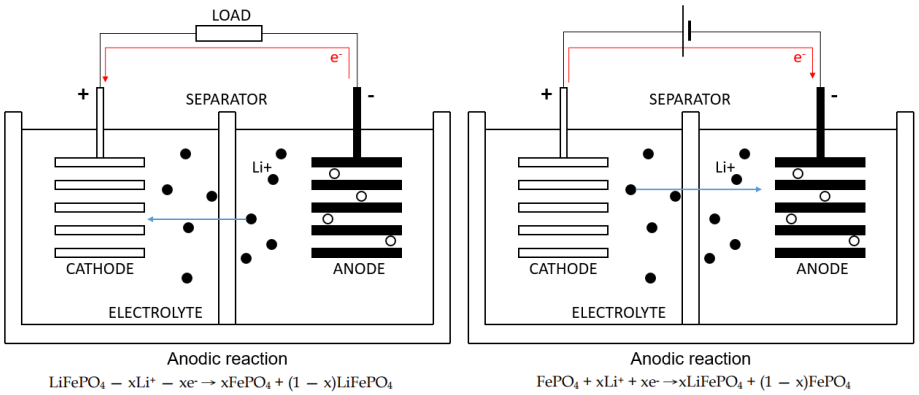

Figure 5.4: $LiFePO_4$ battery main reactions

As the electrodes of a Li-ion battery are much lighter than those of gel batteries, the energy density of Li-ion batteries is higher.

5.2.3. Battery modeling and selection

A brief market research was carried out to further compare both battery technologies. The results of the comparison are given in Table 5.2.

As the battery is cycled, its capacity diminishes as a consequence of multiple effects, among them, electrode wearing and electrolyte degradation. It is considered than when a capacity of a battery drops to 80% of the nominal capacity the battery must be replaced. Battery manufacturers usually indicate how the cycle lifetime is affected by the depth of discharge (DoD) of the battery.

Generally, for VRLA batteries the cycle lifetime drops abruptly when the battery is discharge further than 50%. For 50% DoD the lifetime of a gel battery varies between 400 and 700 cycles, while for an AGM battery it is around 20% lower. Li-ion batteries have a much longer lifetime, and the depth of discharge can be easily extended to 80%. At this DoD a Li-ion battery can be cycled 2500 to 4000 times.

Although the price of Li-ion technology has decreased significantly during the last years, from Table 5.2 it can be concluded that the average cost per unit of energy stored is still three times as high compared to Pb-acid batteries. For this reason, Li-ion is mainly used for high power or mobile applications where the weight is an important constraint.

The temperature also affects the battery performance. At low temperatures, the capacity of a battery drops very rapidly. On the other hand, high temperatures increase the self-discharge rate of a battery. Pb-acid batteries are more resilient to lower temperatures while Li-ion batteries can tolerate higher temperatures. Nonetheless, for the results of the simulations presented in this study, the temperature effects have been neglected.

A simplified electrical model of a battery has been used to determine the required storage capacity depending on the PV power produced. The model assumed represents the battery as an ideal voltage source with an internal resistance. This model is not sufficient to represent the instantaneous current and voltage

Table 5.2: Comparison of batteries available in the market

Type	Brand	Capacity	C_{eff} [Wh]	E_d [Wh/kg]	E_d [Wh/L]	Cost [€/Wh]	Cost [€/cyc]
AGM	Victron	12V - 130Ah	660	17.4	40.5	0.51	0.84
Gel	Dyno	12V - 161Ah	966	23.1	39.4	0.53	0.73
Gel	RPower	12V - 150Ah	900	20.2	45.0	0.45	0.68
Gel	Drypower	12V - 160Ah	960	19.2	55.2	0.63	1.10
Gel	Ultracell	12V - 65Ah	390	20.3	37.9	0.63	0.61
Gel	Victron	12V -165Ah	990	20.6	49.5	0.39	0.77
Li-ion	Victron	12.8V - 160Ah	1638	49.6	65.0	1.13	0.74
Li-ion	RPower	12.8V - 100Ah	1024	70.6	83.9	1.51	0.38
Li-ion	Smart Battery	12.8V -200Ah	2048	62.8	68.5	1.17	0.60

levels of a battery[2], however, it is accurate enough to determine the storage capacity needed and the average battery efficiency.

Figure 5.5 shows the over-potential of a Gel battery during charge and discharge. The slope of the lines corresponds to the internal resistance of the battery.

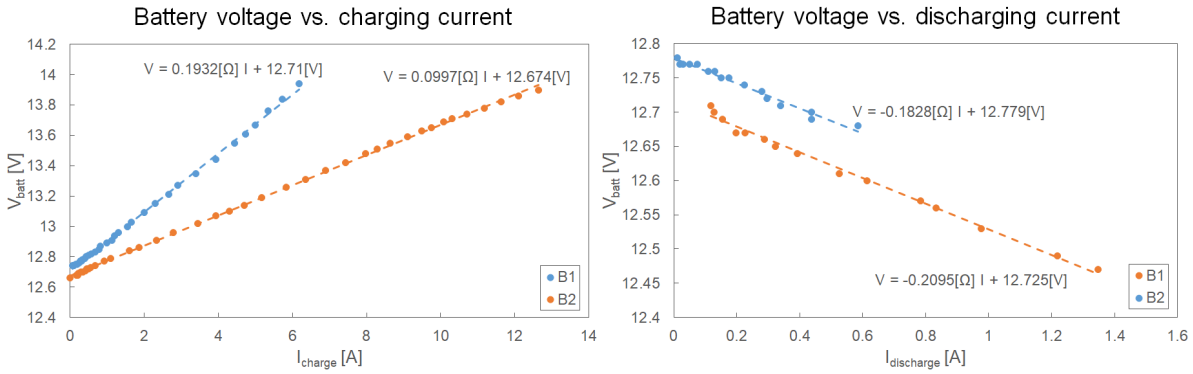

Figure 5.5: DC resistance measurements of the battery 12V 161Ah Gel battery used in the prototype.

Finally, the self-discharge rate of the batteries has been taken into account for the simulations. The self-discharge is a process that occurs even when no load is connected across the terminals of a battery, and is associated with the chemical instability of the electrodes and impurities in the electrolyte. The self-discharge rate has a strong dependence on the temperature. Since the Infotainment Spot was designed for the Netherlands, the temperature of the battery is not an issue. However, in warmer locations, the temperature inside of the kiosk must be taken into account to calculate the required capacity.

5.3. Charge controller

The choice of the charge controller is conditioned by the low number of cells in the PV modules. As mentioned before, the kiosk without a tracking system is powered by two PV modules, one with 14 cells connected in series, and another one with ten cells connected in series. The V_{mpp} of the solar cells used is $0.559V$, which means that the peak power of the PV modules is lower than $7.83V$ and $5.59V$ respectively. Owing to the fact that typical battery voltages, both for Pb-acid and Li-ion, are above 12V, a step-up charge controller is required.

Most PV modules on the market have 48 or more solar cells connected in series. As a consequence, most charge controllers are used to step down the PV module voltage, and there are few boost charge controllers available in the market. The only charge controller found that matched the requirements is the GVB-8 Boost from Genasun. This charge controller can be used to charge a battery of 12V using PV panels that produce at least 4V. However, as shown in Figure 5.6, the efficiency of the charge controller is considerably lower for low input voltage levels: when the PV module voltage is around 10 V the efficiency of the converter is approximately 92%, for an input voltage of around 5 V the efficiency drops to 85%.

[2]More detailed models account for the dynamics of a battery by adding extra capacitances and resistances in the electrical model.

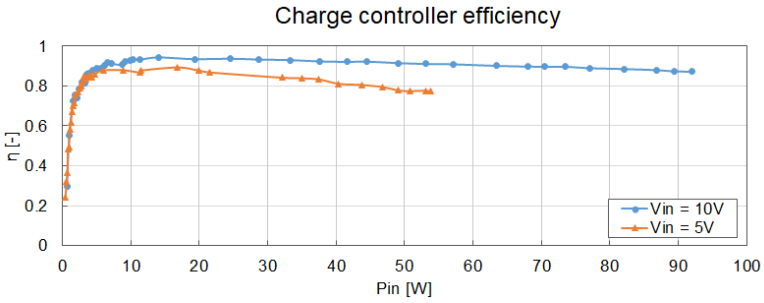

Figure 5.6: Measured efficiency of the boost charge controller using a DC voltage source at different input voltages

It is also important to mention that the charge controller requires at least 0.5 W from the PV modules to start working. The minimum operating power (P_{min-CC}) was taken into account in the simulations.

Along with the DC/DC converter efficiency measurements, the efficiency of the Maximum Power Point Tracking (MPPT) algorithm implemented in the charge controller was determined. In order to measure the efficiency of the algorithm, the charge controller was connected to the 14-cell PV module used to build the prototype, and to a large capacity battery capable of taking all the produced power. The irradiance on the module was measured using two calibrated pyranometers[3]. Additionally, the temperature of the module was measured using two thermocouples placed on the back of the module. The output power of the PV modules was measured and compared to the expected maximum power using the module temperature coefficients, the incident irradiance, and the I-V curve of the module determined under STC. The system was evaluated during 20 minutes taking measurements every 7 seconds; the results are presented in Figure 5.7.

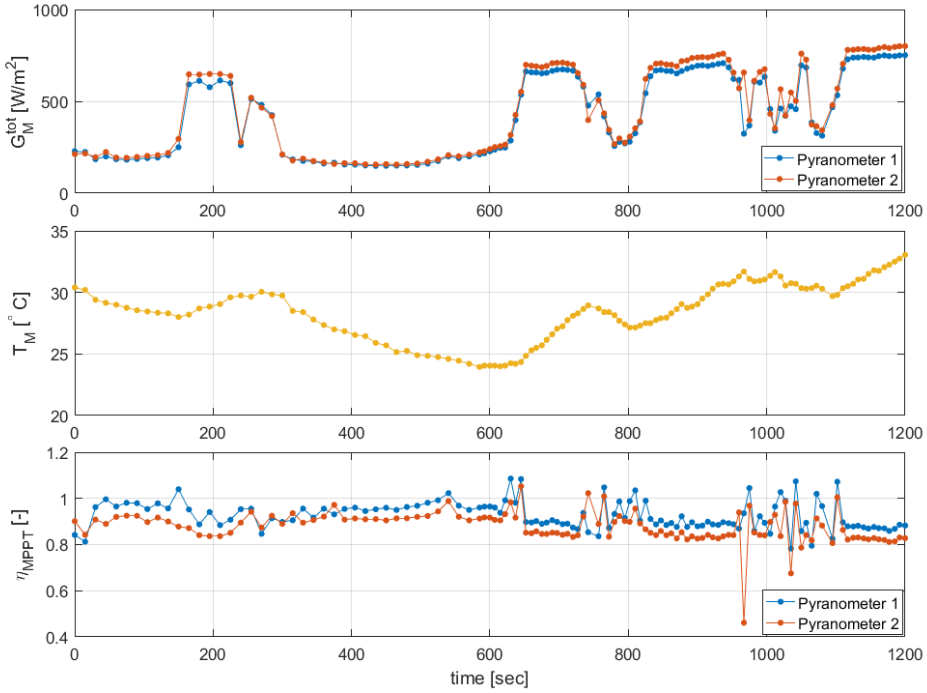

Figure 5.7: MPPT efficiency measurements using the 14 cell KS Flex PV module

In Figure 5.7 the difference between the measured irradiance values can be attributed to a small angular misalignment of the pyranometers. Moreover, in some cases, the calculated MPPT efficiency values are higher than 1. These are measurement errors, and they are a consequence of the response time and the lack of synchronism between the measurement instruments because the errors occur at those moments when the irradiance changed rapidly. Since the data logger of the pyranometers responds much slower than the volt-

[3]The pyranometers used are the Huskeflux LP02-LI19 (Pyranometer 1) and the EKO INSTRUMENTS Integrated Sensor Unit of the MP-11 IV checker (Pyranometer 2).

meters and ammeters used to measure the PV power, the calculations lead to incorrect results. Excluding the efficiency results higher than unity, the average MPPT efficiency is 87.8% and 92.5% using the pyranometers 1 and 2 respectively. The average of both results (90.1%) was used in the simulations.

5.4. Required storage capacity

An algorithm was developed to calculate the minimum storage capacity required for an arbitrary location and orientation of the kiosk taking into account the various energy losses in the system. A block diagram of the algorithm is presented in Appendix I. Using this algorithm, the minimum Gel and Li-ion storage capacities can be compared.

The storage capacity required by the Infotainment Spot installed at the TU Mekelpark bus stop is shown in Figure 5.8.

The required capacity values shown in Figure 5.8 are clearly not symmetrical with respect to the north direction. When the modules are facing west, the capacity required is almost twice as much as when they are facing east. This is because of the influence of the tall EWI building which is placed on the southwest of the bus stop.

As it was expected, the kiosk with a tracking system demands a larger storage capacity. The extra capacity needed is between 10% and 15% higher. These values are even higher than the reported differences in the energy yield, which showed that the static kiosk could harvest in 4% more energy in average. The reason for this apparent discrepancy is that for the kiosk with a tracking system there are larger differences between the power generated in summer and winter, a most of the extra power generated in summer is dumped.

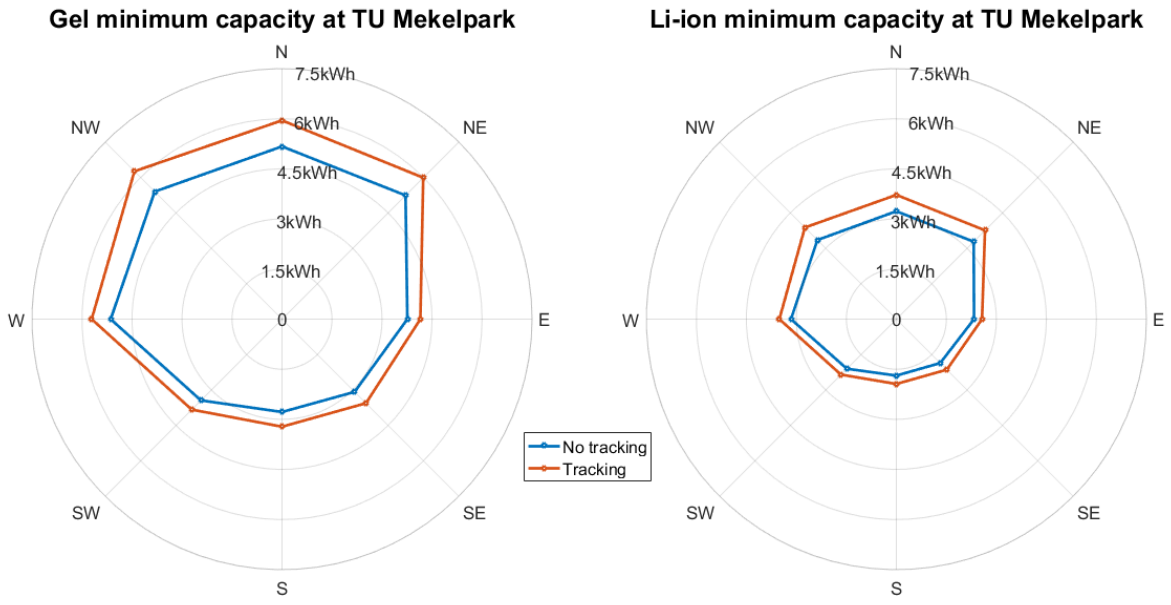

Figure 5.8: Minimum required storage capacity depending on the PV module orientation

Furthermore, it was found that in average 40% less storage capacity is required when using Li-ion batteries. The reduction is mainly due to the deeper DoD of lithium batteries (30% deeper), but also the higher efficiency and the lower self-discharge rate contribute to decreasing the capacity.

Although 40% less capacity is required, a Li-ion battery for the kiosk is (according to Table 5.2) still 80% more expensive than a Gel battery per unit of storage capacity. If the cycle lifetime is also taken into account, then Li-ion batteries become more convenient because they last for at least twice as many cycles as gel batteries, ultimately making Li-ion technology 10% cheaper in the long run. Nevertheless, for the implementation of the prototype of the Infotainment Spot gel technology was used.

At TU Mekelpark bus stop, the road goes along the south-southeast direction, which means that if the kiosk is perpendicular to the street, the PV modules should be facing east-northeast. From Figure 5.8, the required storage capacity is 3750 Wh when the modules are facing east, and 5240 Wh when the modules are

facing northeast. Owing to the large difference, it is more convenient break the perpendicularity between the road and the kiosk, and to orient the modules slightly more towards the east.

Another aspect that was investigated is how does the peak power of the kiosk affect the required storage capacity. The kiosk designed has 24 solar cells of $5.03 W_p$ each. Figure 5.9 shows that the storage capacity drops linearly with the number cells on the flat PV module of the kiosk. At TU Mekelpark the drop in the required gel capacity is around 108 Wh/cell, while in the case of a free horizon the drop is approximately 42 Wh/cell. In both cases, the reduction per added cell is approximately 3% of the required storage capacity. Since PV modules are much cheaper than storage capacity, from an economic perspective, it would be more convenient to add more cells to the kiosk. Nonetheless, a kiosk with 26 cells is already too tall and less aesthetic, and the 24-cell version was chosen.

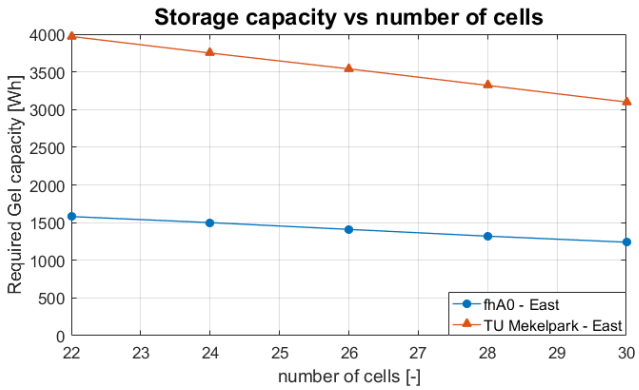

Figure 5.9: Sensitivity analysis of the gel storage capacity on the number of cells.

5.4.1. State of charge

The state of charge of the battery throughout the year is very important to know if the battery is going to achieve the expected lifetime.

The cycle lifetime mentioned in previous sections implies a regular charging and discharging process of the battery. However, as shown in Figure 5.10, the battery is not used with such regularity.

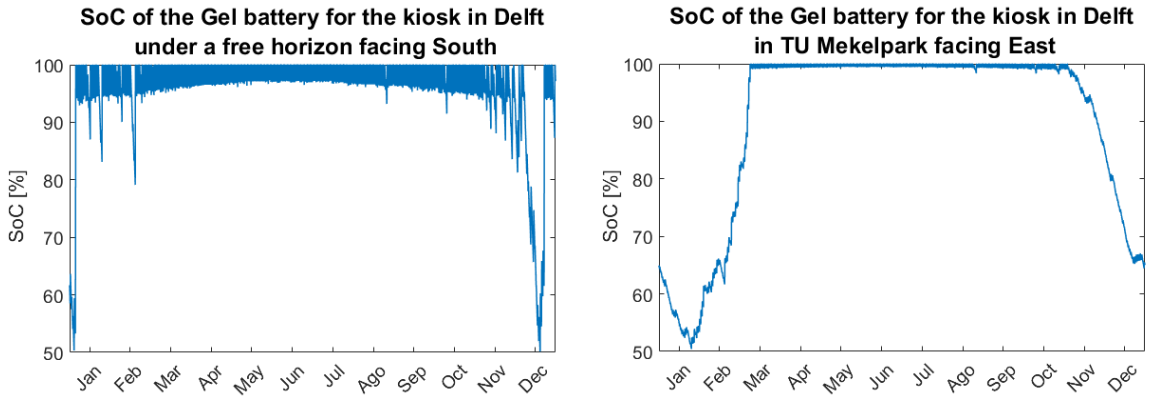

Figure 5.10: State of charge of the battery during an entire year under two different skyline profiles.

If the kiosk is placed in a location with a free horizon and facing south, the storage capacity required is 670 Wh, and the DoD of most cycles is around 5%. The SoC of the battery only drops down to 50% a couple of days per year. Consequently, it is expected that the battery will last longer than the specified number of cycles at a DoD of 50%.

On the other hand, in a more realistic scenario, the SoC profile looks like the plot on the right in Figure 5.10. In this case, the required capacity is 3750 Wh, and from the beginning of autumn to the beginning of spring the SoC of the battery is always below 100%, and it reaches a minimum in January. Moreover, due to the

larger nominal capacity of the battery, the daily DoD during spring and summer is only 1%. To ensure that the battery will perform as expected, it is necessary to recharge the battery to 100% at least once during winter. This helps to slow down the sulfation of the electrodes, which is a process characterized by an accelerated loss in the nominal capacity as a consequence of the crystallization of lead sulfate on the active electrode material.

5.4.2. Loss of load probability

The loss of load probability (LLP) quantifies the inability of a PV system to supply the load during a specific interval of time. It is defined as the ratio between the average power required by the load that cannot be provided by the off-grid system (E_{fail}) and the total energy consumed by the load[27]:

$$LLP = \frac{E_{fail}}{\int_{year} P_{LOAD} \cdot dt} \tag{5.1}$$

The definition in equation 5.1 is not applicable for the Infotainment Spot design because the storage capacity has been calculated so that there is always a minimum amount of energy remaining in the battery to prolong the cycle lifetime. In other words, the if the LLP is calculated using equation 5.1 it would be null. Hence, another criterion has been applied to give an LLP value.

As mentioned before, sealed Pb-acid batteries must be periodically charged to 100% to extend the cycle lifetime. Based on this requirement, it is suggested to disconnect all the loads from the system during six consecutive days in winter to allow the battery to be fully recharged. If the disconnection of the load is done based on the weather forecast, approximately $1500Wh$ can be harvested in 6 days. This procedure would allow to fully recharge most off-grid kiosks. Taking into account that the tablet can still be powered by the internal battery for two days, the system would be out of service only for four days. The LLP of the kiosk would then be 0.011 which is considered an acceptable value for this type of applications[26].

5.4.3. Energy damping

A low LLP off-grid system in the Netherlands will naturally dump most of the harvested energy during summer. This is a consequence of the non-uniformity of the incident solar radiation throughout the year. In average the global horizontal irradiation is 1100 kWh/year/m^2, but the irradiance during summer is up to 8 times higher than during winter. Therefore, the irradiation during winter is the one that determines the minimum storage capacity, and most of the energy produced during the rest of the year is dumped.

In this sense, the Netherlands is not an ideal place for off-grid PV systems. Other locations with similar annual irradiation values have a much more distributed irradiance during the entire year, and the difference between summer and winter is given by a factor of 3 to 4 (see Figure 5.11).

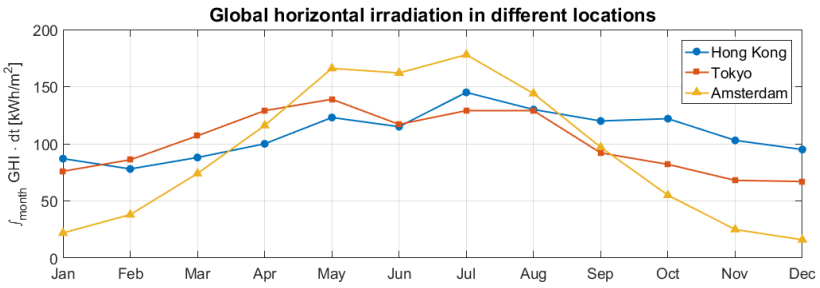

Figure 5.11: Monthly global horizontal irradiation using Meteonorm data (year 2016) for Amsterdam, Tokyo, and Hong Kong

The simulations have shown that for the kiosk installed in Delft in a place with a free horizon and facing south, the PV modules could generate 93.0 kWh during an entire year, but 70.4 kWh would be dumped (using 670 Wh of gel batteries). This equals to a dumping ratio of almost 76%. Figure 5.12 there is a high dumping ratio even during winter.

A more realistic case is shown in Figure 5.13 for the kiosk installed in Delft, at the bus stop TU Aula facing southwest. The minimum storage energy required in this case is 1220Wh. Here the PV generated power is lower, and all the available PV power during January and December must be used to charge the battery. The total generated power is 74.0kWh, and the resulting dumping ratio is 71%.

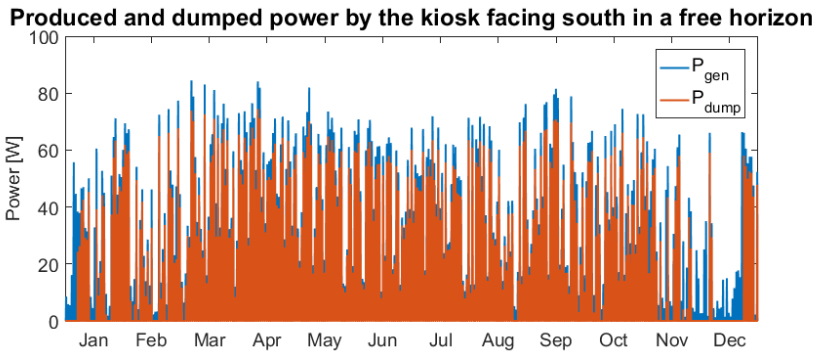

Figure 5.12: Energy dumping for a free horizon

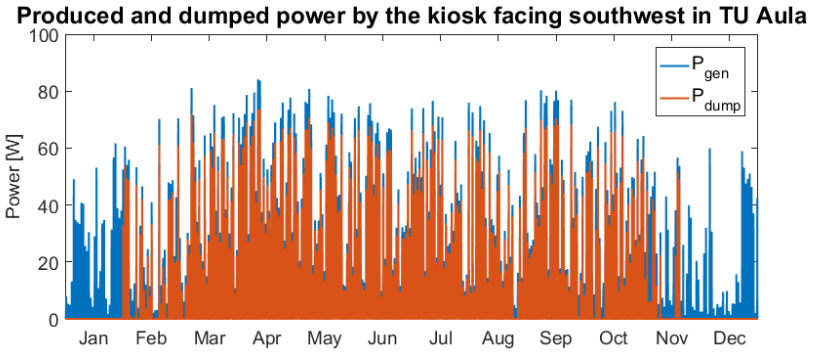

Figure 5.13: Energy dumping at TU Aula

5.4.4. The storage capacity and the energy yield during winter

The elevated dumping ratio indicates that the required storage capacity strongly depends on the energy harvested during winter. In fact, Figure 5.14 shows a strong interdependence between the energy generated between December and January and the minimum storage capacity. This correlation supports the decision made in Chapter 4 to optimize the tilt angle of the structure for the winter months. The association follows a trend that is limited by the two dashed lines shown in the plot.

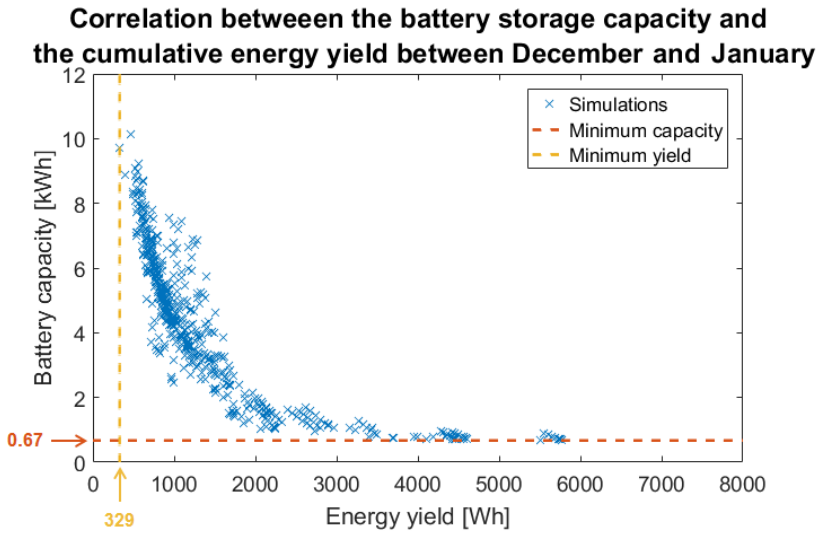

Figure 5.14: Correlation between the minimum battery (gel) capacity required and the energy yield of the kiosk during winter in Delft

The vertical line shows that the energy yield during December and January must be at least larger than

329 Wh for the kiosk to be able to operate during the year without interruptions. If the yield is lower than this value, the energy demand becomes larger than the available energy and the loss of load probability increases beyond acceptable limits.

The horizontal line at 670 Wh represents the minimum storage capacity that the system requires to operate independently of the yield during winter. This lower limit shows that when the energy yield during winter increases beyond 4000 Wh, the required energy capacity remains almost constant. In order to understand this effect, it must be taken into account that the daily energy consumption of the system is approximately 50 Wh. As the daily energy demand becomes comparable to the available energy stored in the battery, the daily variations in the irradiation limit the minimum capacity. In other words, the effect of an entire week of cloudy or rainy days has a much stronger effect on the state of charge of the battery.

Finally, it was found that there is a minimum value of the sky view factor for the acceptable locations and orientations of the kiosk. The flat module of the installed Infotainment Spot must have a sky view factor larger than 0.18. Moreover, there is no limit on the maximum acceptable sun coverage factor. The reason for this is that during winter around 70% to 80% of the radiation is diffuse, and hence the yield is strongly related to the SVF value.

5.5. The prototype

The prototype was assembled using the components shown in Figure 5.15. Additionally, protective fuses have been added in all the components to prevent any of the loads to short-circuit the batteries. The prototype was meant to be placed at TU Mekelepark, and is equipped with two gel batteries of 12 V and 161 Ah.

Figure 5.15: Components of Infotainment Spot

A picture of the finalized prototype is shown in Figure 5.16.

Figure 5.16: Picture of the finalized prototype.

5.5.1. Cost estimation

The total cost of the prototype was approximately 5000 euros. This figure includes only the cost of the components, the actual cost of the kiosk would be slightly higher if the cost of labor was taken into account. The breakdown of the cost is shown in Figure 5.17.

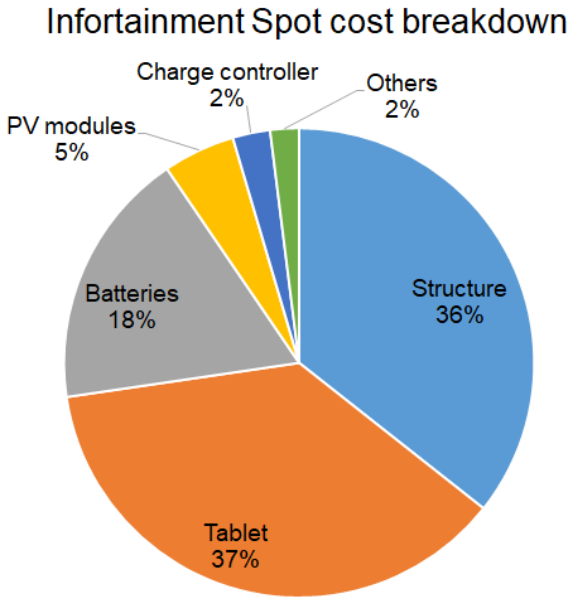

Figure 5.17: Share of each components on the final cost of the Infotainment Spot prototype

The most expensive component of the kiosk is the rugged tablet. It represents 37% of the total cost. The metallic structure is almost as expensive as the tablet. The breakdown also shows that the batteries are more than three times more expensive than the PV modules. The PV modules, according to the trend in recent years, are one of the cheapest components of a PV system.

As mentioned before, for the Netherlands the most convenient option would be to make the kiosk a grid-tied system. Not only the cost of the batteries would be saved, but also other users in the grid could take advantage of the energy that is dumped during summer.

If a grid-tied kiosk is massively produced, the cost of the structure could be reduced in around 40%. Moreover, the tablet could be replaced by a touchscreen and a computer. A customized solution for the user interface could imply a 50% cost reduction compared to a rugged tablet. Under these assumptions, a grid-tied kiosk could be manufactured for half the cost of the prototype.

5.6. Summary

In this chapter, the loads of the system were characterized to generate a load profile. Based on the load profile the storage requirements of the system were calculated, and the LLP and the damping ratio of the system have been studied. Finally, the Infotainment Spot prototype was presented, and a simple cost estimation was given.

Chapter 5 allowed to answer the last research question. The answers to the sub-questions are summarized below.

What are the limitations of an off-grid Infotainment Spot?

(a) *What is the best battery technology for this application?*
Simulations have shown that when lithium iron phosphate batteries are used, 40% less storage capacity is needed compared to Pb-acid. Although Li-ion technology is three times more expensive than VRLA, if the battery efficiency and the cycle lifetime are taken into account, in the long run Li-ion is 10% cheaper than VRLA.

(b) *What is the effect of winter on the required storage capacity?*
The large fluctuations in the monthly irradiation in the Netherlands, result in a strong correlation between the energy yield in winter and the required storage capacity. Depending on the skyline profile characteristics, during December and January, the PV modules can generate from a few hundred up to 6000 kWh. It has been found that the minimum energy yield during these months must be larger than 329 Wh in order for the system to operate with an acceptable loss of load probability.

(c) *Are there restrictions on the skyline profiles characteristics for the acceptable locations?*
Most winter days in the Netherlands are cloudy, and therefore most of the solar radiation is diffuse. Due to the dependency of the diffuse radiation on the sky view factor, it was found that the SVF in the acceptable locations must be at least larger than 0.18.

6

Conclusions and outlook

6.1. Conclusions

The primary goal of this thesis project was to investigate the effects of urban landscapes on the performance of a PV system. One specific system has been the study object: a new version of the Infotainment Spot was designed, and the performance of the system was assessed under a wide range of skyline profiles.

Several physical models were considered to evaluate the performance of a PV system, and based on these, a simulation framework was developed. Using this framework, significant relationships between the energy yield and the characteristics of the skyline profiles have been found. The correlations allowed the creation of a simplified model for estimating the energy yield of a PV system. Additionally, the storage requirements of the Infotainment Spot have been determined for different locations and orientations.

Throughout this study, the three research questions proposed in the first chapter have been addressed. The questions and the corresponding answers are synthesized below.

1. **What is the effect of implementing a tracking system on the Infotainment Spot?**

   (a) *How can a tracking system be optimized?*

   The implementation of a horizontal axis tracking system in the Infotainment Spot allows it to follow the sun along throughout the year. The tilt angles that maximize the energy yield were determined, and it was shown that a discrete (monthly) tracking system is preferable to a continuous tracking. The use of a monthly tracking system results in almost the same yield, and it offers a significant reduction in complexity and wearing of the mechanical components.

   (b) *What is the gain in the harvested energy by using a tracking system when compared to a fixed tilt system?*

   If two Infotainment Spots with a peak power equal to 110.7 W are compared, the system with a solar tracker in one year can generate 4% more energy in average. However, if all available space on the back of the kiosk is exploited, two more cells can be accommodated in the static design increasing the peak power to 120.7 W. It was shown that higher peak power alternative always has a higher performance, and it can generate 3% more energy in one year.

2. **Can the characteristics of a skyline profile be quantified to create a simplified model for estimating the energy yield of a PV system?**

   (a) *What are the relevant parameters?*

   The characteristics of a skyline profile can be effectively described using two parameters: the sky view factor (SVF) and the sun coverage factor (SCF).

   The sky view factor, the visible proportion of the sky in a given location, allows calculating the energy yield resulting from the diffuse isotropic, the horizon brightening and the ground reflected radiation components.

The sun coverage factor has been introduced as part of this study, and it is defined as the ratio between the number of hours the sun is covered by the skyline profile, and the total number of hours the sun is above the horizon. The SVF is used to estimate the energy yield resulting from the direct beam and the diffuse circumsolar radiation components.

(b) *What is the reach and the limitations of the model?*

The proposed estimation model for estimating the energy yield is expressed by Equation 4.5:

$$\hat{E_y} = (a_2 \cdot SCF^2 + a_1 \cdot SCF + a_0) + (b_2 \cdot SVF^2 + b_1 \cdot SVF + b_0)$$

This model requires six empirical coefficients that have been calculated for five different cities using meteorological data from years 2005, 2010 and 2015. The model applies to any location in Utrecht, North and South Holland.

One relevant feature of this model is that it can be scaled to predict the energy yield of a system with a higher peak power and the same tilt angle.

The prediction has two main limitations. First, the objects that constitute the skyline profile must be at least 3 m away from the PV modules to ensure that the reflected light on these surfaces can be neglected. Second, the accuracy of the model improves the more separated the solar modules are from the ground. When the module is too close to the ground, the ground-reflected light causes the total irradiance to vary about 5% along the module.

(c) *What is the accuracy of the estimation?*

The accuracy of the model is about ±10% for years with average irradiation levels. However, when the annual irradiation increases in 15%, the prediction in the worst case underestimates the yield by 20%.

3. **What are the storage requirements of an off-grid Infotainment Spot?**

(a) *What is the best battery technology for this application?*

Simulations have shown that by using lithium iron phosphate batteries, 40% less storage capacity is needed compared to Pb-acid. Although Li-ion technology is yet three times more expensive than VRLA, if the battery efficiency and the cycle lifetime are taken into account, Li-ion results 10% cheaper than VRLA.

(b) *What is the effect of winter on the required storage capacity?*

The large fluctuations in the monthly irradiation in the Netherlands result in a strong correlation between the energy yield in winter and the required storage capacity. Depending on the skyline profile characteristics, during December and January, the Infotainment spot can generate from a few hundred up to 6000 kWh. From this correlation, it was determined that the minimum energy yield during these months must be larger than 329 Wh in order for the system to operate with an acceptable loss of load probability.

(c) *Are there restrictions on the skyline profiles characteristics for the acceptable locations?*

Most winter days in The Netherlands are cloudy, and therefore most of the solar radiation during winter is diffuse. Since the diffuse radiation is related to the sky view factor, it was found that the SVF in the acceptable locations must be at least larger than 0.18.

6.2. Outlook

To conclude this report, three ideas to continue the research line of this project are proposed.

6.2.1. Energy potential mapping

In Chapter 4, a 3D map of the city of Delft created using LIDAR data was introduced. The corresponding point cloud has an accuracy of 1 meter, and it can be generated for any Dutch city. Therefore, using LIDAR data it is possible to reconstruct the skyline profile at any point on the map, and through the method presented in Chapter 3, the SCF and SVF values can be calculated. Once the characteristics of the skyline profile in

a specific location are determined, the energy estimation model based on synthetic skyline profiles can be applied to calculate the performance of a PV system.

The combination of LIDAR data and the simplified energy yield estimation model makes it possible the calculation of an accurate energy yield map for any city in The Netherlands. Such a tool could give an insight of what are the most profitable locations in a city to install a PV system.

6.2.2. Monitoring system for the infotainment spot

The prototype of the Infotainment Spot should be equipped with a monitoring system for the battery and the PV modules. The monitoring system could be used to measure the state of charge of the battery as well as the produced power during long intervals of time.

The PV power measurements combined with irradiance measurements from nearby weather stations could be used to validate the framework proposed in Chapter 3 with real measured data. Moreover, the validation could be extended by performing measurements with pyranometers in a free horizon location. By using obstacles to simulate the skyline profile, the effect on the irradiance components could be verified.

On the other hand, the SoC measurements could be useful for validating the battery simulation model. Furthermore, the actual lifetime of the battery could be determined and compared to the reported cycle lifetime.

6.2.3. Utilization of the Infotainment Spots as distributed energy storage units

This study has shown that The Netherlands, owing to the specially irregular seasonal irradiance patterns, is not a convenient location for off-grid PV systems. Grid-tied PV systems are significantly cheaper since they prescind from an energy storage system. Furthermore, a grid-connected PV system can exploit the PV power generated during summer, which in an off-grid system is mostly dumped.

The installation of off-grid PV systems is more sensible in locations where the electrical network is not reliable, or where the seasonal irradiance patterns are more uniform.

There is, however, one reason to promote the installation of energy storage systems in The Netherlands. In the future, the share of renewable sources in the total electricity generation will significantly increase, and batteries could be an alternative to mitigate the natural fluctuations of the renewable power sources. Nevertheless, for the storage units to be functional, the PV system must be grid connected to allow the power flow between different units in the grid. The batteries in Infotainment Spots could be integrated into a microgrid, which would allow taking advantage of the whole installed storage capacity.

A

Thermal performance measurements

Kameleon Solar specializes in the design of customized PV solutions. The PV modules Kameleon Solar manufactures are specifically designed for each customer. For this reason, it is not possible for the company to provide all the information that is needed to accurately simulate the behaviour of a solar module. In particular, Kameleon Solar does not provide the Nominal Operating Cell Temperature (NOCT) which is needed to determine the determine the effect of temperature on the module efficiency. In this appendix the experiments carried out to determine this parameter are described. These measurements have been taken following IEC standards at Eternal Sun's facilities.

NOCT and NMOT

The Nominal Operating Cell Temperature (NOCT) as menitoned previously is a parameter that characterizes the thermal performance of a PV module. According to the IEC61215 (Ed. 2) standard, it is defined as the cell temperature within an open-rack mounted module under the following conditions:

- Tilt angle : 45°
- Total irradiance: $800 W/m^2$ (AM1.5)
- Ambient temperature: $20°C$
- Wind speed: $1 m/s$
- Electrical load: Open circuit.

At the moment the NOCT is the parameter that most PV module manufacturers give to characterize their modules. However, it is more useful to study the performance of the the module under load conditions close to the maximum power point of the module, since this is more representative of real operating conditions. For this reason, a new standard has defined a parameter (NMOT) that characterizes the performance of the module when loaded close to its maximum power point.

According to the IEC61215 (Ed. 3) standard, the Nominal Module Operating Temperature (NMOT) is defined as the equilibrium mean solar cell junction temperature within an open-rack mounted module operating near the peak power in the following standard reference environment:

- Tilt angle : $(37 \pm 5)°$
- Total irradiance: $800 W/m^2$ (AM1.5)
- Ambient temperature: $20°C$
- Wind speed: $1 m/s$
- Electrical load: A resistive load sized such that the module will operate near its maximum power point at STC or an electronic maximum power point tracker (MPPT).

The NMOT is naturally lower than the NOCT since part of the energy that reaches the solar cell generates charge carriers, which take some power away from the module that would otherwise be turned into heat.

The standard that describes the measurement methodology defines that the measurements are to be taken in outdoors. In open environments the irradiance, ambient temperature and wind speed are hard to control. An indoor version of the experiments has been applied to characterize Kameleon Solar's PV modules. Since there is no standard that specifies how these measurements should be taken indoors, the measurement procedure followed is described below.

Standard Measurement procedure

The outdoor's measurement procedure and module mounting are described in the standard IEC61853-2. The standard defines that a temperature sensor with an accuracy of $\pm 1^{\circ}C$ and a repeatability of $\pm 0.5^{\circ}C$ must be used to record at least once per second the cell temperature of the at 4 different points on the back of the PV module. Additionally, a pyranometer is needed to measure the irradiance on the same plane as the modules, a thermometer to measure the ambient temperature and a anemometer to register the wind speed.

Indoors measurements

In order to take the measurements indoors the solar simulator LA150200 has been used. This equipment fabricated by Eternal Sun is an AAA class large area steady-state solar simulator which intensity can be dimmed to perform NOCT and NMOT measurements. The required wind speed was generated using a wind generator that was attached to the measurement bed as shown in Figure A.1. Both the LASS and the measurement bed were tilted at 37° with respect to the ground.

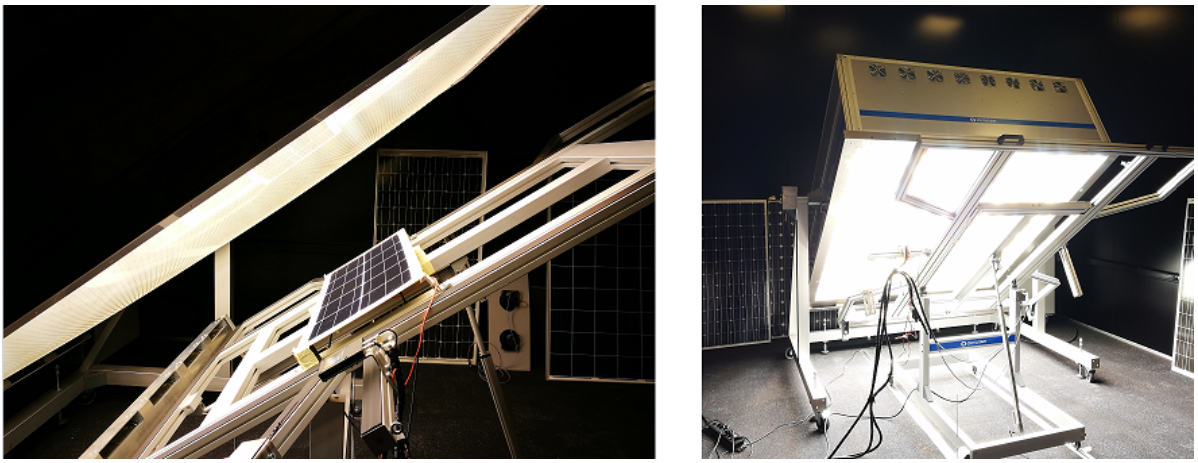

Figure A.1: NMOT measurement setup

The wind speed was measured with a digital anemometer at $1cm$ from the front and the back surfaces, while the temperature was measured using a thermocouple in contact with the back of the panel and with an IR thermometer on every cell[1].

The spectrum generated by the LASS differs from the AM1.5 spectrum specially on the IR band. The intensity has been therefore adjusted to $600W/m^2$ in the spectral band between $400nm$ and $1100nm$ so that the total intensity incident on the panel was $800W/m^2$ according to the standard specifications.

During the measurements the panel was kept close to the MPPT using a DC electrical load which was adjusted manually repeatedly and the temperature of the room was regulated with an air conditioning unit.

Results

The PV module was tested during 60 minutes. During this period the irradiance in the spectral band between $400nm$ and $1100nm$ oscillated between $603W/m^2$ and $614W/m^2$ (as measured with a calibrated reference cell). The minimum and maximum wind speeds on the front side of the panel were $1.0m/s$ and $1.4m/s$, while on the back of the module the measured wind speeds were $0.75m/s$ and $1.1m/s$ respectively.

[1] The front and the back temperatures of each cell were measured with the IR thermometer emissivity setting at 0.9.

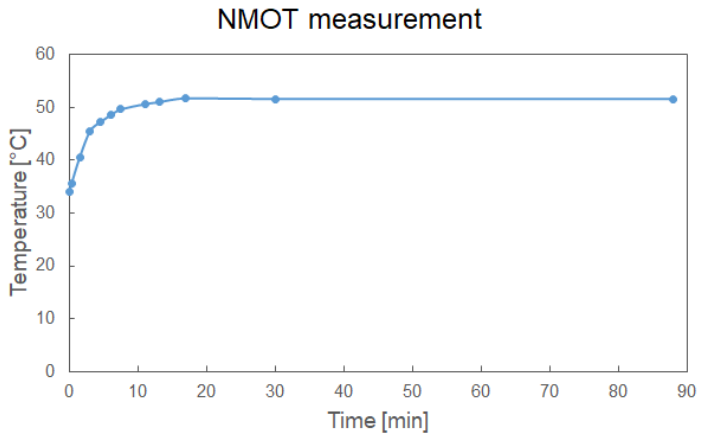

Figure A.2: Progress of the module temperature during the NMOT measurements

The evolution of the average temperature in time is shown in Figure A.2. The resulting NMOT of the panel was $(51.7 \pm 2)°C$, and the maximum power of the PV module dropped from $40.5W$ to $37.3W$ from the beginning to the end of the session.

After performing the NMOT measurement, the panel was left at open circuit for 20 minutes to measure the NOCT. The measured NOCT value was $(55.4 \pm 2)°C$.

B

Equiangular projection of a tilted plane

Let's consider a PV module tilted θ_m degrees (module elevation: $a_m = \frac{\pi}{2} - \theta_m$, and oriented with and azimuth A_m.

The normal vector to the plane of incidence is given by:

$$\vec{n} = \left[\cos(A_M)\sin(a_M); \sin(A_M)\sin(a_M); \cos(a_M)\right] \tag{B.1}$$

if the planes includes the origin then its equation in Cartesian coordinates is given by:

$$\vec{n} \cdot \begin{bmatrix} x \\ y \\ z \end{bmatrix} = 0 \tag{B.2}$$

Now let's consider a sphere of unit radius center at the origin as shown in Figure B.1. The sphere is defined by:

$$x^2 + y^2 + z^2 = 1 \tag{B.3}$$

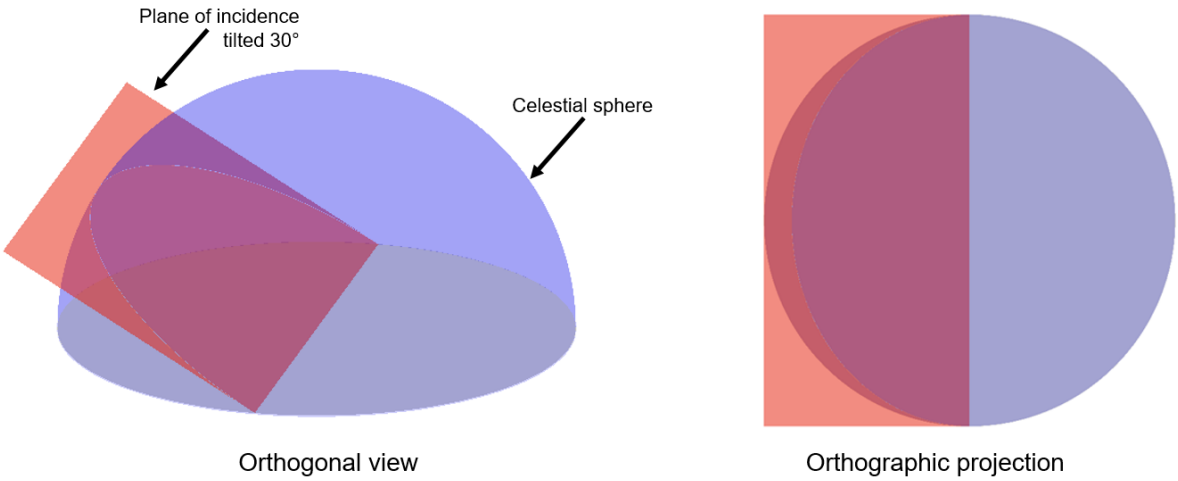

Figure B.1: Representation of the intersection between a tilted plane and the celestial sphere

By isolating z in Equation B.2 and substituting in Equation B.3 the orthographic projection of the intersection between the sphere and the module's plane on the x-y plane can be obtained:

$$\gamma_1 \cdot x^2 + \gamma_2 \cdot x \cdot y + \gamma_3 \cdot y^2 = 1 \tag{B.4}$$

where

$$\gamma_1 = 1 + \cos(A_M)^2 \tan(a_M)^2 \tag{B.5}$$

$$\gamma_2 = \sin(2 \cdot A_M) \cdot \tan(a_M)^2 \tag{B.6}$$

$$\gamma_3 = 1 + \sin(A_M)^2 \tan(a_M)^2 \tag{B.7}$$

By converting equation B.4 from Cartesian to polar coordinates (ρ,ϕ), it is possible to describe the distance of any point on the ellipse the to the origin as a function of γ_i and ϕ:

$$\rho = \left(\gamma_1 \cos(\phi)^2 + \frac{\gamma_2}{2} \sin(2 \cdot \phi) + \gamma_3 \sin(\phi)^2\right)^{-\frac{1}{2}} \tag{B.8}$$

However, in order to apply Steyn method [28] for calculating the sky view factor it is necessary to obtain the equiangular projection of the intersection on the x-y plane. The equiangular projection distance is a function of the radius of the sphere (R) and the elevation angle (δ) and it is given by:

$$r = 2 \cdot R \frac{\delta}{\pi} \tag{B.9}$$

Using Figure B.2 and Equation B.9 it is possible to derive the relation between the equiangular and orthographic projected distances:

$$r = \frac{2 \cdot \rho}{\sin(\delta)} \cdot \frac{\delta}{\pi} \tag{B.10}$$

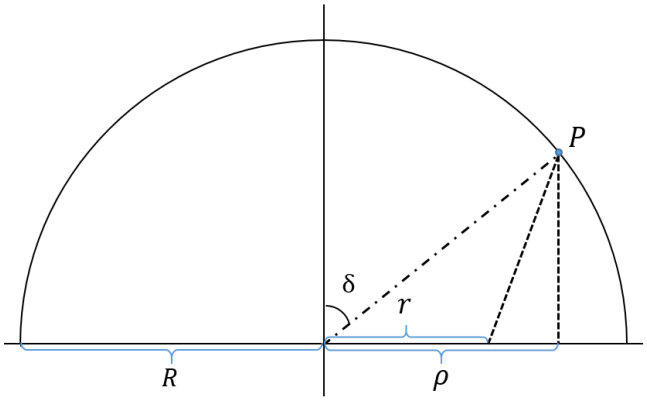

Figure B.2: Orthographic (ρ) and equiangular (r) projections of point P

By realizing that in this case $\delta = \arccos(\rho)$ and applying this transformation to Equation B.8, it is possible to find an expression for the equiangular projection of the intersection between the module's plane and the celestial sphere as a function of γ_i and ϕ:

$$r = \frac{2 \cdot \rho}{\sin(\arccos(\rho))} \cdot \frac{\arccos(\rho)}{\pi} \quad where \quad \rho = \left(\gamma_1 \cos(\phi)^2 + \frac{\gamma_2}{2} \sin(2 \cdot \phi) + \gamma_3 \sin(\phi)^2\right)^{-\frac{1}{2}} \tag{B.11}$$

In Figure B.3 the equiangular and the orthographic projections of a plane tilted 30° are compared.

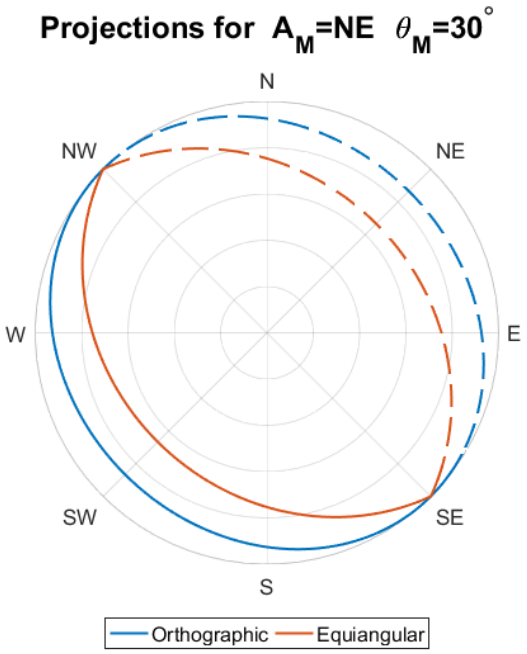

Figure B.3: Orthographic and equiangular projections of the intersection between the module's plane and the celestial sphere

C

Mutual shading

Let's consider a flat surface tilted θ_B degrees. On top of this surface to flat flaps of length m are mounted as indicated in Figure C.1 where s represents the spacing between flaps. Each of the flaps can have a different tilt, in this case θ_1 denotes the tilt of the top flap and θ_2 that of the bottom flap.

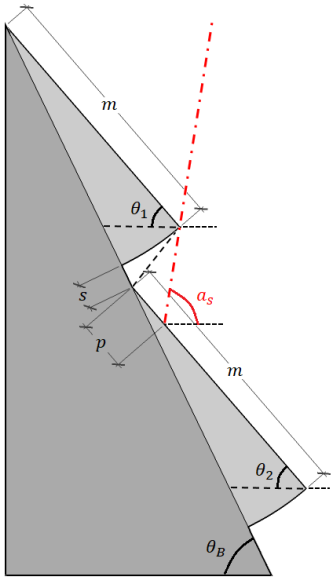

Figure C.1: Trigonometric description of the structure

In order to determine the length of the length of the projected shadow of the top flap on the bottom one (p) when the sun altitude is a_s the auxiliary triangles shown in Figure C.2 must be considered. In Figure C.2 the length of the flap is denoted as $\overline{AC}$, the separation between flaps is $\overline{DE}$, and the length of the shadow on the bottom flap is $\overline{EG}$.

From triangle ΔABC, α_1 is defined as:

$$\alpha_1 = \theta_B - \theta_1 \tag{C.1}$$

The distance $\overline{BC}$ can be calculated by applying the sine theorem to triangle ΔABC:

$$\overline{BC} = \overline{AC} \cdot \frac{sin(\alpha_1)}{sin(\theta_B)} \tag{C.2}$$

From the isosceles triangle ΔADC:

$$\delta_1 = \frac{\pi}{2} - \frac{\theta_B + \theta_1}{2} \tag{C.3}$$

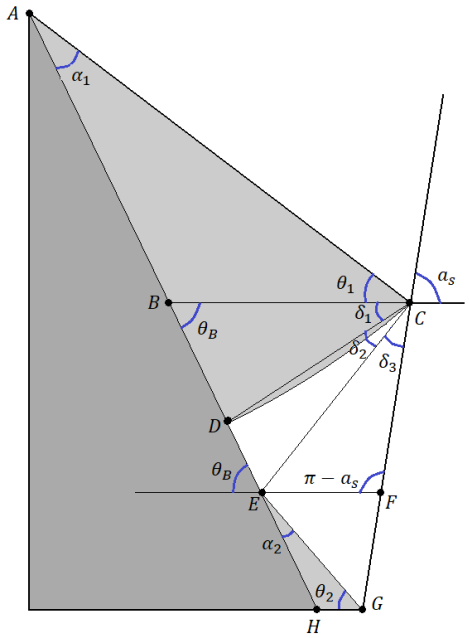

Figure C.2: Auxiliary angles and distances

Distance $\overline{CD}$ can be obtained by by applying the sine theorem to triangle ΔBCD:

$$\overline{CD} = \overline{BC} \cdot \frac{sin(\theta_B)}{cos(\alpha_1/2)} = \overline{AC} \cdot \frac{sin(\alpha_1)}{cos(\frac{\alpha_1}{2})} \tag{C.4}$$

Distance $\overline{CE}$ can be obtained by applying the cosine theorem to triangle ΔCDE:

$$\overline{CE} = \sqrt{\overline{CD}^2 + \overline{DE}^2 - 2 \cdot \overline{CD} \cdot \overline{DE} \cdot cos(\frac{\pi + \alpha_1}{2})} \tag{C.5}$$

By applying the sine theorem to triangle ΔCDE:

$$\delta_2 = arcsin\Big(\frac{\overline{DE}}{\overline{CE}} \cdot cos(\frac{\alpha_1}{2})\Big) \tag{C.6}$$

From the relation between the angles opposed by the vertex at C:

$$\delta_3 = a_s + \frac{\theta_B + \theta_1}{2} - \frac{\pi}{2} - arcsin\Big(\frac{\overline{DE}}{\overline{CE}} \cdot cos(\frac{\alpha_1}{2})\Big) \tag{C.7}$$

Finally, the length of the shadow ($\overline{EG}$ or p in Figure C.1) can be obtained by applying the sine theorem to triangle ΔCEG:

$$p = \overline{EG} = \frac{sin(\delta_3)}{sin(\theta_2 + a_s)} \cdot \overline{CE} \tag{C.8}$$

Combining Equations C.8, C.7, C.5, C.4, and C.1 an expression for the shadow length depending only on the tilt angles, the flap length and the module spacing can be obtained.

D

Energy yield simulation parameters

Tables D.1 and D.2 present all the parameters considered for calculating the energy yield of the Infotainment Spot and the minimum storage capacity.

Table D.1: Energy yield simulation parameters

Parameter	Value
Structure tilt	75°
Bending radius	1 m
A_{cell}	232 cm^2
η_{cell}	18%
ϵ_{back}	0.89
ϵ_{top}	0.84
T_{INMOT}	69.7°C
$\kappa_{I_{SC}}$	+3.88 mA/$^\circ C$
$\kappa_{V_{OC}}$	-1.84 mV/$^\circ C$
κ_{η}	-0.38%/$^\circ C$
α_{gnd}	0.15

Table D.2: Battery simulation parameters

	V_{nom} [V]	R_{int} [Ω]	Self-discharge [%/yr]	SOC_{min} [%]	SOC_{max} [%]
Li-ion	12.8	200	20	20	100
Gel	12	50	30	50	100

Figure D.1 shows the three modules designed by Kameleon Solar for the Infotainment spot. The module on the left is the flat module for the fixed-tilt version. The module in the middle was bent and curved upper part of the kiosk. The module on the right was designed for the Infotainment Spot with a solar tracker. The dimensions of all these modules have also been taken into included in the simulations.

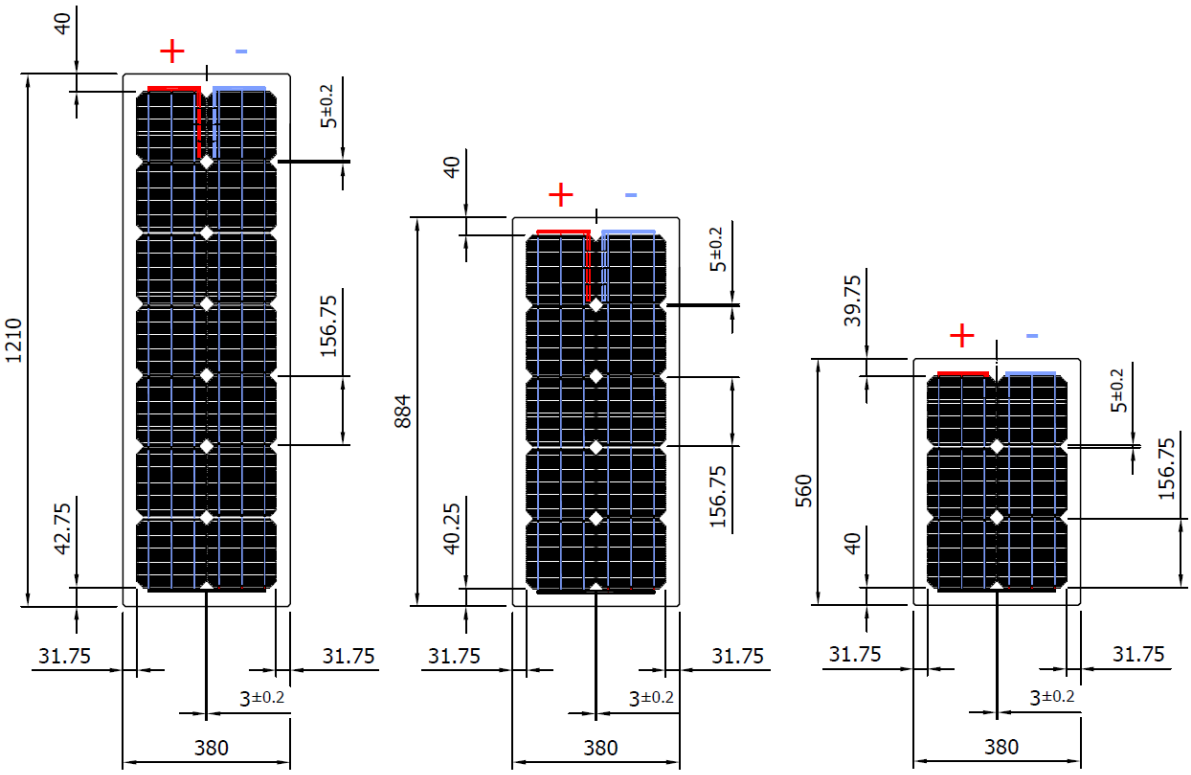

Figure D.1: Mechanincal drawings of the KS Flex modules designed for this project

E

Skyline profiles

E.1. Synthetic Skyline Profiles

The geometrical description of each of the synthetic skyline profiles used in the simulations is presented in Table E.1. Each family is characterized by a different arrangement of the bins that constitute the skyline profile. The skyline profiles that constitute the same family vary in the altitude of the bins, which is determined by the last number in the name of the skyline profile.

Table E.1: Description of the different synthetic skyline profile families

Name	Number of bins	Bin height	Bin width [deg]	Bin separation [deg]	Starting azimuth [deg]
fhA[x]	1	$5 \cdot x$	360	-	0
fhB[x]	1	$10 \cdot x$	180	-	0
fhC[x]	1	$10 \cdot x$	180	-	180
fhD[x]	2	$10 \cdot x$	90	90	45
fhE[x]	3	$10 \cdot x$	60	60	30
fhF[x]	4	$10 \cdot x$	45	45	22.5
fhG[x]	6	$10 \cdot x$	30	30	15
fhH[x]	4	$10 \cdot x$	60	15	37.5
fhI[x]	6	$10 \cdot x$	45	12.85	12.85
fhJ[x]	7	$10 \cdot x$	45	5.62	5.62
fhK[x]	6	$10 \cdot x$	50	8.57	8.57
fhL[x]	6	$10 \cdot x$	55	4.29	4.29

Figure E.1 to E.12 show examples of each of the skyline profiles described above. The shape of the synthetic skyline profiles are overlapped on the sun path in Delft.

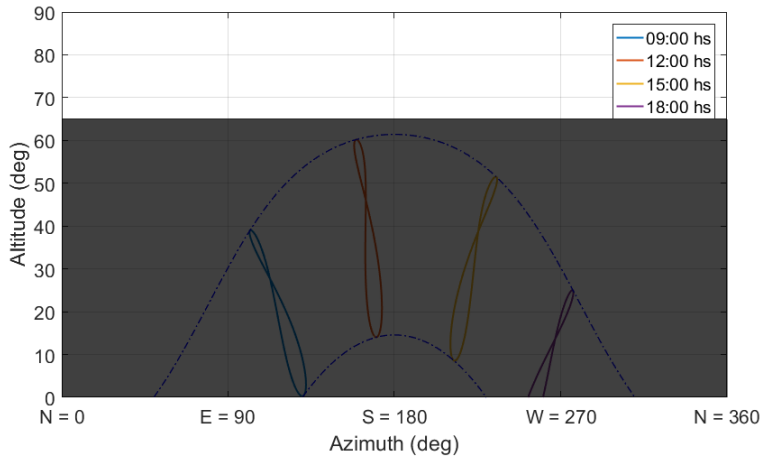

Figure E.1: Synthetic skyline profile fhA13

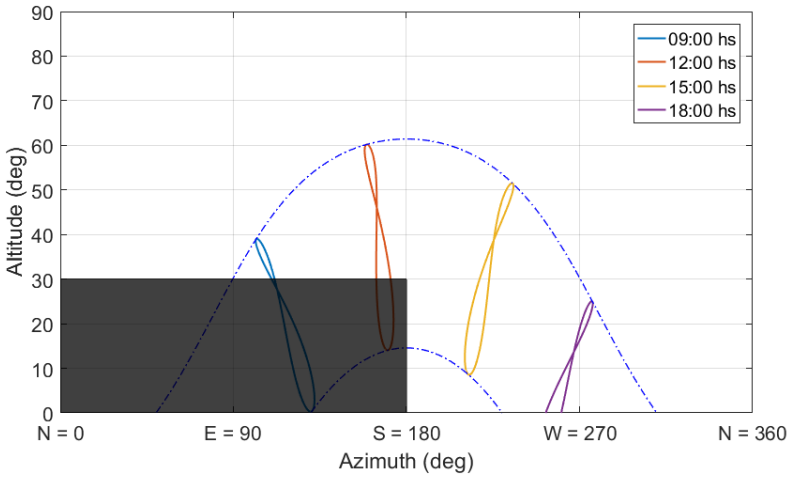

Figure E.2: Synthetic skyline profile fhB3

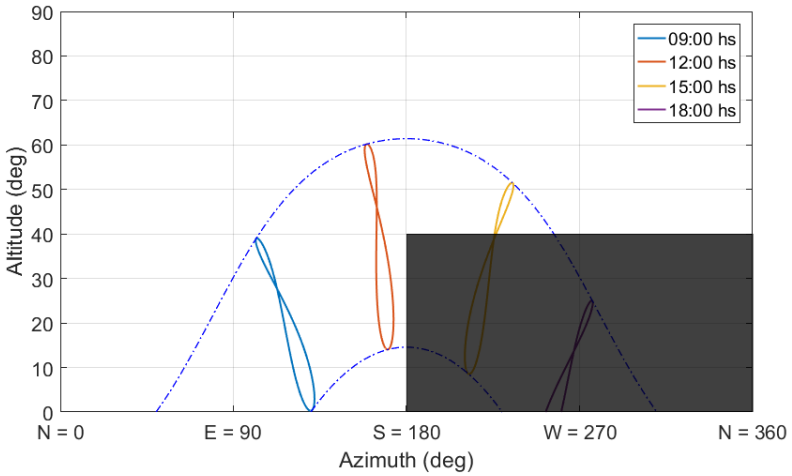

Figure E.3: Synthetic skyline profile fhC4

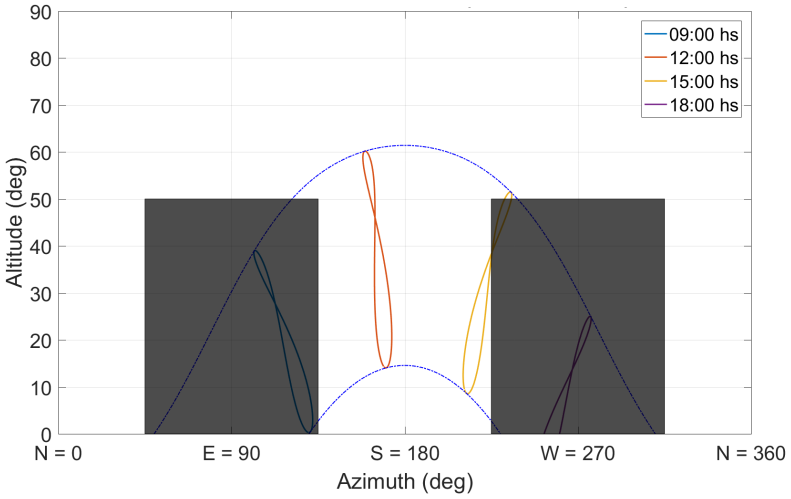

Figure E.4: Synthetic skyline profile fhD5

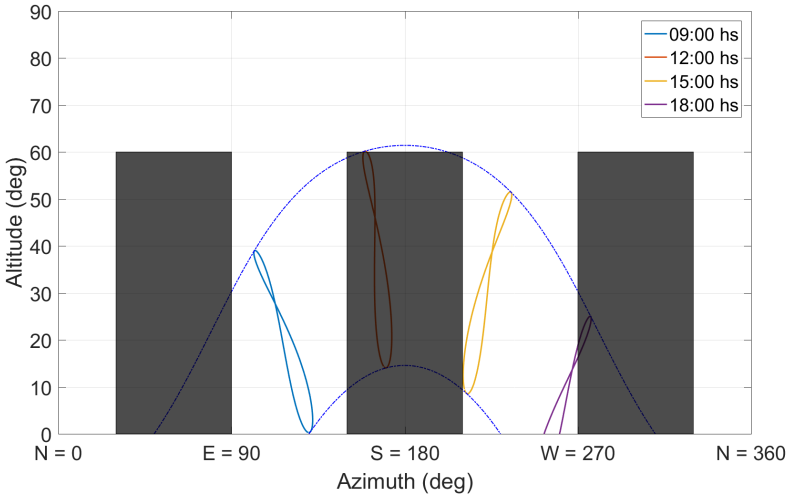

Figure E.5: Synthetic skyline profile fhE6

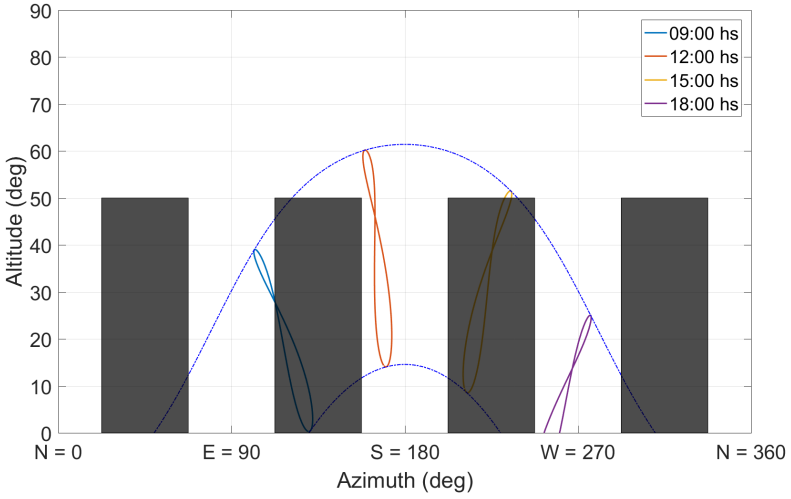

Figure E.6: Synthetic skyline profile fhF5

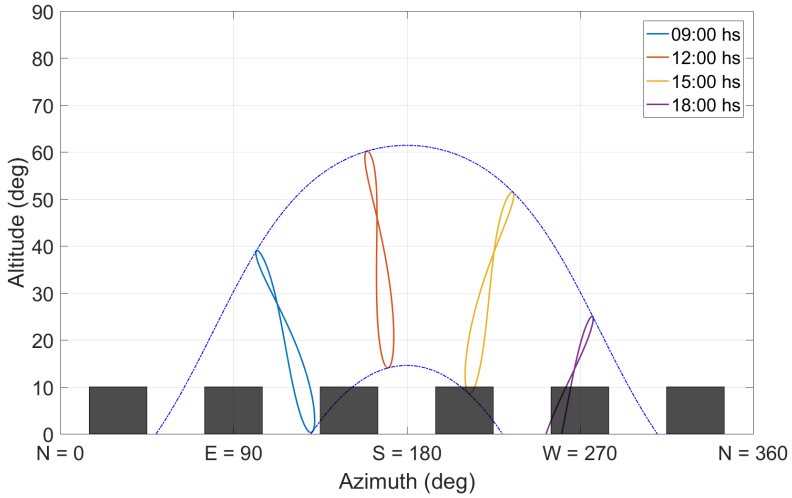

Figure E.7: Synthetic skyline profile fhG1

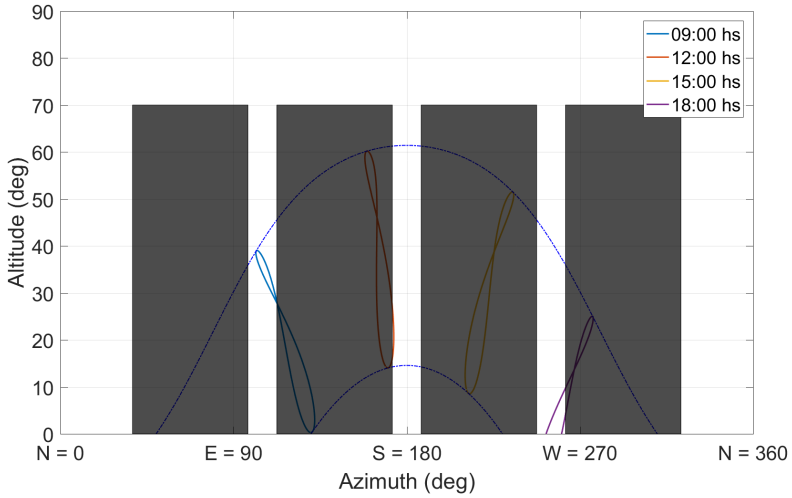

Figure E.8: Synthetic skyline profile fhH7

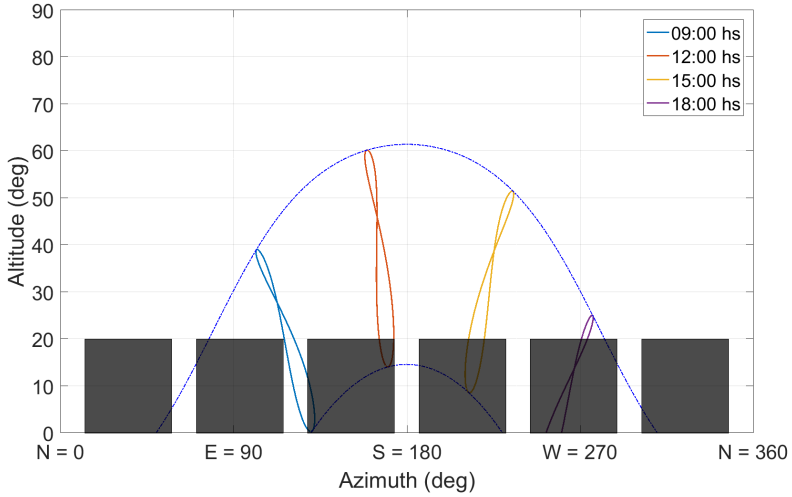

Figure E.9: Synthetic skyline profile fhI2

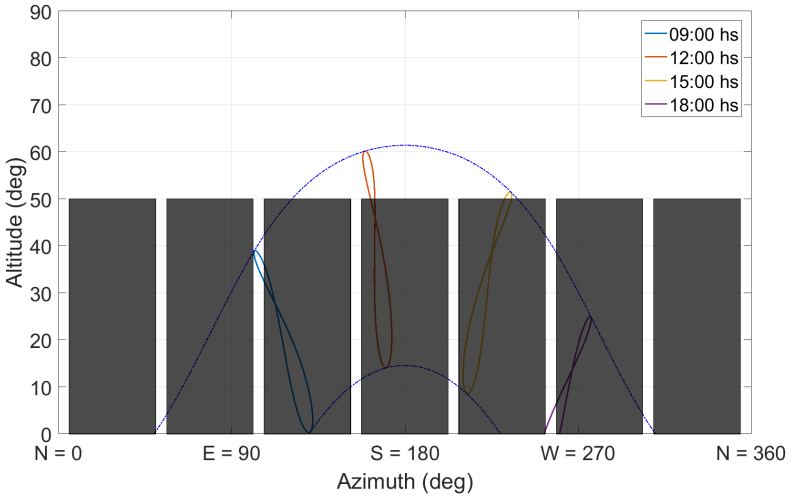

Figure E.10: Synthetic skyline profile fhJ5

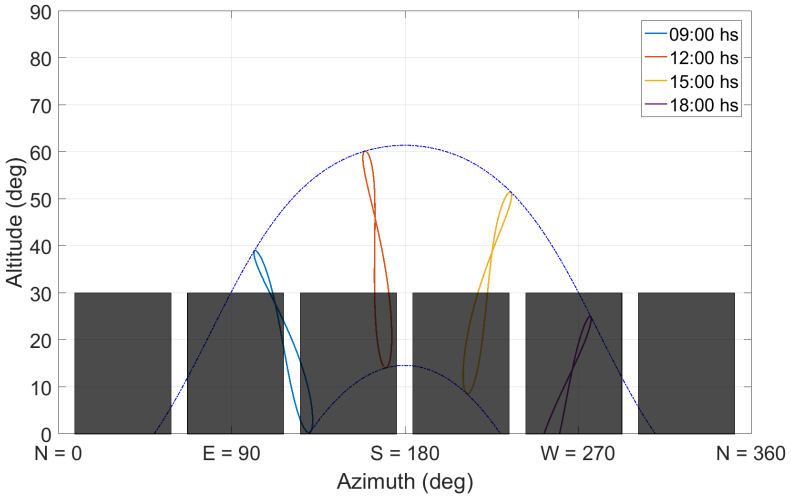

Figure E.11: Synthetic skyline profile fhK3

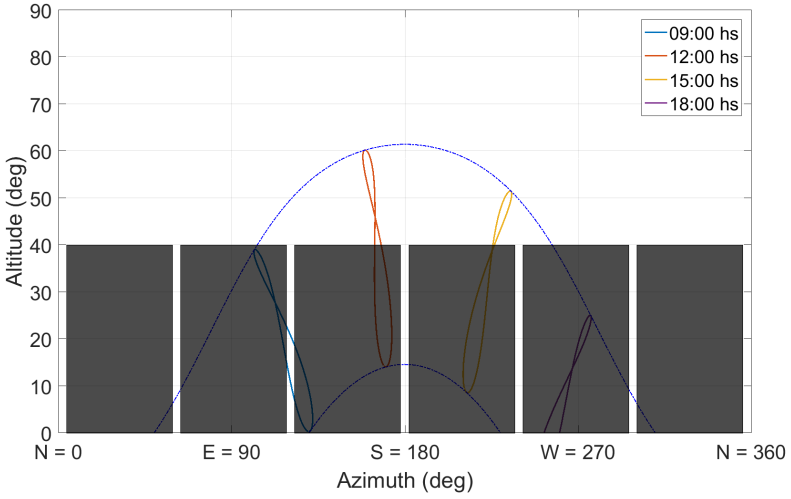

Figure E.12: Synthetic skyline profile fhL4

E.2. Real skyline profiles

The skyline profiles at the 12 bus stops studied with the Horicatcher tool in Delft are presented below. The north direction in pointing upwards in all the images.

(a) TU Mekelpark bus stop

(b) TU Aula bus stop

(c) TU sport en cultuur bus stop

(d) Michiel de Ruyterweg bus stop

(e) Botanische Tuin bus stop

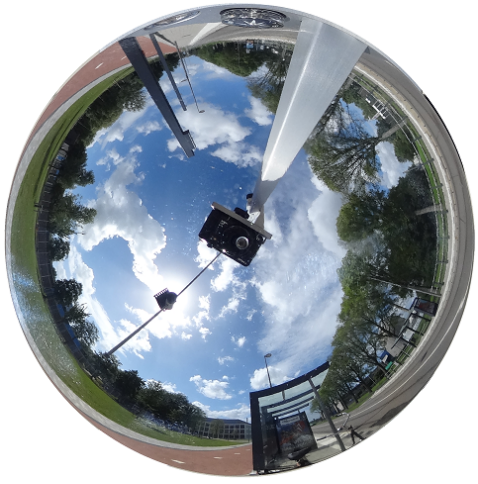

(f) TU Kluyverpark bus stop

Figure E.13: Bus stops studied in Delft

(a) Julianalaan bus stop

(b) Zuidpoort bus stop

(c) Delft Station bus stop

(d) Prinsenhof bus stop

(e) Poortlandplein bus stop

(f) Nassauplein bus stop

Figure E.14: Bus stops studied in Delft

F

Energy yield model coefficients

The coefficients for estimating the energy yield using Equation 4.5 are given in the tables below.

Table F.1: Estimation coefficient for the flat PV module with 14 cells

	a_2 [Wh]	a_1 [Wh]	a_0 [Wh]	b_2 [Wh]	b_1 [Wh]	b_0 [Wh]
N	-631	-8250	8865	-11323	48054	-362
NE	671	-44236	42955	-10691	47357	-317
E	9037	-73172	63015	-10702	47061	-356
SE	-17109	-37556	53855	-12082	46942	25
S	-22038	-30229	51825	-9955	45134	254
SW	-12403	-42782	54792	-11724	46685	71
W	11159	-72129	60082	-10047	46630	-293
NW	5751	-47072	40801	-10447	47253	-323

Table F.2: Estimation coefficient for the 2 flat PV module with 6 cells

	a_2 [Wh]	a_1 [Wh]	a_0 [Wh]	b_2 [Wh]	b_1 [Wh]	b_0 [Wh]
N	-59077	58196	1006	-23446	45136	-1152
NE	-55801	47136	8111	-22219	44496	-1074
E	-16543	-33702	49138	-20783	43348	-904
SE	-28479	-21494	49139	-18334	40784	-358
S	-27930	-24692	52103	-19581	41502	-516
SW	-23603	-26419	49693	-18342	40814	-358
W	-8024	-41333	48499	-19613	42870	-831
NW	-37056	21318	15411	-22641	44819	-1132

A curved module does not have a unique tilt and hence it has multiple SCF and SVF values for the same skyline profile. For this study the tilt at the middle point of the curved PV module (53°) has been used to calculate both factors. This approximation is valid since the radius of curvature of the module is larger than its length.

Table F.3: Estimation coefficient for the curved PV module with 10 cells

	a_2 [Wh]	a_1 [Wh]	a_0 [Wh]	b_2 [Wh]	b_1 [Wh]	b_0 [Wh]
N	11811	-21405	9761	-9083	30152	-395
NE	16913	-48797	31519	-9586	30512	-459
E	607	-34501	33517	-9720	30383	-432
SE	-13957	-21444	34624	-8746	29299	-273
S	-21280	-13467	34386	-9648	29971	-317
SW	-11473	-22977	34171	-8802	29386	-294
W	3882	-36928	32457	-9859	30563	-468
NW	19544	-49987	30364	-9615	30572	-476

G

LightTools model geometry

The distance between the obstacles (skyline profile objects) and the the kiosk in the LightTools model is depicted in Figure G.1. The geometry of this problem is important to understand the results obtained from the simulations, especially in the case when the obstacles and the structure are close to each other.

The angle of the horizon line for the skyline profile fhH4 40°, however, specially when the distance to the obstacle (d_{obs}) is comparable to the dimension of the cell (156.75mm), the upper part and the bottom part of the solar cell do not perceive the same skyline profile. For this reason the angle of the horizon line at the center of the cell is defined:

$$a_{obs} = tan\left(\frac{h_{obs} - 0.249m}{d_{obs} - 0.533m}\right) \tag{G.1}$$

a_{obs} when the obstacles are far enough tends to 40°.

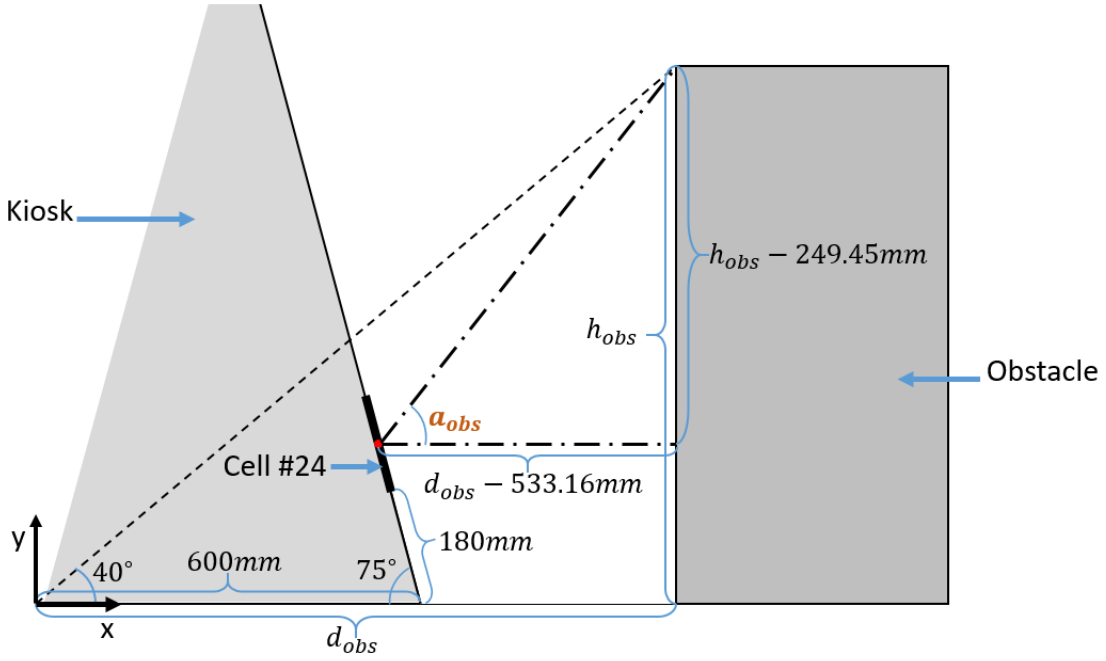

Figure G.1: Geometric description of the LightTools Model

For the distances to the obstacles considered in the simulations different values for a_{obs} are obtained:

In particular for $d_obs = 1m$, it is important to notice that the angle to the top of the obstacle at top of the cell is 46.6°, while at the bottom of the cell the angle equals 56.2°. These differences must be taken into ac-

Table G.1: Angles seen by the solar cell for different obstacle distances

d_{obs} [m]	h_{obs} [m]	a_{obs} [deg]
1	0.84	51.7
2	1.68	44.3
3	2.52	42.6
5	4.20	41.5
10	8.39	40.7
20	16.8	40.4

count when interpreting the results from the simulation which in turns has a resolution of 5° for the different light source positions.

H

The PV bus shelter

The same framework applied to calculate the energy yield of the kiosk was used to estimate the performance of a grid-tied PV bus shelter. The design of the shelter is shown in Figure H.1. Two glass-glass solar panels with 42 cells connected in series are integrated into the shed. The peak power of the bus shelter is 442 W and the roof is tilted 5°.

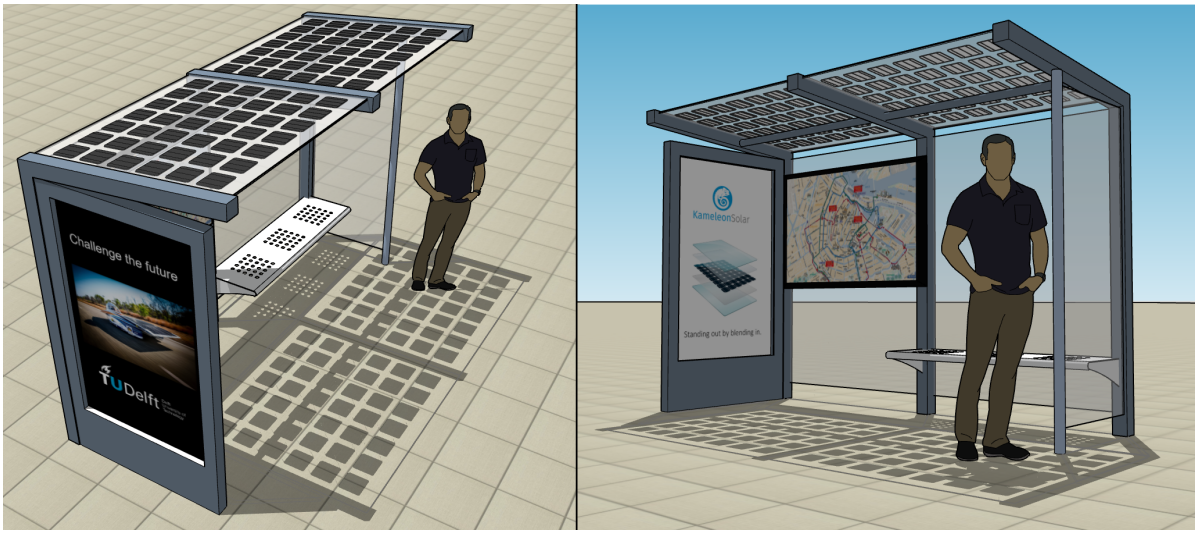

Figure H.1: PV bus shelter model

The performance was assessed under the same synthetic horizons used for the Infotainment Spot. The resulting energy yield for the best (fhA0) and worst (fhA13) skyline profiles conditions using meteorological data for Delft is shown in figure H.2.

Although the tilt of the module is very low, there is a large difference difference between the energy harvested for different orientations when the horizon is completely free. The annual yield is 335 kWh when the modules are facing south, and 189 kWh when the modules are pointing to the north.

However, under the skyline profile fhA13 the *SCF* is null, and the energy yield is almost constant regardless the orientation of the module. In this case the annual energy yield is only 35 kWh.

The highest capacity factor (with a free horizon) of this PV shelter is 9%. On the other hand, the maximum capacity factor of the Infotainment Spot is almost 9.5%. The reason behind this difference is that the tilt of the Infotainment spot has been optimized, while the the roof of the bus shelter is almost horizontal, and the tilt differs significantly from the the optimum value.

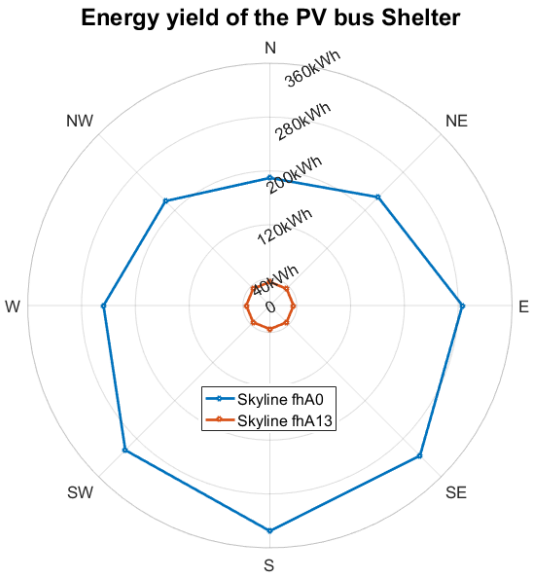

Figure H.2: Yield Shelter

Table H.1 shows the coefficients for predicting the energy yield of the one of the glass-glass PV modules tilted 5° using Equation 4.5. This coefficients were calculated using the same meteorological data as for the kiosk. The corresponding deviations in the prediction from 2006 to 2016 are shown in Figure H.3

Table H.1: Coefficients for predicting the energy yield of one fo the PV modules on the bus shelter

	a_2 [Wh]	a_1 [Wh]	a_0 [Wh]	b_2 [Wh]	b_1 [Wh]	b_0 [Wh]
N	-18226	-18355	36625	-49144	143014	-5525
NE	-37818	-26743	62505	-49062	142441	-5406
E	-64350	-28470	92314	-48760	141442	-5230
SE	-87408	-32603	118289	-48559	140580	-5031
S	-104512	-31802	134118	-48527	140199	-4966
SW	-78556	-36475	114848	-48751	140902	-5115
W	-51941	-36706	86659	-49072	141919	-5294
NW	-28801	-31261	59322	-49251	142763	-5491

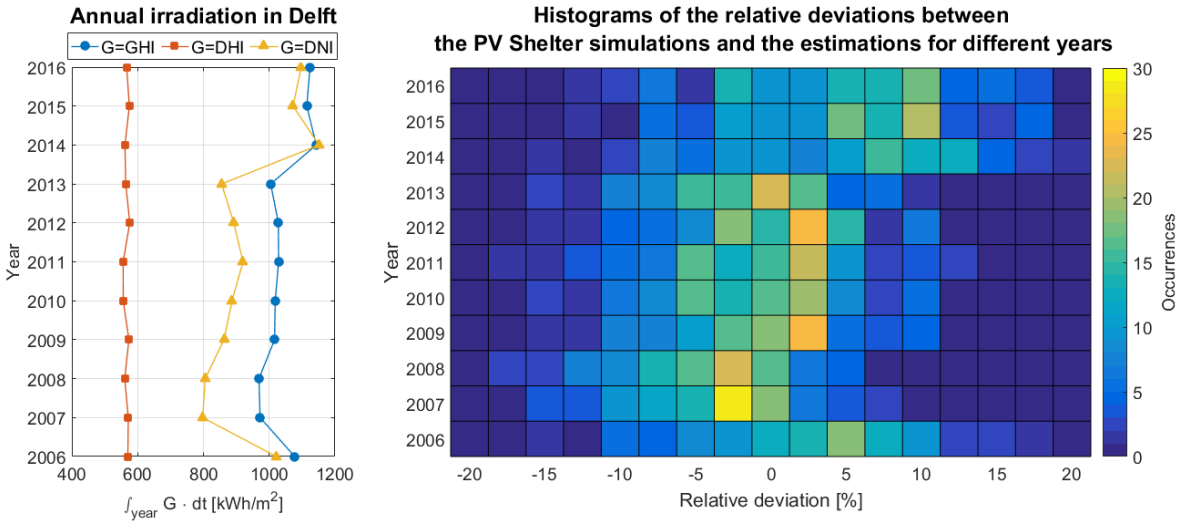

Figure H.3: Deviations between the simulations and the energy yield prediction model between 2006 and 2016

Storage capacity algorithm

The algorithm implemented to calculate the minimum storage capacity required is presented in Figure I.1.

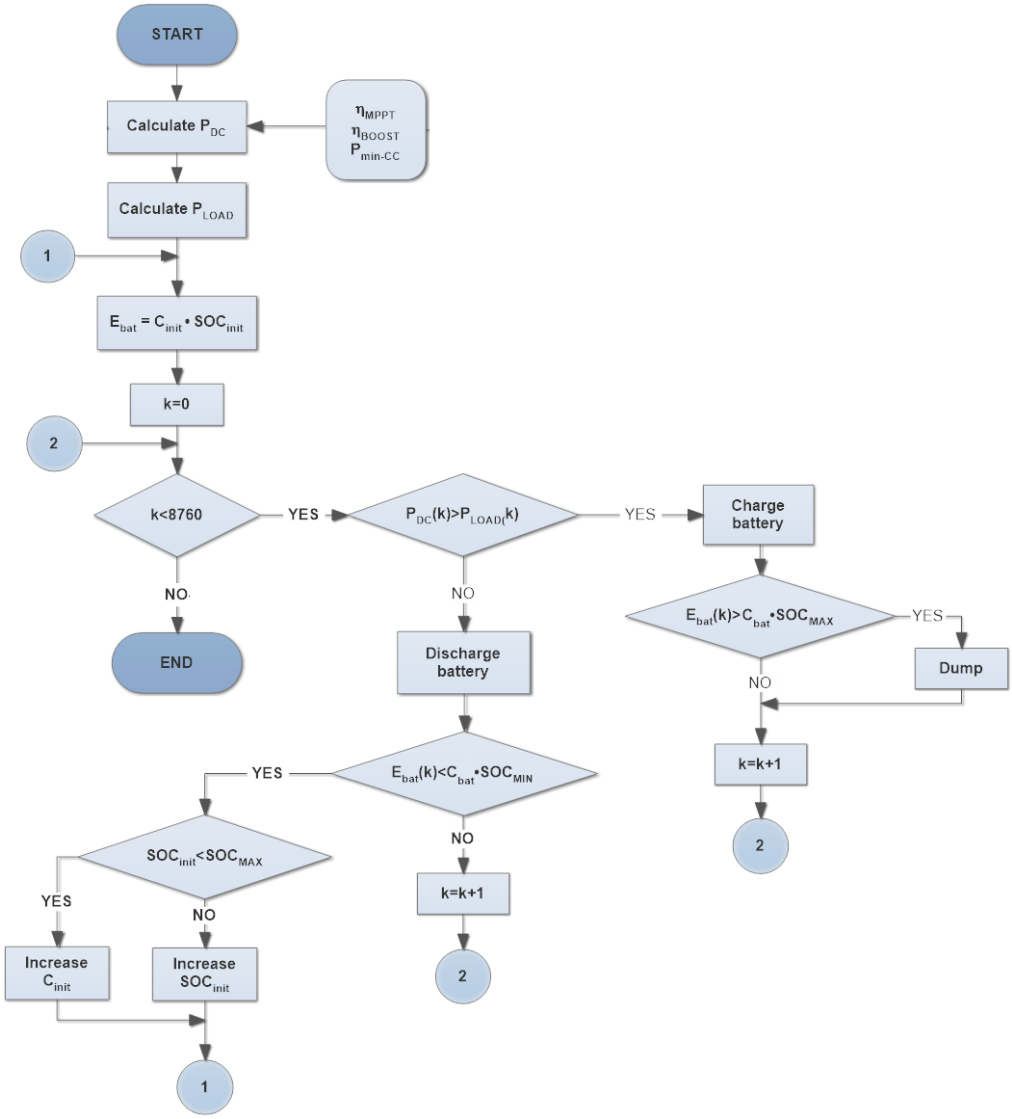

Figure I.1: Minimum storage capacity algorithm

The efficiency of the charge controller (η_{BOOST} and η_{MPPT}) as well as the minimum required power

(P_{min-CC}) were taken into account to calculate the actual electrical output of the PV modules. The internal resistance and the self-discharge rate the battery are included in the blocks that represent the charging and discharging processes.

Bibliography

[1] International Energy Agency. World energy outlook 2016 - excutive summary. Technical report, IEA, 2016.

[2] International Renewable Energy Agency. Rethinking energy 2017: Accelerating the global energy transformation. Technical report, IRENA, 2017.

[3] Andrew W Blakers, Aihua Wang, Adele M Milne, Jianhua Zhao, and Martin A Green. 22.8% efficient silicon solar cell. *Applied Physics Letters*, 55(13):1363–1365, 1989.

[4] Jürgen Garche. Advanced battery systems—the end of the lead–acid battery? *Physical Chemistry Chemical Physics*, 3(3):356–367, 2001.

[5] Martin A Green. The passivated emitter and rear cell (perc): From conception to mass production. *Solar Energy Materials and Solar Cells*, 143:190–197, 2015.

[6] N Guillevin, RCG Naber, LJ Geerligs, and AW Weeber. High efficiency n-type multicrystalline solar cells. In *19th Workshop on Crystalline Silicon Solar Cells & Modules, Materials and Processes*, pages 9–12, 2009.

[7] Ingrid Haedrich, Ulrich Eitner, Martin Wiese, and Harry Wirth. Unified methodology for determining ctm ratios: Systematic prediction of module power. *Solar Energy Materials and Solar Cells*, 131:14–23, 2014.

[8] JE Hay and JA Davies. Calculation of the solar radiation incident on an inclined surface. proceedings, first canadian solar radiation data workshop. *Toronto, Ontario, Canada*, 1978.

[9] Périne Jaffrennou, A Uruena, Jo Das, Julien Penaud, Mathieu Moors, Aude Rothschild, Benoit Lombardet, and Jozef Szlufcik. Laser ablation of sio2/sinx and alox/sinx back side passivation stacks for advanced cell architectures. In *26th World Conference and Exhibition on Photovoltaic Solar Energy Conversion*, 2011.

[10] Jennifer Wen Lin Liao, Mônica Marcondes Cavaleri, and Post Doc. The study of sky view factor in urban morphologies: Computational tools and methods of analysis. *International Plea Conference*, 2014.

[11] B Liu and R Jordan. Daily insolation on surfaces tilted towards equator. *ASHRAE J.;(United States)*, 10, 1961.

[12] Elke Lorenz, Thomas Scheidsteger, Johannes Hurka, Detlev Heinemann, and Christian Kurz. Regional pv power prediction for improved grid integration. *Progress in Photovoltaics: Research and Applications*, 19(7):757–771, 2011.

[13] Daniel MacDonald et al. The emergence of n-type silicon for solar cell manufacture. In *50th Annual AuSES Conference (Solar 2012), Melbourne, Australia*, 2012.

[14] JE Manders, N Bui, DWH Lambert, J Navarette, RF Nelson, and EM Valeriote. Lead/acid battery design and operation. *Journal of power sources*, 73(1):152–161, 1998.

[15] Konrad Mertens. *Photovoltaics: fundamentals, technology and practice*. John Wiley & Sons, 2013.

[16] B Min, H Wagner, M Müller, H Neuhaus, R Brendel, and PP Altermatt. Incremental efficiency improvements of mass-produced perc cells up to 24% predicted solely with continuous development of existing technologies and wafer materials. In *Proceedings of the 30th European Photovoltaic Solar Energy Conference and Exhibition*, 2015.

[17] Public Works Ministry of Transport and Water Management. Public transport in the netherlands, June 2010.

[18] Vimal Adithyan Muthukumar. A new method for calculating solar irradiance on pv systems facing reflective surfaces. Master's thesis, Delft University of Technology, the Netherlands, 2016.

[19] Partha Sarathi Paul, Sudipta Mondal, Nasrin Akter, and Sharif Mohammad Mominuzzaman. Modeling combined effect of temperature and irradiance on solar cell parameters by matlab/simulink. In *Electrical and Computer Engineering (ICECE), 2014 International Conference on*, pages 512–515. IEEE, 2014.

[20] Richard Perez, Pierre Ineichen, Robert Seals, Joseph Michalsky, and Ronald Stewart. Modeling daylight availability and irradiance components from direct and global irradiance. *Solar energy*, 44(5):271–289, 1990.

[21] Simon Philipps. Photovoltaics report. Technical report, Fraunhofer ISE and Werner Warmuth, 2017.

[22] Simone Regondi. Solar powered infotainment spot 2.0. Master's thesis, Delft University of Technology, the Netherlands, 2017.

[23] Douglas T Reindl, William A Beckman, and John A Duffie. Diffuse fraction correlations. *Solar energy*, 45 (1):1–7, 1990.

[24] J Remund, S Müller, S Kunz, B Huguenin-Landl, C Studer, and C Schilte. Meteonorm global meteorological database–handbook part ii: Theory, version 7.1, 2014.

[25] R Santbergen, VA Muthukumar, RME Valckenborg, WJA van de Wall, AHM Smets, and M Zeman. Calculation of irradiance distribution on pv modules by combining sky and sensitivity maps. *Solar Energy*, 150:49–54, 2017.

[26] Santiago Silvestre. Review of system design and sizing tools. *Practical Handbook of Photovoltaics: Fundamentals and Applications. Elsevier, Oxford*, page 543, 2003.

[27] Arno HM Smets, Klaus Jäger, Olindo Isabella, René ACMM van Swaaij, and Miro Zeman. *Solar Energy: The physics and engineering of photovoltaic conversion, technologies and systems*. UIT Cambridge Limited, 2016.

[28] D. G. Steyn. The calculation of view factors from fisheye-lens photographs: Research note. *Atmosphere-Ocean*, 18(3):254–258, 1980.

[29] VDMA. International technology roadmap for photovoltaics - results 2016, including maturity report. Technical report, ITRPV, 09 2017.

[30] Xingchi Wang, Peter Adelmann, and Thomas Reindl. Use of lifepo4 batteries in stand-alone solar system. *Energy Procedia*, 25:135–140, 2012.

[31] Vincent Weeda. Solar powered infotainment spot. Master's thesis, Delft University of Technology, the Netherlands, 2014.